

WEIGHING THE GIANTS USING COSMIC MICROWAVE BACKGROUND LENSING

Submitted in Total Fulfillment
of the Requirements of the Degree of
Doctor of Philosophy

SCHOOL OF PHYSICS
The University of Melbourne

SANJAYKUMAR PATIL

Abstract

Clusters of galaxies are powerful probes of cosmology. The number density of galaxy clusters is sensitive to

Statement of contribution:

This is to certify that:

- This thesis entitled “Weighing the giants with CMB-lensing” comprises my original work towards the degree of Doctor of Philosophy.
- Due acknowledgement has been made in the text to all other material used.
- The thesis is less than 100,000 words in length, exclusive of tables, maps, bibliographies, and appendices.

.....
Sanjaykumar Patil

Preface

While this thesis is substantially my own work, it also contains the work that has been done in collaboration with colleagues. This section describes the publication on which some of the chapters are based.

- Chapter 1 and 2 comprises a fully referenced literature review of the standard model of cosmology. Both the chapter have been written by me.

- Chapter 3 explains the Maximum Likelihood Estimator and is based on the work presented in the following publication

Raghunathan, Patil, Baxter, Bianchini, Bleem, Crawford, Holder, Mazzotti, and Reichardt (2017).

The lensing pipeline and simulations were generated by Srinivasan Raghunathan. I did the validation of pipeline and quantified the systematic biases due to redshift uncertainty.

- Chapter 4 is based on the following publication

Raghunathan, Patil, Baxter, Benson, Bleem, Chou, Crawford, Holder, Mc Clintock, Reichardt, Rozo, Varga, Abbott, Ade, Allam, Anderson, Annis, Austermann, Avila, Beall, Bechtol, Bender, Bernstein, Bertin, Bianchini, Brooks, Burke, Carlstrom, Carretero, Chang, Chiang, Cho, Citron, Crites, Cunha, da Costa, Davis, Desai, Diehl, Dietrich, Dobbs, Doel, Eifler, Everett, Evrard, Flaugher, Fosalba, Frieman, Gallicchio, García-Bellido, Gaztanaga, George, Gilbert, Gruen, Gruendl, Gschwend, Gupta, Gutierrez, de Haan, Halverson, Harrington, Hartley, Henning, Hilton, Hollowood, Holzapfel, Honscheid, Hou, Hoyle, Hrubes, Huang, Hubmayr, Irwin, James, Jeltema, Kim, Carrasco Kind, Knox, Kovacs, Kuehn, Kuropatkin, Lee, Li, Lima, Maia, Marshall, McMahon, Melchior, Menanteau, Meyer, Miller, Miquel, Mocanu, Montgomery, Nadolski, Natoli, Nibarger, Novosad, Padin, Plazas, Pryke, Rapetti, Romer, Carnero Rosell, Ruhl, Saliwanchik, Sanchez, Sayre, Scarpine, Schaffer, Schubnell, Serrano, Sevilla-Noarbe, Smecher, Smith, Soares-Santos, Sobreira, Stark, Story, Suchyta, Swanson, Tarle, Thomas, Tucker, Vanderlinde, De Vicente, Vieira, Wang, Whitehorn, Wu, and Zhang (2019a).

I did the analysis using the simulations, applied it to the real data, and

obtained the posterior probability distribution. In addition to that I quantified the bias due to our assumption of underlying cosmology and wrote the draft of introduction, data, results and conclusion work of the section.

- Chapter 5 is based on:

Patil, Raghunathan, and Reichardt (2019).

I developed the new method to suppress the major foreground in lensing analysis, generated the simulations to validate the newly developed method, forecasted the mass uncertainties future surveys will achieve. I also wrote the entire draft with suggestion from Christian Reichardt and Srinivasan Raghunathan.

- Chapter 6 is entirely written by me. It summarizes all the work done during thesis and also sheds some light on future direction of CMB-cluster lensing.

In addition to the above mentioned publications I have also been actively involved:

-

Contents

Chapter 1: Introduction	1
1.1 Expanding universe	1
1.2 Cosmological distances	2
1.3 Friedmann Equations	4
1.4 Cosmic Inventory	7
1.5 Cosmic Microwave Background	9
1.6 Boltzmann equations	10
1.7 Primary anisotropies	11
Chapter 2: Cluster Cosmology	15
2.1 Overview	15
2.2 Linear theory of structure formation	15
2.3 Power spectrum	17
2.4 Statistics of spherically collapsed objects	20
2.4.1 The Press-Schechter Theory	21
2.5 Galaxy Clusters & Cosmology	21
2.5.1 Limited by mass estimation	24
Chapter 3: Maximum Likelihood Estimator	27
3.1 CMB lensing overview	27
3.2 Maximum Likelihood Estimator	30
3.2.1 Covariance matrix calculation	31
3.3 Results	33
3.3.1 Idealised simulations	33
3.3.2 Effects of extragalactic foregrounds on lensing analysis . . .	35
3.4 Systematic bias checks	37
3.4.1 Halos along the line of sight	39

3.4.2	Cluster mass profiles	40
3.4.3	Cluster miscentering	41
3.4.4	Bias due to redshift uncertainty	42
3.4.5	Bias due to the kinematic SZ signal	43
3.4.6	Thermal Sunayev-Zel'dovich effect	44
3.4.7	Dusty galaxies in the cluster and other foregrounds	47
3.5	A look into the future	47
3.5.1	Expected lensing mass uncertainties for future CMB experiments	48
3.5.2	Optimizing survey design: SNR as a function of beam size and map noise levels	52
3.6	Conclusion	54
Chapter 4: modified quadratic estimator		57
4.1	Thermal Sunayev-Zel'dovich effect	57
4.2	QUADRATIC ESTIMATOR	59
4.2.1	removing SZ induced bias	62
4.3	Data	64
4.3.1	South Pole Telescope	64
4.3.2	DES and the redMaPPer catalog	66
4.3.3	CLUSTER CUTOUTS	68
4.4	Model Fitting	70
4.5	pipeline verification	71
4.5.1	“Curl” null test	71
4.5.2	Systematic error budget	71
4.6	Results and Discussion	76
4.6.1	Stacked mass measurements	76
4.6.2	Mass-richness $M - \lambda$ scaling relation calibration	78
4.6.3	Comparison to literature	79
Chapter 5: Template Fitting		83
5.1	Method	83
5.1.1	Template fitting to reduce the SZ variance	83
5.1.2	Sources of uncertainty in the CMB-Cluster Lensing Measurement	87

5.2	Results	89
5.2.1	Miscentering	90
5.2.2	Robustness of template fitting method	91
5.3	Forecasts	92
5.4	Discussion and Conclusion	93
Appendix A:	Appendix A	113
A.1	Section in an appendix	113
A.2	Simulated skies	113
A.2.1	Cosmic Microwave Background	114
A.2.2	Sunyaev-Zel'dovich (SZ) effect	114
A.2.3	Radio and Dusty Galaxies	115

List of Tables

3.1	The percentage mass biases from various systematic uncertainties. A positive (negative) number means the recovered mass is over-(under-)estimated. The first three lines reflect the expected biases from astrophysical foregrounds; these are serious for the temperature estimator, but not the polarization estimator. The next two lines deal with uncertainties in where the cluster is located (whether in redshift or on the sky); these are likely to be manageable for both estimators. The last four lines relate to uncertainties in how the mass is distributed, whether due to projection effects from nearby, lower-mass haloes, or due to uncertainties in the average mass profile for galaxy clusters. These questions about the mass distribution are a concern for both temperature and polarization.	39
3.2	The forecasted mass uncertainties for large-aperture future CMB experiments. We combine data from 90, 150, and 220 GHz to clean the extragalactic foregrounds using a constrained ILC method designed to remove the tSZ signal while minimizing the residual foreground power and instrumental noise. For polarization, the ILC is essentially optimal weighting of the bands for minimum noise.	49

List of Figures

1.1	Cosmological distances as a function of redshift; solid lines represent matter dominated universe.	4
1.2	Scaling of various components as function of scale factor (a). While radiation is dominant component in the early universe, dark energy is dominant at present.	7
1.3	CMB as observed by <i>Planck</i> satellite. Credits: ESA/ <i>Planck</i> collaboration	10
1.4	Angular power spectrum of CMB primary temperature anisotropies for <i>Planck</i> cosmology (Planck Collaboration et al., 2018).	12
1.5	The above figure depicts important scenarios as experienced by an electron at the time recombination; it is adopted from the works of Hu and White (1997) and Dodelson (2003).	14
2.1	Total transfer function (CDM+baryon+neutrinos) as calculated by <i>CAMB</i>	18
2.2	Total matter power spectrum generated by <i>CAMB</i> for two different redshifts.	20
2.3	Galaxy cluster Abell 1689. Credits: HST/Chandra X-ray observatory	22
2.4	On the left is flat Λ CDM model: constraints on Ω_m and σ_8 from clusters in purple, from CMB observations in blue (<i>Planck</i>) and grey (<i>Planck</i> and WMAP). On the right we have flat w CDM: constraints on w and Ω_m for various cosmological probes. Cluster (purple) provide the tightest single-probe constraints.	23
2.5	Effects of systematics in mass estimation on cluster cosmology. . .	24

3.1	Lensing effect on CMB due to a galaxy cluster of mass $5 \times 10^{14} M_{\odot}$. On the top panel we show the effect of cluster lensing on CMB temperature field. Bottom two panels are for the stokes Q and U parameters. The lensing signal for temperature is few μK and an order of magnitude smaller in polarisation. Note that in the above simulation we haven't used either experimental noise or foregrounds.	28
3.2	In the top panel we show the combined likelihood of 100,000 clusters each at redshift of 0.7 and at mass of $2 \times 10^{14} M_{\odot}$ for temperature and polarisation MLE estimators. The difference between QU and EB estimator isn't statistically significant. In the bottom panel we show the results of null test and as expected the likelihood peaks at zero for all three estimators	34
3.3	In the left we show the performance of different estimators for idealised simulations as function of experimental noise levels. We consider the effects of various foregrounds on the estimators in the right panel. All the curves are for a set of 100,000 clusters each at mass of $2 \times 10^{14} M_{\odot}$ and at redshift of 0.7.	36
3.4	The positional offset between the assumed and true cluster centroid will bias the estimate low for T_{ML} (black triangles) and QU_{ML} (orange squares) estimators. The typical positional offset of 0.5' (von der Linden et al., 2014; Song et al., 2012; Sereno et al., 2016) is marked with the vertical dashed line. The error bars are derived using estimates gathered by repeating the test 100 times.	43
3.5	The expected residual foreground and noise power spectrum for the future CMB experiments. The 90, 150, and 220 GHz channels have been combined using a constrained ILC technique to remove the tSZ effect while minimizing other extragalactic foregrounds and instrumental power. The left and the right panels correspond to temperature and polarization respectively. The plateauing of the residual temperature spectrum reflects the limited foreground removal possible with three frequency channels. Specifications about each experiment are listed in Table 3.2.	48

3.6	The performance of the polarization MLE is very sensitive both to the angular resolution and map noise level of an experiment; the gains for the temperature MLE are much smaller. The numbers correspond to the CMB-cluster lensing mass uncertainty (in percent) of the cluster sample containing 100,000 clusters after the addition of foregrounds (dotted lines in right panel of Fig. 3.3). Improving the beam from 3.'5 to 1' enhances the SNR by a factor of two for the CMB-S4 noise levels. The saturation of T_{ML} is due to the larger impact of foregrounds on the temperature maps.	50
4.1	The plot shows the intensity of CMB as function of frequency before (black) and after (blue) it passes through a cluster.	58
4.2	A galaxy cluster of mass $M_{200m} = 5 * 10^{14} M_{\odot}$ as seen in a CMB survey with following specifications : 1.'7 beam at 90 GHz (left panel) and 1'beam at 150 GHz (right panel).	59
4.3	Schematic representation of quadratic estimator. Top panel shows the observed CMB temperature map which acts as the input. The observed map is passed through the filters to obtain large scale gradient map (left middle panel) and small scale lensing map (right middle panel). QE extracts the correlation between panel gradient map and lensing map to obtain reconstructed lensing convergence profile shown in panel the bottom panel	60
4.4	Gradient of temperature field as a function of low pass filter $l = l_G$. It is dominated by multipoles below 2000.	62
4.5	Effect of SZ on lensing convergence profile. On the top panel we show the lensing convergence profile for a stack of 1000 cluster each at a mass of $M_{200m} = 2 * 10^{14} M_{\odot}$ and a redshift of $z = 0.7$ with experimental white noise level of $3\mu\text{K} - \text{arcmin}$; left panel is without SZ and right panel is with SZ. On the bottom panel we have radial profile of the same in solid blue (without SZ) and green (with SZ) curves; black curve is the radial profile of the input NFW profile.	63
4.6	SPTpol noise power spectrum of temperature and polarisation maps.	67

4.7	Stacked result of the curl test performed at the cluster locations by replacing the divergence operator in Eq. (5.3) with a curl operator. We obtain a PTE value of 0.26, consistent with a null result. For the ease of visual comparison we adopt the same colour scale as in Fig. 4.10.	72
4.8	Quantifying the level of bias due to residual foregrounds and the SZ signal using S10 simulations. The recovered lensing mass, unbiased for the fiducial case with SZ-free map for gradient estimation and $l_G = 2000$ is shown as black circles. The equivalent biased results with just the 150 GHz map and $l_G = 1500(2000)$ cutoff scales for the gradient estimation are shown as red squares (orange diamonds). Each light shaded point corresponds to an individual simulation run with clusters from the ES RM Year-3 flux-limited sample. The darker data points are the values obtained for $10 \times$ the sample size	73
4.9	The inverse-variance weighted stacked convergence maps at the location of 4002 and 1741 clusters in the range $\lambda \in [20,1000]$ from flux limited (left) and the volume-limited (right) samples of the DES RM Year-3 cluster catalog. The contour corresponds to the regions above 3.5σ . The null hypothesis of no-lensing is rejected at 8.7σ and 6.7σ for the two cases respectively.	77
4.10	The azimuthally averaged radial profile of the stacked convergence maps from Fig. 3. The black circles and orange diamonds correspond to the flux and volume-limited Year-3 DES RM cluster samples. The error bars are the diagonal value of the covariance matrix estimated using the jackknife technique in Eq. (10). The data points for the two sample have been artificially shifted from the bin centres to avoid cluttering.	78
4.11	Marginalized posteriors of the normalization parameter A of the M- λ relation for the volume-limited sample of the RM cluster-catalog. The result is consistent with the best-fit values obtained by DES weak-lensing measurements (M18), shown as the shaded region	80

4.12 Comparison of M_{200m} mass estimates of galaxy clusters obtained using the M- λ relation from different works in the literature using the RM cluster catalogs. The points have been normalized using the 1σ error from the analysis with the Year-3 volume-limited sample of the DES RM catalog. The filled (open) points represent measurements using the CMB-cluster lensing (galaxy weak-lensing) technique	81
5.1 Template fitting significantly reduces SZ power, even with an imperfect match between the template and true SZ signal. The top left panel (a) shows the expected Arnaud profile for a galaxy cluster of mass $M_{200m} = 510^{14} M_\odot$ at $z=0.7$ after being smoothed by Gaussian beam with FWHM= 1'.7. The top right panel (b) shows the residuals after subtracting the best-fit 2'.0 FWHM Gaussian (the amplitude is free, but the FWHM is fixed). The lower panel (c) shows one-dimensional slices through each panel: the solid, blue line is a slice through the beam-convolved Arnaud profile of (a), and the dashed green line is a slice through the residual map in (b).	85
5.2 Ratio of SZ variance over kappa variance as a function of cluster mass and experimental noise level. As expected the ratio increases with mass for a given experimental noise level. The black solid line represents the points where the ratio SZ variance is equal to that of experimental noise.	88
5.3 Projecting out an SZ template from the second leg o the modified QE improves the performance for all masses considered. Here we show the percentage mass uncertainties from three methods for a sample of 1000 clusters at a experimental noise level of $3 \mu\text{K}\text{-arcmin}$. All the curves use an SZ-free map for the gradient, but make different assumptions about the second, high-pass filtered map.	89

5.4 Our new method is robust to realistic SZ simulations. The red and black solid curves show the performance of modified QE for the Sehgal and Takahashi simulations respectively. The dashed lines show the improvement in each case when template fitting is used to reduce the SZ variance in the small-scale map. [SR: Change xlabel to M_{200m}].	91
5.5 Our new method is robust to realistic SZ simulations. The red and black solid curves show the performance of modified QE for the Sehgal and Takahashi simulations respectively for a sample of 1000 clusters. The dashed lines show the improvement in each case when template fitting is used to reduce the SZ variance in the small-scale map. The plotted uncertainties are for a stack of 1000 galaxy clusters of the quoted mass at $z = 0.7$	93

Chapter 1

Introduction

Cosmologists answer the age-old question, "where did we come from?". Over the last two and half decades with flood of data from cosmological experiments, we have entered a "precision era" in cosmology. With the available cosmological data and the strong theoretical premises of the General Theory of relativity, the Universe can be divided into three main components. Only 5% of the universe is made up of baryons, which is mainly in the form of stars and gas in galaxies. Approximately 27% ? is made up of dark matter, which is responsible for additional gravitational effects in the Large Scale Structures. Remaining 68% is made up of elusive dark energy, which is responsible for the accelerated expansion of the universe. This chapter reviews the theoretical framework of the homogeneous universe and the Cosmic Microwave Background (CMB).

1.1 Expanding universe

In 1929, Edwin Hubble observed that the galaxies that are farther away from us are moving away at a faster rate Hubble (1929). This was the first observational evidence of expanding universe. The wavelength of the light traveling through space stretched by the Universe. This shift in wavelength to longer wavelengths is called redshift, z , and defined as:

$$z = \frac{\lambda_o - \lambda_e}{\lambda_e} = \frac{\lambda_o}{\lambda_e} - 1, \quad (1.1)$$

where λ_o and λ_e are the observed and emitted wavelengths respectively.

Hubble's data could be fit by a linear relation between galaxy velocity and its distance, a relation now known as Hubble's law

$$v = H_o d \quad (1.2)$$

where v is the velocity, d is the proper distance, and H_o is the Hubble constant

which is usually expressed as

$$H_o = 100h \text{ km s}^{-1} \text{Mpc}^{-1} \quad (1.3)$$

where h is the dimensionless Hubble parameter, measured by Planck Collaboration et al. (2018) to be $h = 0.674 \pm 0.005$. Assuming the Universe is expanding at constant rate, v constant and at $t = 0$ the Universe started. Through simple math we can get rough age of the Universe also known as the Hubble time,

$$t_H = \frac{1}{H_0} = 9.836 \times 10^9 h^{-1} \text{ yr.} \quad (1.4)$$

Hubble distance is defined as the distance light travelled in Hubble time which is roughly $3 \times 10^3 h^{-1} \text{ Mpc}$

The current paradigm of cosmology rests on the following three main assumptions

- General Theory of Relativity is valid on all length scales in the universe
- The different components of the universe obey equation of state
- universe is homogeneous and isotropic at sufficiently large length scales (Copernican Principal or CP)

The Friedmann-Lemaître-Robertson-Walker (FLRW) metric is the only metric in General Relativity consistent with the Copernican principle and expanding universe. The FLRW metric is given by:

$$ds^2 = dt^2 - a^2(t) \left[\frac{dr^2}{1 - kr^2} + r^2(d\theta^2 + \sin^2(\theta)d\phi^2) \right]^1 \quad (1.5)$$

where $a(t)$ is the scale factor, r is the comoving distance, and k is the curvature (k zero in flat Λ CDM cosmology).

1.2 Cosmological distances

While measuring distances is crucial in understanding the underlying cosmology, it can be tricky in an expanding universe. In a time interval dt light travels a comoving distance of $dt/a(t)$. The comoving distance light has travelled since the

¹we have set speed of light, $c = 1$

beginning of the universe is obtained by integrating the equation below,

$$\eta = \int_0^t dt/a(t) \quad (1.6)$$

This distance, η , defines the comoving horizon, no information could have travelled between the regions that are separated by distance $> \eta$. We can get the comoving distance between an astrophysical object at redshift of z in a similar way

$$\chi(a) = \int_{t(a)}^{t_0} \frac{dt'}{a(t')} = \int_z^0 \frac{dz}{z^2(z)H(z)} \quad (1.7)$$

where $H(z) = \dot{a}/a$ is the Hubble parameter which depends on the cosmology. At late times the universe is matter dominated, so we can ignore the contribution of the other components in the universe and analytically integrate the above equation

$$\chi(a) = \frac{2}{H_0} \left[1 - \frac{1}{\sqrt{1+z}} \right] \quad (1.8)$$

Another way to measure the distance in cosmology is by measuring the angle θ subtended by an object of known physical size l .

$$d_A = \frac{l}{\theta} \quad (1.9)$$

The subscript ‘A’ stands for the angular diameter distance. The comoving size of an object is given by l/a , the angle subtended in terms of comoving distance is $\theta = (l/a)/(\chi)$, plugging this in above equation gives

$$d_A = a\chi = \frac{\chi}{1+z} \quad (1.10)$$

Observed flux can be used to measure the luminosity distance of a cosmological object.

$$F = \frac{L(\chi)}{4\pi\chi^2} \quad (1.11)$$

where F is the observed flux and $L(\chi)$ is the comoving luminosity. Comoving Luminosity is related to intrinsic luminosity as $L(\chi) = La^2$, plugging this in the above equation we get Luminosity distance as

$$d_L = \chi * (1+z) \quad (1.12)$$

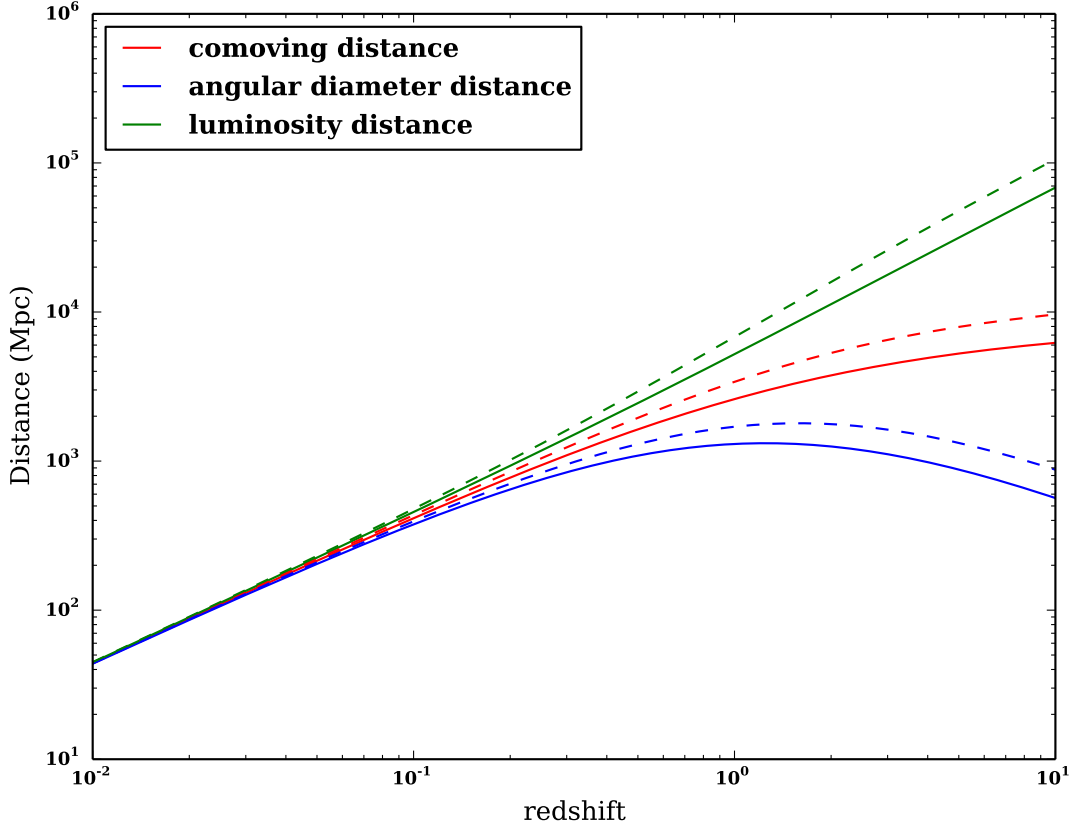


Figure 1.1: Cosmological distances as a function of redshift; solid lines represent matter dominated universe.

Fig. 1.1, shows cosmological distances as a function of redshift; dashed lines represent the *Planck* (Planck Collaboration et al., 2018) cosmology and solid lines represent matter only universe.

1.3 Friedmann Equations

The mathematical formalism of the universe so far based on the assumption of isotropy and homogeneity in an expanding universe which led us to the FLRW metric. General theory of relativity relates the dynamics of the background universe to the matter and energy content in the universe via the Einstein Field Equations

$$R_{\mu\nu} - \frac{1}{2}g_{\mu\nu}R = 8\pi GT_{\mu\nu}. \quad (1.13)$$

The L.H.S corresponds to the geometry of the universe, while the R.H.S represents the matter and energy content in the universe. In the above equation $R_{\mu\nu}$ is the

Ricci tensor which depends on the metric and its derivatives, R is the Ricci scalar and $g_{\mu\nu}$ is the metric. The stress energy tensor, $T_{\mu\nu}$, is given by:

$$T_{\nu}^{\mu} = (\rho + P)u^{\mu}u_{\nu} - P\delta_{\nu}^{\mu} \quad (1.14)$$

where $\rho(t)$ and $P(t)$ are the energy density and pressure in the rest frame of the fluid and u^{μ} is the relative four velocity of the fluid. Solving the time-time component of the Einstein field equation yields an equation for the evolution of the scale factor,

$$H = \frac{\dot{a}}{a} = \frac{8\pi G}{3}\rho - \frac{k}{a^2} \quad (1.15)$$

while all three spatial components reduce to

$$\frac{\ddot{a}}{a} = -\frac{4\pi G}{3}(\rho + P) \quad (1.16)$$

where $\rho = \Sigma_i \rho_i$ and $P = \Sigma_i P_i$ are the sum of energy density and pressure of all the components in the universe respectively. Equations 1.16 and 1.15 are the Friedmann equations governing the evolution of the background universe.

The average mass density of the Universe required to just halt the expansion of the Universe, it is given by,

$$\rho_{crit} = \frac{3H^2}{8\pi G} \quad (1.17)$$

Note that the value of critical density depends on Hubble's constant which is time dependent. The present value of critical density is approximately $10^{-26} kg/m^3$. While this is equivalent to 6 hydrogen atoms per cubic meter, the best achievable terrestrial vacuum is 10^9 atoms per cubic meter. The critical density can be used to define dimensionless density parameters as $\Omega_i = \rho_i/\rho_{crit}$. Assuming all the components in the universe are perfect isotropic fluids, we can write down the stress energy tensor as

$$T_{\nu}^{\mu} = \begin{pmatrix} -\rho & 0 & 0 & 0 \\ 0 & P & 0 & 0 \\ 0 & 0 & P & 0 \\ 0 & 0 & 0 & P \end{pmatrix} \quad (1.18)$$

Using the energy-momentum conservation condition

$$\dot{\rho} + H(3\rho + P) = 0 \quad (1.19)$$

Note that the continuity equation will also hold for individual species as long as we neglect the energy exchange among different components. As mentioned earlier the cosmological fluids are expected to obey the equation of state: $P = w\rho$. Plugging this in the above equation we can solve for density as function of scale factor

$$\rho(a) \propto \exp\left(-3 \int_0^\infty \frac{da'}{a'} [1 + w(a')]\right) \quad (1.20)$$

For a time-independent equation of state parameter w the above equation reduces to $\rho \propto a^{-3(1+w)}$.

The components of the Universe that we know about are:

- **Non relativistic matter:** For non-relativistic matter such as cold dark matter and baryons the energy density is equal to the rest mass energy. The pressure is much smaller than the energy-density ($P \ll \rho$). In such cases $w = 0$ and the density will scale as $\rho \propto a^{-3}$
- **Radiation and relativistic matter:** Pressure is related to the energy-density of relativistic matter as $P = 1/3\rho$. This includes photons and neutrinos whose density scales with scale factor as $\rho \propto a^{-4}$
- **Dark Energy:** It is a hypothetical form of energy which is responsible for late time cosmic acceleration. The equation of state parameter depends on the model of Dark Energy and in many of models the equation of state is time dependent. However the current data suggests the value equation of state parameter to be $w = -1$. Substituting it in the above equation we get $\rho \propto a^0$ and hence the cosmic dilution doesn't affect the dark energy density.

It is important here to note that the cosmic dilution has different effect on different components. While radiation component is subdominant in today's universe, it played a major role in the early universe. Fig. ?? shows the energy density of different components as a function of scale factor; as one expects at late times cosmological constant and matter are the dominant components, whereas at earlier times radiation plays a significant role in the evolution of background universe. With the density scaling relations in hand and substituting $a = 1/(1+z)$, we can

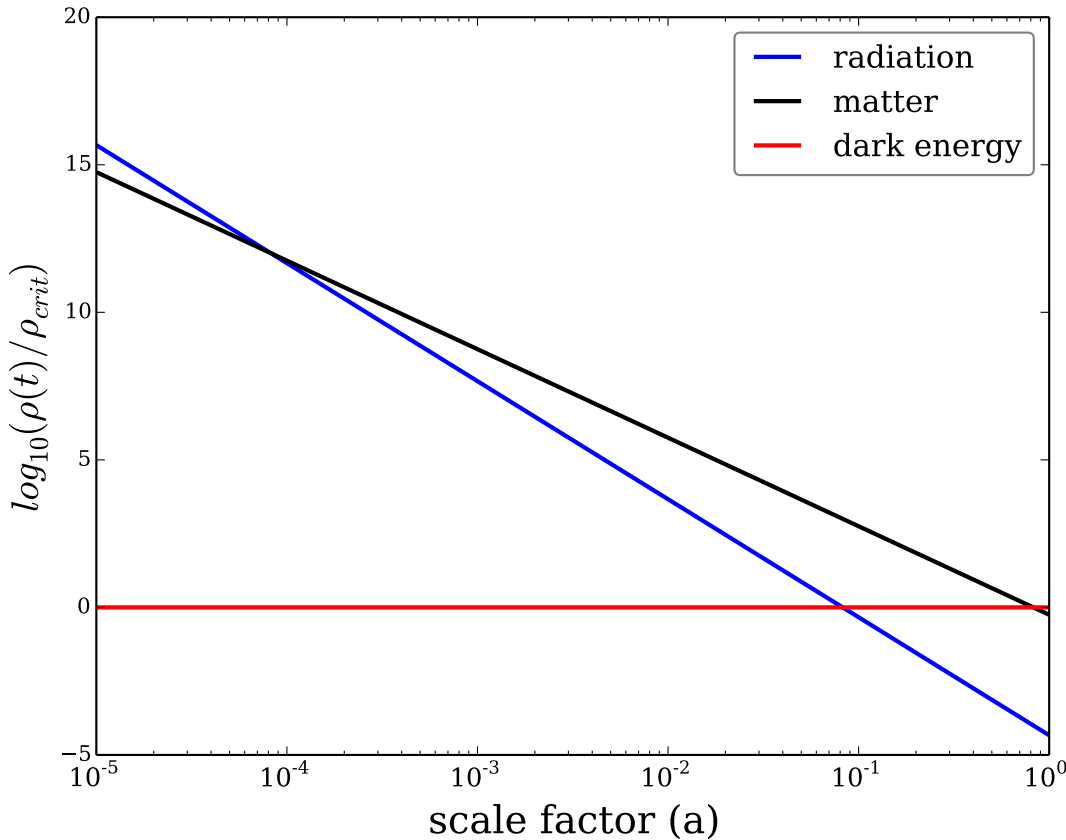


Figure 1.2: Scaling of various components as function of scale factor (a). While radiation is dominant component in the early universe, dark energy is dominant at present.

rewrite Eqn. 1.15 for a flat universe as

$$H^2(z) = H_0^2(\Omega_{ro}(1+z)^4 + \Omega_{mo}(1+z)^3 + \Omega_\Lambda) \quad (1.21)$$

where Ω_{ro}, Ω_{mo} and Ω_Λ are the density parameters of radiation, matter and dark energy respectively.

1.4 Cosmic Inventory

The above theoretical framework provides the evolution of different components as a function of scale factor. Now we look at the observational constraints obtained on these parameters. CMB temperature is measured precisely by the FIRAS instrument Mather et al. (1994) on COBE satellite Fixsen et al. (1996),

$T = 2.725 \text{ K} \pm 0.002\text{K}$. While neutrinos also contribute to radiation density, cosmic neutrinos have not been observed yet. For bosons such as photons the energy density as a function of temperature is given by

$$\rho_\gamma = \frac{\pi^2}{15} T^4 \quad (1.22)$$

which corresponds to

$$\Omega_\gamma = \frac{\rho_\gamma}{\rho_{crit}} = 5.04 * 10^{-5} \quad (1.23)$$

Unlike photons the energy density of baryons cannot be obtained by measuring its temperature, it needs to be measured directly. There are two main independent ways to measure the baryon density:

- Cosmic Microwave Background (CMB): by measuring the amplitude of the first and second peaks of CMB power spectrum
- Big Bang Nucleosynthesis (BBN): by measuring the primordial deuterium abundance.

From CMB power spectrum analysis we have $\Omega_b h^2 = 0.0224 \pm 0.0001$? and that from BBN is 0.0226 ± 0.00034 Cooke et al. (2016). Both of these measurements agree with each other remarkably well within error limits.

Dark matter forms 85% of total matter content in the universe. Unlike baryons, dark matter doesn't interact with the radiation. As dark matter interacts only gravitationally, by measuring the gravitational field in a given system we can infer the total mass content. One of the ways to measure the total matter (dark matter + baryon) is by using galaxy cluster gas mass fraction. Galaxy clusters (detailed review is in next chapter) are so large that the ratio of gas mass to that of total cluster mass is expected to reflect the ratio baryon to the total mass in the universeWhite et al. (1993); Grego et al. (2001). Constraints on dark matter density as measured by *Planck* is $\Omega_{dm} h^2 = 0.120 \pm 0.001$?.

As per current cosmological observations the major contribution for the energy density content in the universe is from dark energy. There are several observational probes to constrain this mysterious component which is responsible for the late time acceleration of the universe. The first direct observational evidence is from type Ia supernovae. Supernovae have constant intrinsic luminosity and are known as standard candles. Cosmologists measured the luminosity distance

(1.12) of type Ia supernovae as function of redshift to constrain $\Omega_\Lambda \approx 0.7$ Knop et al. (2003).

1.5 Cosmic Microwave Background

Cosmic Microwave Background (CMB) was theoretically predicted by George Gamov in 1940s as an observational relic of Hot Big Bang(HBB) model ?. It was observed accidentally by Aron Penzias and Robert Wilson in 1964 at the Bell Laboratories for which there were awarded Nobel prize in physics (1978) Penzias and Wilson (1965). Almost three decades after its discovery, Cosmic Background Explorer (COBE) detected anisotropies in CMB at a tiny level of 10 in a million. Far-Infrared Absolute Spectrophotometer (FIRAS) , an instrument mounted on COBE measured the black body temperature of CMB to be ~ 2.7 K. Since then a number of experiments have been designed to measure the anisotropies in the CMB.

High density and temperature of the early universe ensured that all the components interacted with each other multiple times remaining in thermal equilibrium. Photons (γ), protons (p) and electrons (e) were tightly coupled into a state called photon-baryon plasma; proton and electrons interacted with each other through Coulomb scattering and photon interacted with electrons through Thompson scattering:



As the universe expands energy density dilutes and the temperature decreases. When the temperature decreases below the ionization energy of hydrogen, $E < 13.6$ eV the equilibrium condition of Eq. 1.24 is distorted to $p + e^- \longrightarrow H + \gamma$ ². This results in the creation of neutral hydrogen atoms and the electron density decreases, which results in decoupling of photons from the photon-baryon plasma. This epoch is called the epoch of recombination; observations suggest that it happened at redshift of $z = 1089.90 \pm 0.23$?

As a radiation of the early universe, CMB provides a wealth of cosmological information. As inflation predicts the early universe is extremely homogenous with

²To be precise, recombination occurs at slightly lower temperature (1MeV) due to the large over abundance of photons with respect to baryons

inhomogeneities of the order of 10 in a million which is imprinted as anisotropies in CMB. Over the evolution of the universe slightly over dense regions of the early universe collapsed gravitationally to form the large scale structures that we see today. Analysing these structures involve complicated non-linear physics, however, CMB can be analysed linearly. In addition to that, $z \sim 1100$ provides long lever arm on the geometry of the universe.

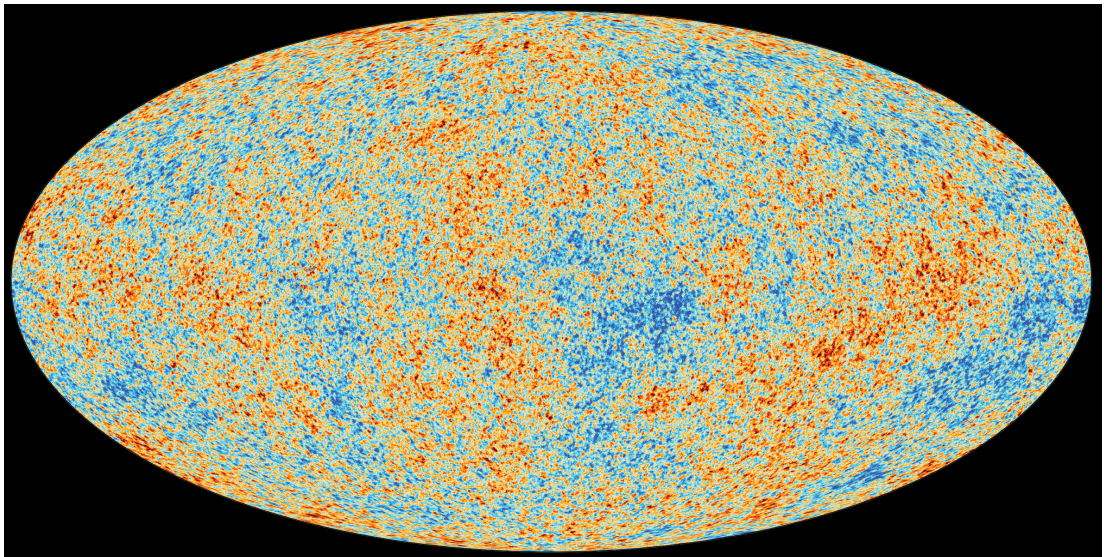


Figure 1.3: CMB as observed by *Planck* satellite. Credits: ESA/*Planck* collaboration

1.6 Boltzmann equations

In the early universe photons, baryons, and dark matter are tightly coupled to each other in a complicated way. The systematic way to understand these couplings is by using Boltzmann equations. Boltzmann equations are easier to solve in Fourier space, as different Fourier modes evolve independently in linear approximation. This section closely follows [Scott and Dodelson](#), here I summarize the Boltzmann equations for cold dark matter, photons, and baryons which were the dominant component of the universe at recombination.

The evolution of photon distribution is coupled to electrons and metric. Photon Boltzmann equation in the Fourier space is given by:

$$\dot{\tilde{T}} + ik(\hat{k} \cdot \hat{p})\tilde{T} + \dot{\tilde{\Phi}} + ik(\hat{k} \cdot \hat{p})\tilde{\Psi} = \dot{\tau}[\tilde{T}_0 - \tilde{T} + (\hat{k} \cdot \hat{p})\tilde{v}_b] \quad (1.26)$$

where T represents the photon temperature, \hat{p} is the photon direction, v_b is the electron velocity, and τ is the optical depth. Variables with \sim denotes Fourier transform, ones with $\dot{\cdot}$ denotes derivative with respect to conformal time η . $\dot{\tilde{\phi}}$ and $\dot{\tilde{\psi}}$ represent the conformal time derivative of the metric.

Cold dark matter (CDM) evolution is the simplest among all as it has only two free parameters velocity and density. CDM Boltzmann equation is given by:

$$\dot{\tilde{\delta}} + ik\tilde{v} + 3\dot{\tilde{\Phi}} = 0 \quad (1.27)$$

$$\dot{\tilde{v}} + \frac{\dot{a}}{a}\tilde{v} + ik\tilde{\Psi} = 0 \quad (1.28)$$

where v is the dark matter velocity, a is the scale factor, and δ is the fractional dark matter over density

$$\delta = \frac{\delta\rho}{\rho} \quad (1.29)$$

ρ is the dark matter density.

Proton and electrons are tightly coupled to each other by Coulomb forces. In addition to that the electrons also interact with photons through Thompson scattering. Both protons and electrons are analysed together as baryons, the Boltzmann equation for baryons is given by

$$\dot{\tilde{\delta}}_b + ik\tilde{v}_b + 3\dot{\tilde{\Phi}} = 0 \quad (1.30)$$

$$\dot{\tilde{v}}_b + \frac{\dot{a}}{a}\tilde{v}_b + ik\tilde{\Psi} = \dot{\tau} \frac{4\rho_\gamma}{3\rho_b} [3i\tilde{T}_1 + \tilde{v}_b] \quad (1.31)$$

where ρ_γ and ρ_b are the photon and baryon density respectively; T_1 is the first moment of photon temperature.

All the above Boltzmann equations can be solved numerically to a great precision for a given cosmological model by using publically available codes such as CAMB and CMBFAST.

1.7 Primary anisotropies

Temperature Power Spectrum:

The measured CMB temperature from a ground based experiment can be written as:

$$T = T_0(1 + \beta \cdot \hat{n} + \frac{T(\hat{n})}{T_0}) \quad (1.32)$$

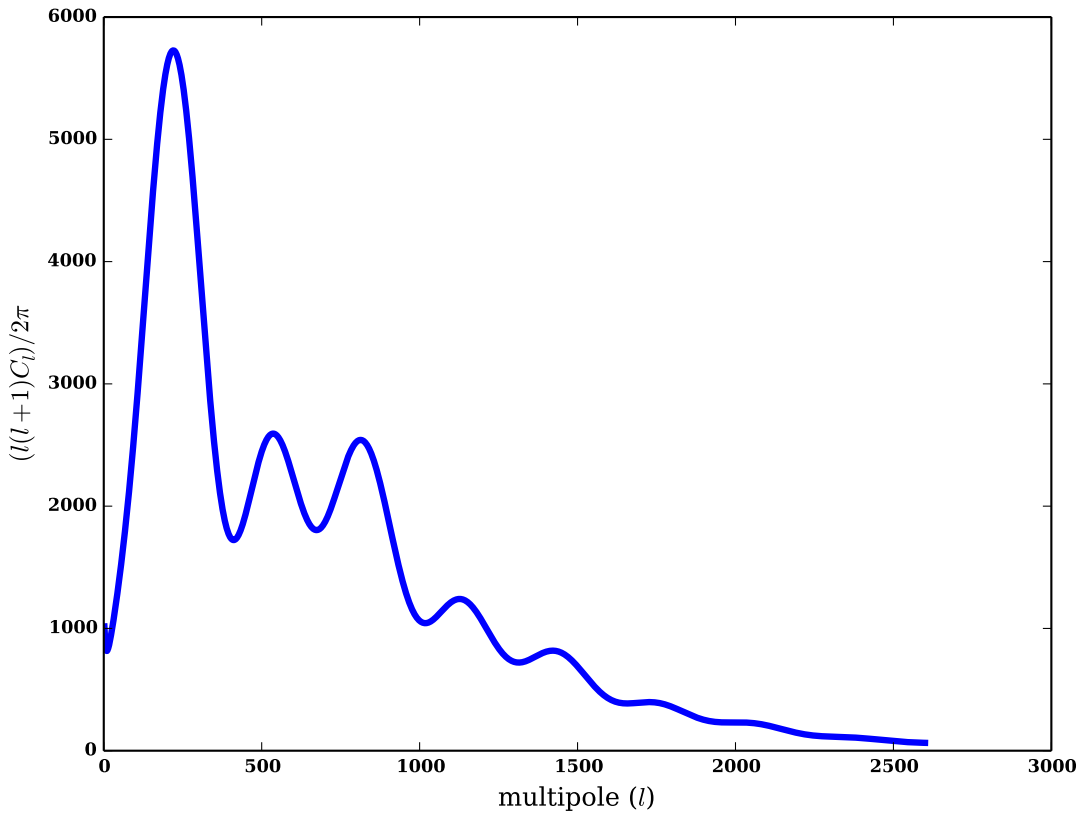


Figure 1.4: Angular power spectrum of CMB primary temperature anisotropies for *Planck* cosmology (Planck Collaboration et al., 2018).

where T_0 is the average CMB temperature, β is the dipole term due to the relative velocity of Earth with respect to Hubble flow which is equal to $\frac{v}{c}$ where v is the Earth's relative velocity. The last term in the equation represents the anisotropies in the CMB which here after we denote by $\Phi(\hat{n}) = \frac{T(\hat{n})}{T_0}$. Note that in the above equation we ignored the foregrounds, systematics, and experimental noise level.

Due to the intrinsic stochastic nature of fluctuations in CMB, we cannot predict the value of temperature at a given location, however, we can tackle the problem statistically. As a function on the surface of sphere, CMB fluctuations can be decomposed in terms of spherical harmonics as follows:

$$\Phi(\hat{n}) = \sum_l \sum_m a_{lm}^T Y_{lm}(\hat{n}) \quad (1.33)$$

$$a_{lm}^T = \int d\Omega \Phi(\hat{n}) Y_{lm}(\hat{n}) \quad (1.34)$$

where Y_{lm} are the spherical harmonic basis, a_{lm}^T are the harmonic coefficients. It

is important to note here that angular scale θ is related to multipole l as $\theta \sim 1/l$.

The randomness of the fluctuations wont let us predict the value of the harmonic coefficient a_{lm}^T . However, different theories predict the distribution from which the a_{lm}^T are picked. As per inflationary paradigm CMB fluctuations are a realisation of a Gaussian random field, then the distribution of harmonic coefficients is also Gaussian. The harmonic coefficients satisfy

$$\langle a_{lm}^T \rangle = 0, \quad (1.35)$$

$$\langle a_{lm}^T a_{l'm'}^{T*} \rangle = \delta_{ll'} \delta_{mm'} C_l^{TT}, \quad (1.36)$$

$$a_{l-m}^T = (-1)^m a_{lm}^{T*} \quad (1.37)$$

where $\langle \rangle$ denotes the ensemble average over many realisation, C_l^{TT} is the angular power spectrum of CMB.

Our universe is only one realisation of such Gaussian random field, however, we can still calculate the angular power spectrum. The idea is to replace the ensemble average with the spatial sample average i.e averaging over $2l+1$ samples.

$$\hat{C}_l^{TT} = \frac{1}{2l+1} \sum_m |a_{lm}^T|^2 \quad (1.38)$$

This measured power spectrum is fitted to the calculated power spectrum (as explained in 1.6) to extract cosmological information. For historical reasons the CMB power spectrum is conventionally parameterized as

$$D_l = \frac{l(l+1)}{2\pi} C_l. \quad (1.39)$$

CMB polarisation CMB is partially polarised (linear) at 10% level due to the Thompson scattering of photons by electrons at the surface of last scattering. Only anisotropic scattering results in polarisation. Before recombination photons and electrons were tightly coupled resulting no net local anisotropy. However, during the period of recombination there is slight anisotropy between photons and free electrons. Though CMB polarisation signal is weak compared to its temperature counterpart, it provides invaluable information on inflation and on late time evolution of universe through its lensing effects. In addition to that, foregrounds are only partially polarised. It was first detected observationally by Degree Angular Scale Interferometer (DASI) in 2002 Kovac et al. (2002).

Note that only quadrupole anisotropy is responsible for CMB polarisation as

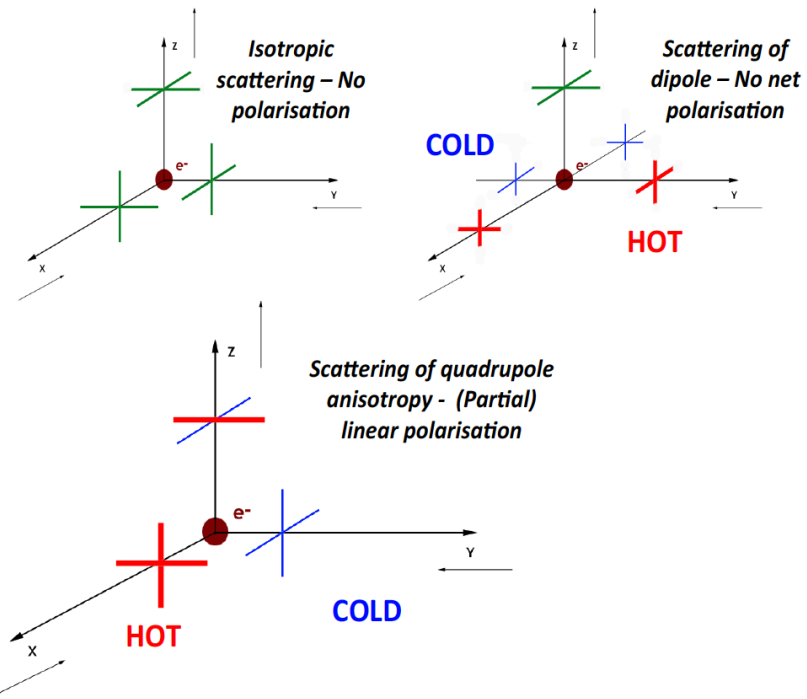


Figure 1.5: The above figure depicts important scenarios as experienced by an electron at the time recombination; it is adopted from the works of Hu and White (1997) and Dodelson (2003).

shown in Fig. 1.5. The above figure represents important scenarios experienced by electron at the time of recombination. Red and blue represent relatively hot and cold photons respectively; green represents the average temperature. Image on the top left represents the isotropic scenario which results in no net anisotropy. On the top right is that of dipole anisotropy which also results in no net polarisation. Only the quadrupole anisotropy which is shown in the bottom panel results in net linear polarisation.

Chapter 2

Cluster Cosmology

2.1 Overview

As described in the last chapter, on average the universe is homogenous - the expansion history, mean energy densities are reasonably well understood, at least empirically. However, the inhomogeneities in the universe in the form of large scale structures such as galaxies, cluster of galaxies etc., carry a wealth of cosmological information. Given that 85% of matter in the universe is made up of cold dark matter, the growth of cosmic structure can be attributed to two main factors mainly: gravitational growth of initial density perturbations controlled by expansion of space and baryonic physics. According to inflationary paradigm and also observationally corroborated by CMB data, the initial density perturbations are scale independent. The matter distribution at late times can be probed by number of different observations: galaxy redshift surveys, weak gravitational lensing, galaxy cluster abundance; latter being the focus of this chapter.

2.2 Linear theory of structure formation

In this section, I will describe the evolution of matter density perturbations in the linear regime (it closely follows Ryden 2003). Assuming that universe is filled with pressure less matter with mean mass density $\rho_m(t)$. By inducing a small density fluctuation ($\delta \ll 1$) within a region of spherical radius 'R'

$$\rho(t) = \rho_m(t)(1 + \delta). \quad (2.1)$$

The gravitational pull at the tip of the spherical region is given by

$$\ddot{R} = -\frac{GM}{R^2} \quad (2.2)$$

where M is the total mass within the sphere which by definition $M = 4\pi/3 \rho R^3$

$$\frac{\ddot{R}}{R} = -\frac{4\pi}{3}G\rho_m - \frac{4\pi}{3}G\rho_m\delta \quad (2.3)$$

As the universe expands the mass within the sphere remains constant

$$M = \frac{4\pi}{3}\rho_m(t)[1 + \delta(t)]R(t)^3 \quad (2.4)$$

From which we get

$$R(t) \propto \rho_m(t)^{-1/3}[1 + \delta(t)]^{-1/3} \quad (2.5)$$

since $\rho_m \propto a^{-3}$ in an expanding universe,

$$R(t) \propto a(t)[1 + \delta(t)]^{-1/3}. \quad (2.6)$$

Taking two time derivatives of the above equation we get

$$\frac{\ddot{R}}{R} = \frac{\ddot{a}}{a} - \frac{1}{3}\ddot{\delta} - \frac{2\dot{a}}{3a}\dot{\delta}. \quad (2.7)$$

Rearranging the above equations we get

$$\frac{\ddot{a}}{a} - \frac{1}{3}\ddot{\delta} - \frac{2\dot{a}}{3a}\dot{\delta} = -\frac{4\pi}{3}G\rho_m(1 - \delta) \quad (2.8)$$

$\frac{\ddot{a}}{a}$ is the expansion of the background universe, substituting $\delta = 0$ in the above equation we get

$$\frac{\ddot{a}}{a} = -\frac{4\pi}{3}G\rho_m. \quad (2.9)$$

Substituting the above relation in 2.8

$$-\frac{1}{3}\ddot{\delta} - \frac{2\dot{a}}{3a}\dot{\delta} = -\frac{4\pi}{3}G\rho_m\delta \quad (2.10)$$

or

$$\ddot{\delta} + 2H\dot{\delta} = 4\pi G\rho_m\delta \quad (2.11)$$

Considering the relativistic corrections the above equation changes to

$$\ddot{\delta} + 2H\dot{\delta} = \frac{4\pi G}{c^2}\rho_m\delta \quad (2.12)$$

In the early radiation dominated phase of the universe $\Omega_m \ll 1$ and $H = 1/(2t)$ which results in

$$\ddot{\delta} + \frac{1}{t}\dot{\delta} \approx 0, \quad (2.13)$$

solving which we get,

$$\delta(t) \approx C_1 + C_2 \ln t \quad (2.14)$$

During the radiation dominated epoch, baryon density oscillated as baryons and photons were tightly coupled. Whereas the dark matter density grew at a logarithmic rate as predicted by the above equation. Similarly, during the dark energy dominated epoch 2.12 takes the form

$$\ddot{\delta} + 2H_\Lambda \dot{\delta} \approx 0 \quad (2.15)$$

which results in

$$\delta(t) \approx D_1 + D_2 e^{-2H_\Lambda t}. \quad (2.16)$$

Dark matter density perturbation exponentially decays off in dark energy dominated epoch.

Only during the matter dominated epoch, density perturbations grow

$$\ddot{\delta} + \frac{4}{3t}\dot{\delta} - \frac{2}{3t^2}\delta = 0. \quad (2.17)$$

Assuming a power law solution of the form Dt^n and plugging it in above equation we get

$$\delta(t) \approx D_1 t^{2/3} + D_2 t^{-1}. \quad (2.18)$$

2.3 Power spectrum

In Fourier space the perturbations can be written as

$$\delta_k = \frac{1}{V} \int_0^\infty \delta(x) e^{ik \cdot x} d^3x. \quad (2.19)$$

The matter power spectrum and auto correlation are related as follows:

$$\langle \delta(x)\delta^*(x) \rangle = \int_0^\infty \frac{dk}{k} \frac{k^3 |\delta^2(k)|}{2\pi^2} = \int_0^\infty \frac{dk}{k} \frac{k^3 P(k)}{2\pi^2} \quad (2.20)$$

where by definition $P(k) = |\delta^2(k)|$. According to inflationary paradigm the primordial fluctuations are nothing but macroscopic manifestations of quantum fluc-

tuations. As proposed by Harrison and Zel'dovich, these primordial fluctuations are scale-invariant ¹

$$P_{\text{primordial}}(k) \propto k \quad (2.21)$$

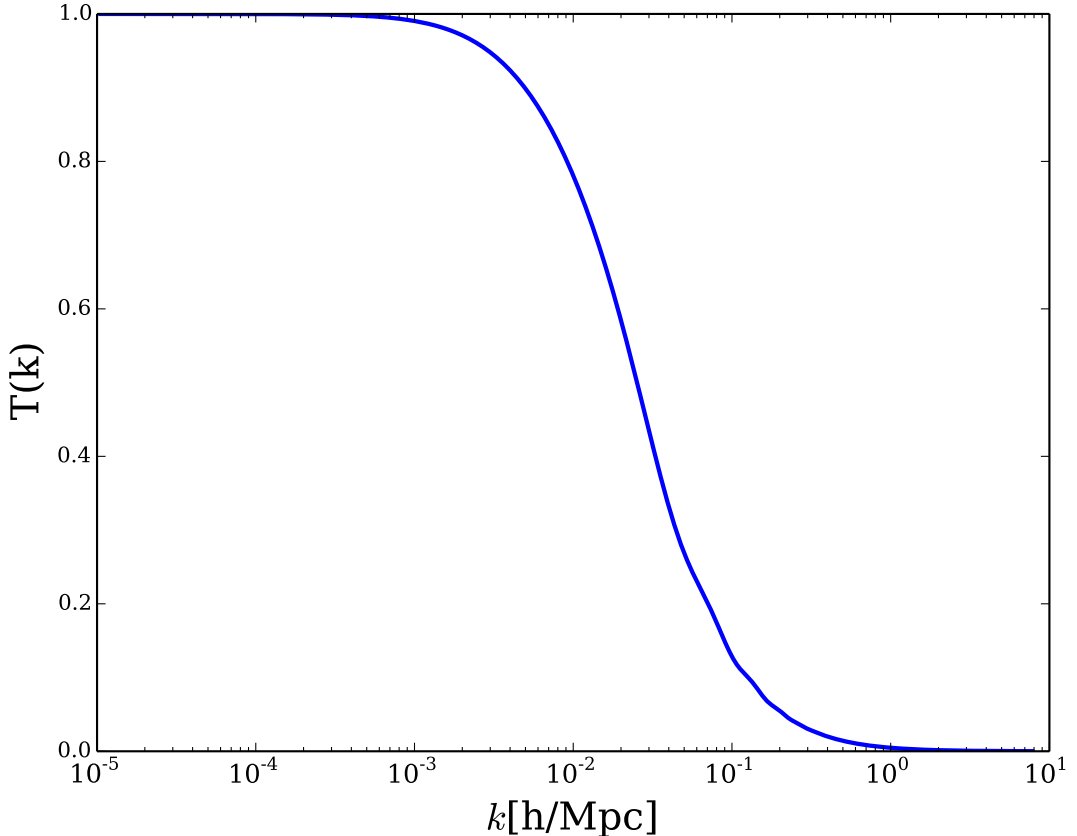


Figure 2.1: Total transfer function (CDM+baryon+neutrinos) as calculated by *CAMB*.

The primordial densities grow in a complicated way as explained in the previous section; the evolved matter power spectrum can be written as function redshift and wave number as

$$P(k, z) = P_{\text{primordial}}(k) D(z)^2 T(k, z)^2 \quad (2.22)$$

where $D(z)$ is the growth factor and $T(k, z)$ is the transfer function. Growth factor

¹otherwise it would imply a preferred mass scale for fluctuations entering the horizon

for cold dark matter is given by

$$D(z) = H(z) \int_z^\infty \frac{dz'(1+z')}{H^3(z')}.$$
 (2.23)

The transfer function depends on the complex interactions between various components in the universe. While there are approximated expression for transfer function, however, the exact solution of the transfer function can only be obtained numerically. Numerical codes such as CAMB, CLASS etc., solve the multi-component Boltzmann equations to provide $T(k,z)$ for a given set of parameters.

The shape of transfer function gives insight into the growth of perturbations. At early phase of the universe during radiation dominated epoch, super horizon scales grew according to the growth factor $D(z)$ as the transfer function is unity. However, sub horizon perturbations grow only logarithmically; smaller modes entered horizon earlier than longer modes, hence had more logarithmic growth. After matter-radiation equality, perturbations grew equally on all scales. The wiggles in the transfer function at intermediate scales is due to Baryon Acoustic Oscillations (BAO). Before recombination, photons and baryons were tightly coupled, baryons experienced two opposing forces: gravitational pull due to dark matter potential well and pressure due to the radiation component resulting in oscillations of photon-baryon plasma. However, at recombination photons-baryons decouple and the baryon perturbations evolve according to the background universe. This length scale can be used as a standard ruler to measure the geometry of the universe Chang et al. (2008).

Fig. 2.2 shows the matter power spectrum at two different redshifts for *Planck* 2018 cosmological parameters. The power at large scales i.e., $k < k_{eq}$ obtained by multiplying the primordial power spectrum with growth factor (as transfer function is unity at those scales). As one expects, the maximum of the power spectrum is directly linked to the horizon at matter-radiation equality, $k_{eq} = 0.01$.

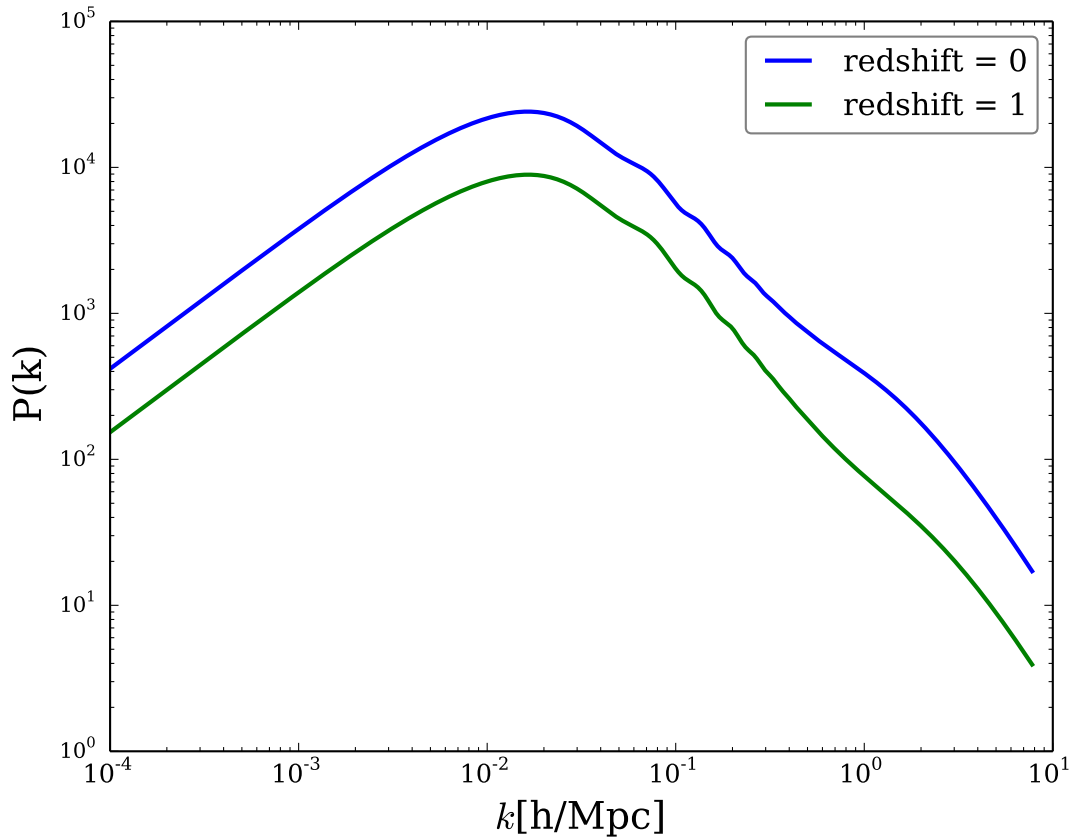


Figure 2.2: Total matter power spectrum generated by *CAMB* for two different redshifts.

2.4 Statistics of spherically collapsed objects

In the previous sections we derived equations for density perturbations in both real and Fourier space. However, in practice, we observe the density contrast, which is nothing but density perturbation averaged over a given volume. Mathematically, density contrast within a radius ‘R’ is given by

$$\delta(x, R) = \int d^3x' W(|x' - x|) \delta(x') \quad (2.24)$$

$$\delta(k, R) = W(k, R) \delta(k) \quad (2.25)$$

The variation of fluctuation at scale R is given by

$$\sigma^2(R) = \langle \delta^2(x, R) \rangle = \int dl n k \nabla^2(k) |W(k, R)|^2 \quad (2.26)$$

where $\nabla(k)$ is the dimensionless power spectrum. Assuming that the density field follows Gaussian random distribution, the probability that the sphere of radius has density contrast δ is given by

$$P(\delta, R) = \frac{1}{\sqrt{(2\pi\sigma^2(R))}} \exp\left(-\frac{\delta^2}{2\sigma^2(R)}\right) d\delta. \quad (2.27)$$

It is important to note here that $P(\delta, R) = P(\delta, M)$, where R is related to M as $M = \frac{4\pi}{3}R^3$

2.4.1 The Press-Schechter Theory

In 1974 Press-Schechter came up with a simplistic model to predict the number of dark matter halos. The basic idea is that a sphere of radius ‘R’ with density contrast δ will form a dark matter if δ greater than a critical value δ_c . The probability of finding dark matter halos with mass greater than M is given by

$$F(M) = \int_{\delta_c}^{\infty} P(\delta, M) d\delta = \frac{1}{2} \operatorname{erfc}\left(\frac{\nu}{\sqrt(2)}\right) \quad (2.28)$$

where $\nu = \delta_c/\sigma(M)$. The halo mass function, i.e, the number density of halos between mass M and $M+dM$ is given by

$$\frac{dn(M, z)}{dM} = -\sqrt{\frac{2}{\pi}} \frac{\rho_m}{M} \frac{\delta_c}{\sigma^2(M, z)} \frac{d\sigma(M, z)}{dM} \exp\left(-\frac{\delta_c^2}{2\sigma^2(M, z)}\right). \quad (2.29)$$

The above equation predicts too many low-mass halos and too few high-mass halos compared to the N-body simulations. For precise cosmological applications, the statistics rely on some form of 2.29 equation with some additional fitting parameters to achieve a better fit, for example Tinker et al. (2008); Jenkins et al. (2001).

2.5 Galaxy Clusters & Cosmology

Galaxy clusters:

Galaxy clusters are the largest gravitationally bound objects in the universe with ten-thousands of galaxies. These are the most massive objects, typically the mass within virial radius ranges from $10^{14} - 10^{15} M_\odot$. The majority the mass is in the form of invisible dark matter (80-87%), which generally follows a spherically symmetric Navarro-Frenk-White model (NFW Navarro et al. (1997)). Around

12% of the cluster mass is in the form of hot intracluster medium (ICM)- sparse plasma that fills the cluster. The temperature of the ICM is of the order of ten million Kelvin and thus predominantly emits in X-rays. Remaining 2% of the cluster mass is in the form of stars, cold gas, and dust in galaxies.

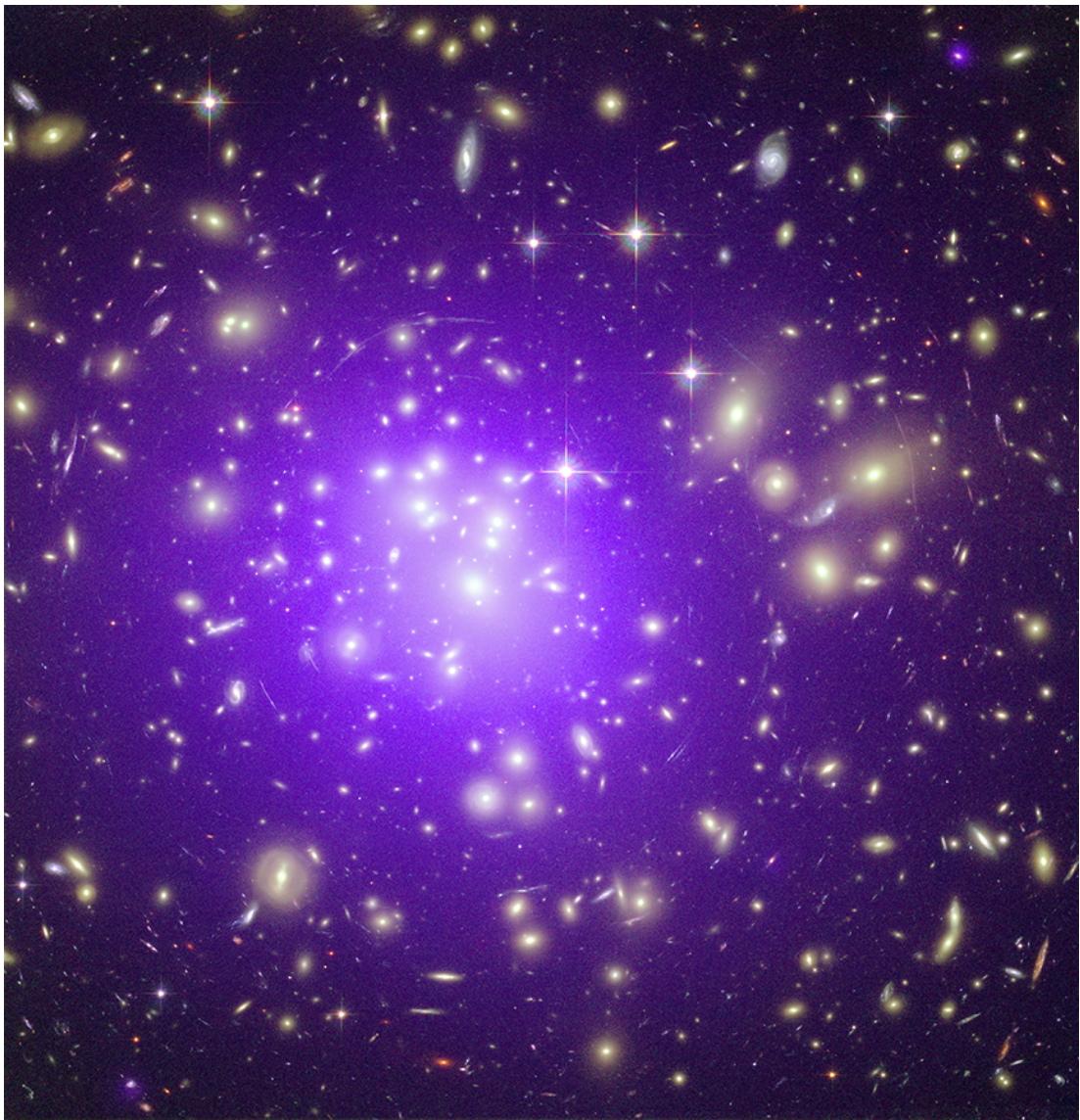


Figure 2.3: Galaxy cluster Abell 1689. Credits: HST/Chandra X-ray observatory

Fig. 2.3 shows the image of a galaxy cluster Abell 1689 which is in constellation Virgo. The X-ray emission due to hot ICM is shown as purple in the image; galaxies from the optical data are coloured yellow. The long arcs in the optical image is caused by distortion due to gravitational lensing.

Cluster cosmology:

Clusters have historical significance in providing crucial information about underlying cosmological model. Dark matter was discovered in Coma cluster in 1930s, when Fritz Zwicky observed that galaxies in cluster were moving too fast to be held by the gravitational pull of the visible galaxies. In the 1990s cluster provided evidence for low matter density universe White et al. (1993).

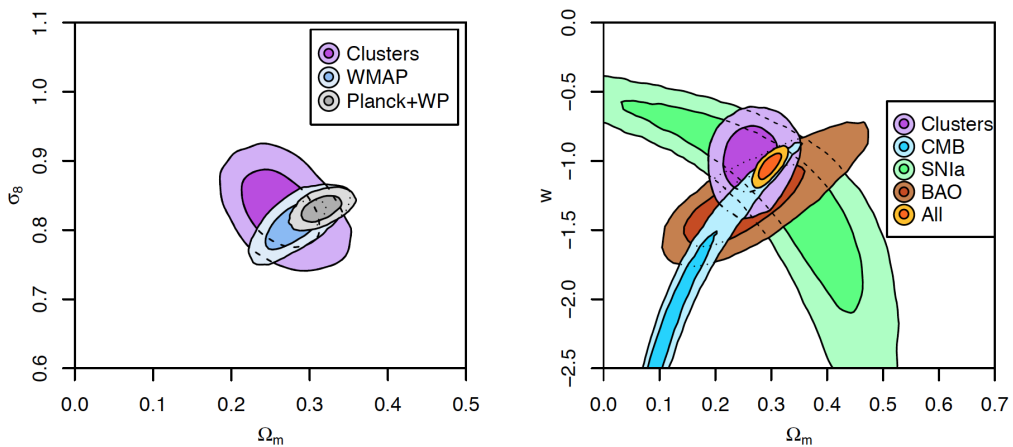


Figure 2.4: On the left is flat Λ CDM model: constraints on Ω_m and σ_8 from clusters in purple, from CMB observations in blue (*Planck*) and grey (*Planck* and WMAP). On the right we have flat w CDM: constraints on w and Ω_m for various cosmological probes. Cluster (purple) provide the tightest single-probe constraints.

As seen in 2.4.1, halo/cluster abundance as a function of mass is sensitive to cosmological parameter such as Ω_m and σ_8 . In addition to that, clusters are powerful probes of dark energy. The dark energy effects the evolution of universe in two different ways. First, it accelerates the expansion of the universe. Second, it acts as anti gravity and hence slows down the structure formation. Cluster number count is sensitive to both of these effects: the abundance and the correlation function of galaxy clusters depend on expansion history and structure growth. Constraints obtained on Ω_m , σ_8 , and dark energy equation of state parameter, w , is show Fig 2.4. As can be inferred from the plot, cluster constraints are complementary to that of CMB anisotropies. For the above constraints, only 241 clusters from ROSAT all sky survey were used Mantz et al. (2015). Given the statistical power of ongoing and future surveys, galaxy clusters have become indispensable probes of cosmology. The Simons Observatory Collaboration et al.

(2019); Benson et al. (2014).

2.5.1 Limited by mass estimation

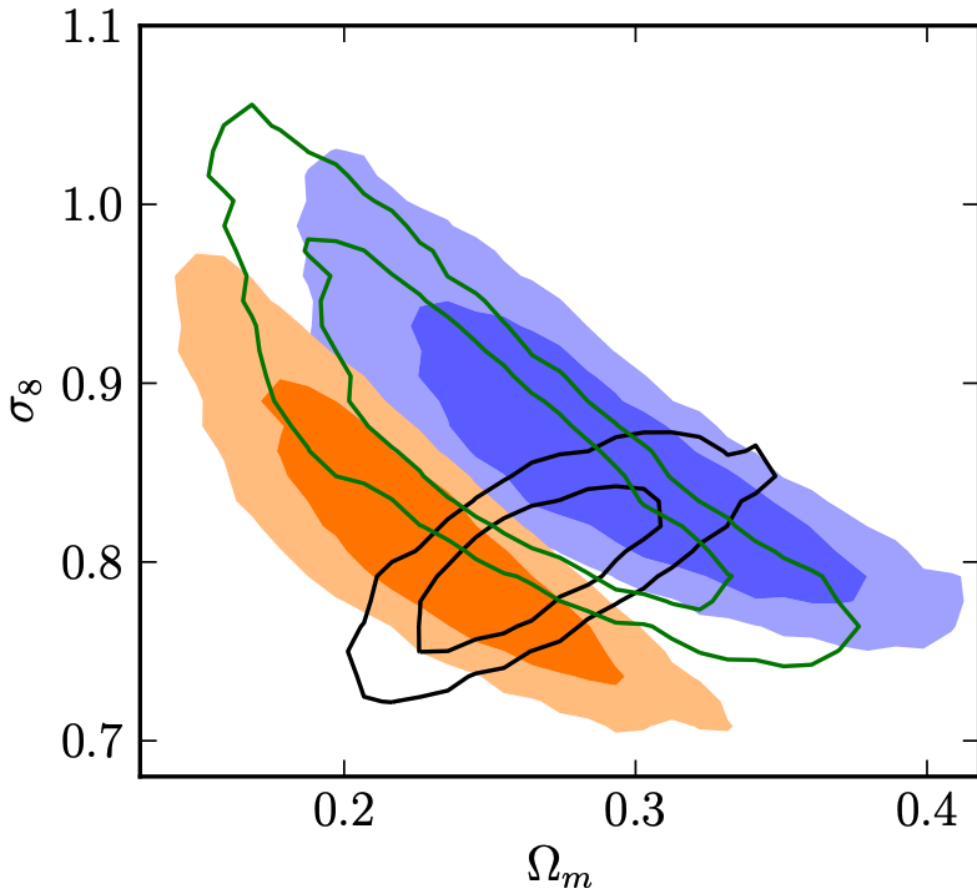


Figure 2.5: Effects of systematics in mass estimation on cluster cosmology.

While clusters are powerful probes of cosmology, they are currently limited by fidelity of mass estimation. Many ways to measure the cluster mass relate the cluster observable O to the cluster mass through a parametric relation

$$O = AM^B f(z)^C + D \quad (2.30)$$

where A is the normalisation parameter, D is the intrinsic scatter, B and C are the mass and redshift evolution parameters respectively. The parametric relation depends on the complicated baryonic physics which is not well understood, any deviation in the physics will eventually effect cluster cosmology. Fig. 2.5 shows the systematic effects of mass estimation on cosmological parameters Ω_m and

σ_8 . Black contour represents the cosmological constraints obtained using CMB, coloured contours represent constraints due to cluster number count. Cluster number count provides complementary constraints, however, any systematic in mass estimation will eventually lead to systematics in cosmological parameters Hasselfield et al. (2013).

Accurate cluster mass estimation is essential in order to fully realise the potential of cluster cosmology. One of the ways to obtain robust cluster mass is through gravitational lensing. Unlike the mass observable scaling relation, cluster mass estimation through lensing of a background source is independent of baryonic physics. The background source can either optical or CMB. However, the probability finding an optical source behind a galaxy cluster of high redshift ($z > 1$) decreases exponentially. On the other hand CMB is at precise redshift of $z = 1100$, well behind all the clusters. In addition to that, statistical properties of CMB are very well studied. The rest of the chapters focus on various methods we have developed to extract lensing signal from CMB data, the data used, and the results we have obtained.

Chapter 3

Maximum Likelihood Estimator

Overview

In literature, there are several methods to extract lensing signal from CMB data (Dodelson, 2004; Lewis and Challinor, 2006; Baxter et al., 2015; Hu et al., 2007; Melin and Bartlett, 2015; Yoo and Zaldarriaga, 2008; Horowitz et al., 2019; Raghunathan et al., 2017). During my thesis, I mainly worked on two methods: Maximum Likelihood Estimator (MLE) and Quadratic Estimator (QE). This chapter is organised as follows. In §3.1, I provide a brief overview of CMB-cluster lensing, followed by description of MLE in §3.2. The performance of MLE and QE is compared in §3.3 and several sources of systematics are quantified in §3.4. The forecasts for future surveys are provided in §3.5 and the conclusions in §3.6. This chapter closely follows Raghunathan et al. (2017).

3.1 CMB lensing overview

While passing through the intervening galaxy cluster, Cosmic Microwave Background (CMB) photons are deflected due to the cluster's gravitational potential. The resulting distortion in the path of CMB photons is called CMB-cluster lensing. The distortion pattern can be understood with our prior knowledge of CMB. Typically the angular size of galaxy cluster is of the order of a few arcminutes (for clusters above $z > 0.3$). On these scales, CMB has no power due to diffusion damping (Silk, 1968) and can be approximated as a gradient. Gravitational lensing by a galaxy cluster induces a dipole kind of structure on top of the background gradient with hot and cold spots swapped. As CMB is polarised at 10% level, lensing signal in polarisation is also an order of magnitude smaller than that of temperature.

Fig 3.1 shows the lensing signal for a cluster of mass $5 \times 10^{14} M_{\odot}$ and at redshift of $z = 0.7$. In the left panels of Fig 3.1, we have the background CMB gradient for the temperature and polarisation stokes Q/U parameters, in the

middle panel we have the corresponding lensed maps and in the right panel we have the lensing dipole signatures.

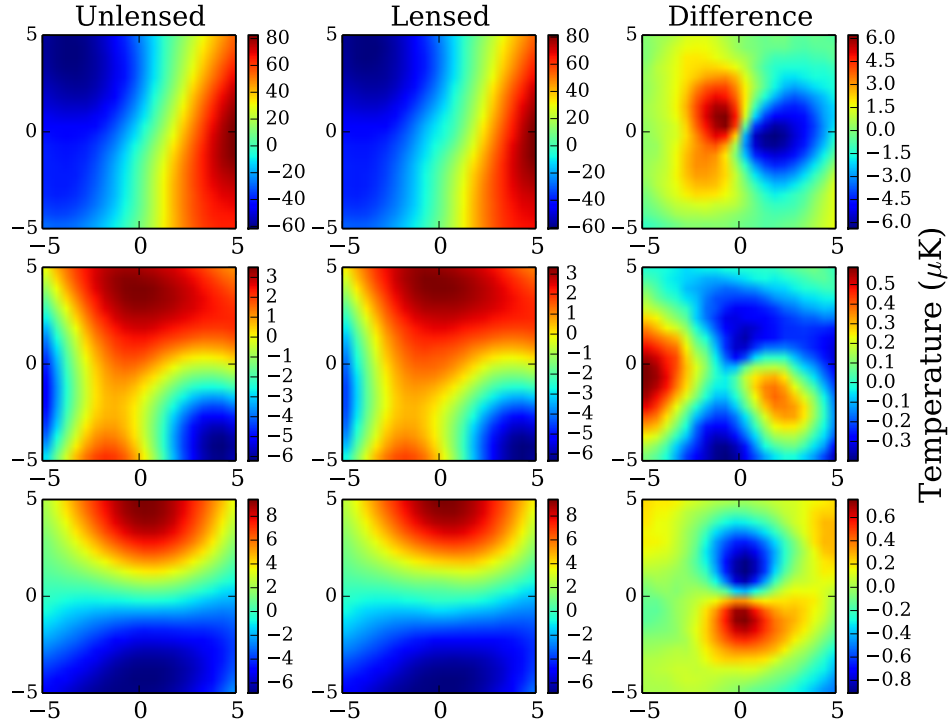


Figure 3.1: Lensing effect on CMB due to a galaxy cluster of mass $5 \times 10^{14} M_{\odot}$. On the top panel we show the effect of cluster lensing on CMB temperature field. Bottom two panels are for the stokes Q and U parameters. The lensing signal for temperature is few μK and an order of magnitude smaller in polarisation. Note that in the above simulation we haven't used either experimental noise or foregrounds.

The deflection induced due to lensing is nothing but remapping of the unlensed CMB temperature and polarisation fields based on the gravitational deflection angle. Mathematically lensing is expressed by the following equations

$$T(\hat{n}) = \tilde{T}(\hat{n} + \vec{\alpha}(\hat{n})) \quad (3.1)$$

$$Q(\hat{n}) = \tilde{Q}(\hat{n} + \vec{\alpha}(\hat{n})) \quad (3.2)$$

$$U(\hat{n}) = \tilde{U}(\hat{n} + \vec{\alpha}(\hat{n})) \quad (3.3)$$

where $\tilde{\cdot}$ represents unlensed fields, T represents the temperature field, Q and U are the stokes polarisation parameters respectively. $\vec{\alpha}(\hat{n})$ is the deflection angle along the \hat{n} direction.

Deflection field:

Deflection field depends on the density profile of a galaxy cluster. Here we provide a detailed calculation of deflection field for spherically symmetric Navarro-Frenk-White (NFW) density profile Navarro et al. (1996). Lensing convergence is related to deflection field as

$$k = \frac{1}{2} \nabla \cdot \vec{\alpha} \quad (3.4)$$

where α is the deflection angle, k is the lensing convergence profile. For symmetrical density profiles, the lensing convergence is equal to the ratio of surface mass density over the critical surface density of the Universe at the cluster redshift, $k = \frac{\Sigma(x)}{\Sigma_{crit}}$. The surface mass density or also known as the projected mass density of the halo is obtained by integrating the halo density profile along the line of sight.

$$\Sigma(x) = 2 \int_0^\infty \rho(r) ds \quad (3.5)$$

where r is the radial distance, x is the corresponding two-dimensional planar distance and s is distance along the line of sight with $s = 0$ being the plane of the cluster. The critical surface density of the Universe at cluster redshift is given by

$$\Sigma_{crit} = \frac{c^2}{4\pi G} \frac{D_{cmb}}{D_{clus} D_{cmb,clus}} \quad (3.6)$$

where D_{cmb} is the comoving distance to the epoch of recombination ($z=1100$), D_{clus} is the comoving distance to the cluster, and $D_{cmb,clus}$ is the comoving distance between the CMB and the cluster.

Unless otherwise mentioned, we define all the cluster quantities in this chapter with respect to R_{200} , which is defined as the radius within which the mean cluster density is 200 times the critical surface density of the Universe at cluster redshift $\rho_{crit}(z)$. By definition M_{200} is given by

$$M_{200} = \int_0^{R_{200}} 4\pi x^2 \rho(x) dx, \quad (3.7)$$

M_{200} can also be written as

$$M_{200} = \frac{800\pi}{3} R_{200}^3 \rho_{crit}. \quad (3.8)$$

The above mathematical equations hold for any spherically symmetric halo. Here we consider a specific case of Navarro Frenk White (NFW) halo density profile. In the NFW profile, the density of the dark matter halo as a function of radius is given by:

$$\rho(r) = \frac{\delta_c \rho_{crit}(z)}{\left(\frac{r}{R_s}\right)\left(1 + \frac{r}{R_s}\right)^2} \quad (3.9)$$

where δ_c is the characteristic over-density, R_s is the characteristic scale radius, and c is the dimensionless concentration parameter. The dimensionless over-density is given by $\delta_c = \rho_0/\rho_{crit}(z)$, where ρ_0 is the cluster central density and $\rho_{crit}(z)$ is the critical density of the universe at cluster redshift. Plugging the above equation in 3.5, we get the surface density for the NFW halo. By changing the variables of integration to $s = \sqrt{r^2 - x^2}$ and $ds = \frac{rdr}{\sqrt{r^2 - x^2}}$ we obtain:

$$\Sigma(x) = 2\delta_c \rho_{crit}(z) R_s^3 \int_x^\infty \frac{1}{r(R_s + r)^2} \frac{rdr}{\sqrt{r^2 - x^2}} \quad (3.10)$$

The scale radius is related to the concentration parameter as follows:

$$c = \frac{R_{200}}{R_s}, \quad (3.11)$$

we have set $c = 3.0$ following Bhattacharya et al. (2013).

Eqn. 3.10 can be solved analytically and the explicit closed-form expression for the NFW case is given by Bartelmann (1996). With $\Sigma(x)$ and Σ_{crit} in hand we can use Eq. 3.4 to get the lensing deflection angle as function of cluster mass and redshift. Unless otherwise mentioned we assume the galaxy clusters follow the NFW profile. However, the mathematical framework described above can be applied to any halo density profile.

3.2 Maximum Likelihood Estimator

We developed the maximum likelihood estimator to constrain the CMB cluster lensing signal. The unlensed CMB can be assumed to be a Gaussian random field to a very good approximation (Planck Collaboration et al., 2014b). CMB-cluster cluster lensing remaps this Gaussian random field based on the deflection

angle. The remapping can be modeled in the form of a covariance between the data pixels. First, we describe the likelihood estimation in § 3.2, followed by covariance matrix calculation in § 3.2.1.

Likelihood Estimation

The likelihood of observing a particular set of pixelized values ‘ d ’ is given by

$$-2\ln L(d|\Sigma_{lens}) = \ln|\Sigma_{lens}| + d^T \Sigma_{lens}^{-1} d, \quad (3.12)$$

where Σ_{lens} is the covariance matrix which acts as a model, d is the pixel values of the observed temperature or polarisation maps.

Lensing signal of a single galaxy cluster is too weak to be detected. We stack many clusters to increase SNR (signal to noise ratio) to a reasonable level

$$-2\ln L(d|\Sigma_{lens})_{tot} = \sum_{i=0}^n w_i [\ln|\Sigma_{lens}| + d_i^T \Sigma_{lens}^{-1} d_i] \quad (3.13)$$

where n is the total number of clusters in the sample, w_i is the weight assigned to the i^{th} cluster. Here we assign equal weights to all clusters ($w_i = 1$) as we are using simulations and it is not the case while using real data.

3.2.1 Covariance matrix calculation

We calculate the covariance matrix using a set of simulated skies¹. To simulate the lensed CMB sky, we first generate the large-scale structure lensed CMB power spectra (C_l^{TT} , C_l^{TE} , C_l^{EE} , and C_l^{BB}) from CAMB for the *Planck* cosmology (Planck Collaboration et al., 2016b). We generate Gaussian random realisations of these power spectra on a $50' \times 50'$ box at $0.25'$ resolution. The generated E and B maps are converted to Q and U maps using:

$$E_l \pm iB_l = - \int d^2\hat{n} e^{-i\hat{n}\cdot l} [Q \pm iU](\hat{n}) e^{\mp 2i\phi_l} \quad (3.14)$$

where ϕ_l is the angle of l as measured from stokes Q axis.

These Gaussian realizations are then lensed by the deflection field (which is obtained as explained in 3.1). We take out the central $10' \times 10'$ for covariance matrix calculation.² The lensing signal is of the order of few arcminutes even for

¹more details about simulations are provided in A.2

²lensing maps are generated on $50' \times 50'$ to take into account the large scale gradient on which the lensing signal is linearly dependent

a massive cluster and most of the lensing signal is within a radial distance of $10'$ from the cluster center. Increasing the boxsize to $14' \times 14'$ increases the SNR by $\leq 1\%$, while increasing the computational complexity by multiple folds.

With simulated lensed CMB maps in hand we calculate the covariance matrix as follows

$$\Sigma_{lens}(M, z) = \langle (\mathbf{G} - \langle \mathbf{G} \rangle)(\mathbf{G} - \langle \mathbf{G} \rangle)^T \rangle \quad (3.15)$$

$$= \frac{1}{n-1} \sum_{i=0}^n (\mathbf{G}_i - \langle \mathbf{G} \rangle)(\mathbf{G}_i - \langle \mathbf{G} \rangle)^T \quad (3.16)$$

where vector G_i is either the polarisation or temperature simulated data for the i^{th} sky realisation and $\langle \rangle$ represents the ensemble average. The number of simulated skies depend on the number of degrees of freedom in the covariance matrix. In our case, the maximum number of degrees of freedom is for the polarisation estimator (concatenated Q/U or E/B maps), for which the covariance matrix is an 800×800 matrix. Number of simulations scale as twice the number of elements in the covariance matrix. We found that 1,30,000 simulations are sufficient to recover cluster masses without any detectable bias. We then multiply Hartlap correction term $\frac{(n_{sims}-n_d-1)}{n_{sims}}$, where n_{sims} is 1,30,000 and n_d is the length of the data vector 400(800) for T(QU), to remove any possible bias in Σ_{lens}^{-1} due to the limited number of simulations.

We also use these simulated skies to quantify the effects of statistical and systematic uncertainties. There are several astrophysical sources which act as a systematic bias for the CMB-cluster lensing analysis. In this work we consider clusters own SZ effects such as thermal Sunayev-Zel'dovich (tSZ) and kinematic Sunayev-Zel'dovich effects. Along with these SZ effects, we have also considered sources which are uncorrelated with cluster, such as tSZ effect from other halos, dusty star forming galaxies (DSFGs), and radio galaxies. In appendix, we provide more details about the addition of these foregrounds to simulated skies.

Here we have used simulations to check the performance of MLE and also to quantify the effect of systematics. Unless otherwise mentioned all the clusters are simulated at a mass of $M_{200} = 2 * 10^{14} M_\odot$ and at redshift of 0.7. For covariance matrix calculation we simulate the clusters at redshift of 0.7 with mass resolution of $2 * 10^{12} M_\odot$. Note that such fine gridding might not be computationally feasible for data where the clusters span a wide range of masses and redshifts. An optimal

solution would be to generate the covariance matrices on coarser grid of mass and redshift and then interpolating it on a finer grid.

3.3 Results

In this section, we first validate our pipeline using simulations and we report the expected mass uncertainties for the polarisation and temperature MLE. Then we compare the performance of MLE and QE for ideal simulations by varying only the experimental noise levels and not including any galactic or extra galactic foregrounds. Later, we compare the performance of the estimators in the presence of foregrounds. In this chapter all the results are for a set of 100,000 simulated clusters (expected number of clusters for CMB-S4) each at a mass of $2 \times 10^{14} M_\odot$ and at redshift of 0.7.

3.3.1 *Idealised simulations*

Our baseline simulations include only experimental white noise level. These idealised simulations serve two purposes:

- serve as benchmark to estimate the effect of different systematic and statistical sources of uncertainties on lensing analysis.
- in addition to that, it provides equivalent conditions to allow for a fair comparison between MLE and QE.

To validate the pipeline we simulate 100,000 galaxy clusters each at a mass of $2 \times 10^{14} M_\odot$ and at redshift of $z = 0.7$. We add a white noise realisation of rms $1\mu\text{K}'$ for temperature maps and rms $\sqrt{2}\mu\text{K}'$ to polarisation maps. These simulations are then convolved by a beam of FWHM $1'$ and then passed through our pipeline. The results are shown in the top panel of Fig. 3.2, the black solid line represents the combined likelihood for temperature MLE estimator and solid (dashed) orange curve is that for the polarisation QU (EB) estimator. We calculate the detection significance as mentioned above and measured a lensing significance of 400σ and 110σ for temperature and polarisation MLE respectively. Null test results are shown in the bottom panel of Fig. 3.2, for which we turned off lensing in our pipeline. As expected likelihoods for all the three MLE estimators (T, QU, and EB) peak at zero mass.

In the left panel of Fig. 3.3, we compare the performances of the three MLE estimators and the temperature QE estimator as a function of experimental noise

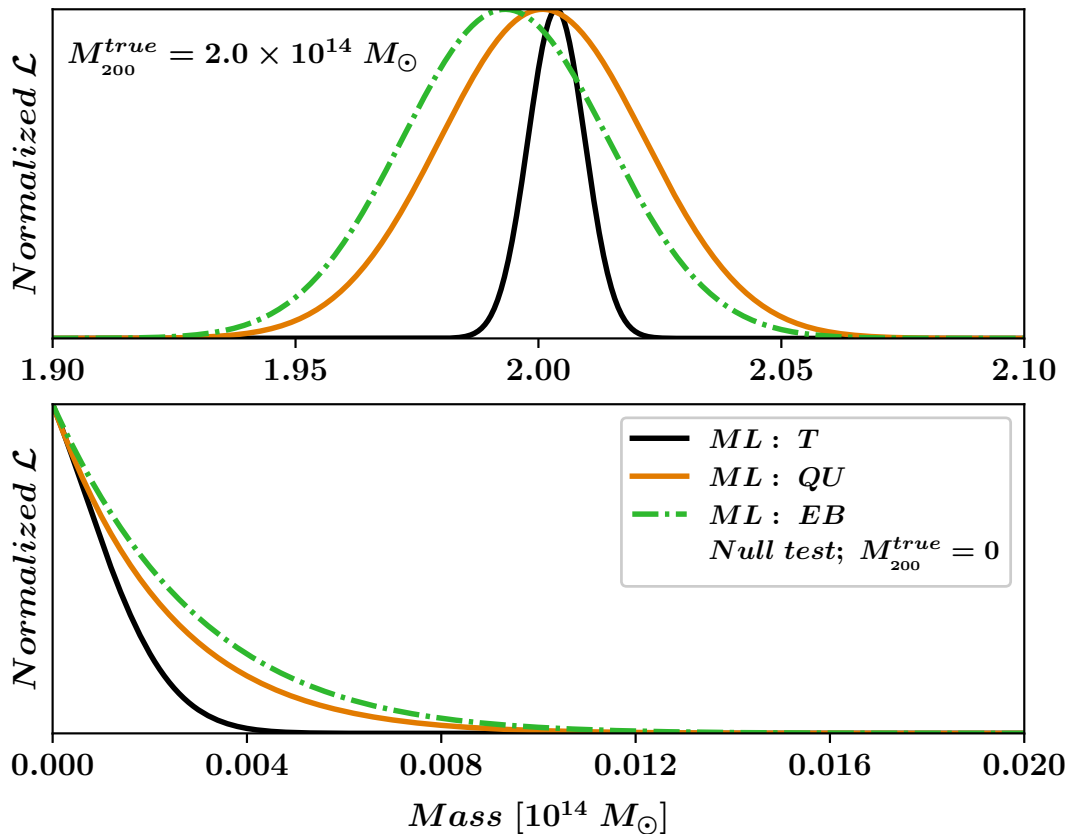


Figure 3.2: In the top panel we show the combined likelihood of 100,000 clusters each at redshift of 0.7 and at mass of $2 \times 10^{14} M_\odot$ for temperature and polarisation MLE estimators. The difference between QU and EB estimator isn't statistically significant. In the bottom panel we show the results of null test and as expected the likelihood peaks at zero for all three estimators

levels. It is evident from the Fig. 3.3 that in the absence of foregrounds, temperature estimator outperforms polarisation above noise-level of $0.075 \mu\text{K}'$. So even for future experiments temperature estimator has to be the primary channel from pure SNR perspective. Only below the noise-level of $0.075 \mu\text{K}'$ do polarisation estimator begin to be competitive with temperature. The relative performance of the temperature and the polarisation estimators can be understood as:

- lensing signal scales the amplitude of the background gradient which is $\sim 10 \times$ brighter in temperature, but
- as the experimental noise levels drop, the background CMB acts as an additional source of noise for the temperature estimator.

Orange squares and green circles in Fig. 3.3 represent MLEs using polarisation QU and EB maps respectively. As expected, there is no significant differences between their performance from a theoretical standpoint. The apparent difference at higher experimental noise levels is not statistically significant. However, using QU maps simplifies the analysis as these modes are directly measured by the experiment and doesn't involve co-ordinate transformation.

Lastly, we compare the performance of temperature MLE (solid black triangles) and QE (orange solid squares) in Fig. 3.3. QE is a first order approximation of MLE (as we will see in 4). At higher noise levels (low SNRs) the effect of higher order terms are negligible resulting in no difference between the performance of MLE and QE estimators. However, at low noise levels (high SNRs) MLE outperforms QE. We find that MLEs performance improves by a factor of 2 at noise level of $0.1\mu\text{K}'$ for our fiducial cluster sample. The performance of QE can be improved by using an iterative version as shown in Yoo and Zaldarriaga (2008).

Both MLE and QE estimators share a common difficulty in regards with the assumed cluster density profile. This dependence shows up in different places in each estimator:

- In MLE as explained in 3.2 we fit the lensed CMB pixel covariance templates to the observed data pixel covariance. The lensed CMB pixel covariance templates are obtained by assuming a cluster density profile.
- QE works by exploiting the correlation between the background CMB gradient and lensing dipole to obtain lensing convergence profile. We fit models to these lensing convergence profile to extract the mass of the cluster.

While MLE outperforms QE at low experimental noise level, QE can be modified to make it robust to the major foreground in lensing analysis as we will see in next chapter (4).

3.3.2 Effects of extragalactic foregrounds on lensing analysis

In this section, we look into the effects of extragalactic foregrounds on CMB-cluster lensing analysis. While galactic foregrounds also affect the CMB-cluster lensing analysis, we can exploit their frequency dependence to suppress galactic

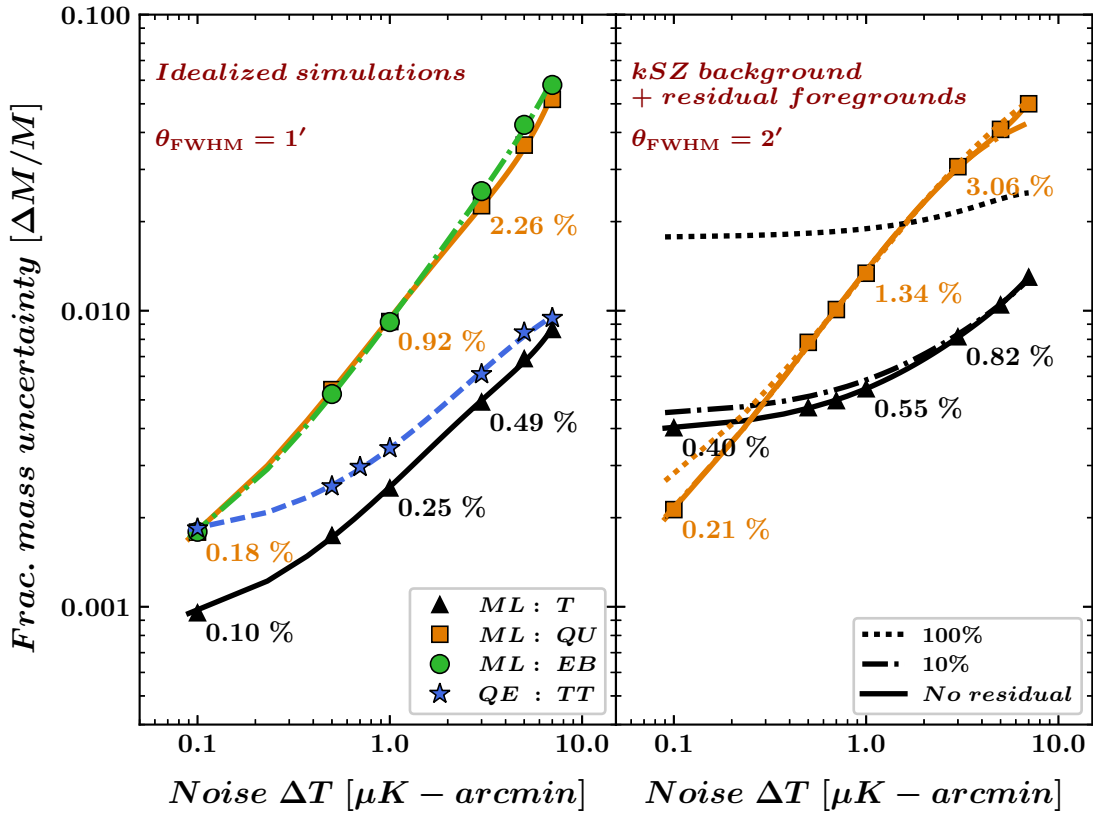


Figure 3.3: In the left we show the performance of different estimators for idealised simulations as function of experimental noise levels. We consider the effects of various foregrounds on the estimators in the right panel. All the curves are for a set of 100,000 clusters each at mass of $2 \times 10^{14} M_\odot$ and at redshift of 0.7.

contamination. Here we consider the effect of extra galactic foregrounds on mass uncertainties. Some of these foregrounds such as clusters own SZ effect etc., also bias the analysis which will be reported in the next section (3.4). The level of foregrounds is much higher in temperature than in polarisation channel, thus the effect of foregrounds is higher in temperature estimator than polarisation. We consider the impact of tSZ, kSZ, radio galaxies and dusty galaxies on lensing analysis.

The impact of foregrounds on the fractional mass uncertainty of lensing estimators as function of experimental noise level is shown in Fig. 3.3. As expected foregrounds have negligible effects on the polarisation channel (orange squares) due to their low level of polarisation. For the temperature estimator the extra-galactic foregrounds set an effective noise level of $5\mu K'$ if not cleaned, this results

in plateauing at 1.8% in mass uncertainty (black dotted line). Without any foreground cleaning polarisation QU estimator outperforms the temperature channel at $1.5 \mu\text{K}'$ noise level. However, we can exploit the frequency dependence of various extragalactic foregrounds to reduce their effect. While combining multiple frequency channels we assume that the beam size is $1'$ FWHM Gaussian irrespective of the frequency channel to simplify the analysis³. Using different spectral dependence of background CMB and tSZ we can completely eliminate the tSZ power. While tSZ can be eliminated, kSZ has the same spectral dependence as that of the CMB and cannot be eliminated using linear combination of different frequency channels.

Furthermore we assume that the frequency cleaning will behind some radio and dusty galaxy power⁴. The black solid line in Fig. 3.3 correspond to 100% removal of radio and dusty galaxy power. The dot-dashed (dashed) line corresponds to 90% (0%) removal of radio and dusty galaxy power. With 90% cleaning of foreground (dashed black curve), temperature estimator becomes the main channel for estimating lensing signal even for future surveys (CMB-S4 Collaboration et al., 2016). There is only a fractional improvement in the performance above 90% of cleaning. It is important to note here that foreground cleaning enlarges the beam which if taken into account will further degrade the mass uncertainties.

To summarize, the extragalactic foregrounds have almost no effect on the performance of polarisation estimators. On the other hand, temperature estimators will have effective noise floor of $5\mu\text{K}'$ if the foregrounds aren't taken into account.

3.4 Systematic bias checks

From Fig 3.3, it is evident that we will achieve unprecedented statistical uncertainties for future low noise surveys. However, in order to fully utilise this statistical power, we need to account for all the systematic biases involved in lensing analysis. In this section, we quantify various sources of systematics that could bias our final results. We examine the following sources:

- cluster center - for example, typical offset between SZ and X-ray centroid is $0.5'$ (von der Linden et al., 2014)
- cluster density profile - the assumed NFW profile may not match the true

³this may not be a very good assumption, but here we just want to build an intuition for future surveys.

⁴note that in all the curves we have assumed 100% kSZ power and 0% tSZ power

density profile

- lensing by other halos - in addition to the galaxy cluster CMB is also lensed by other halos along the line of sight
- redshift - misestimation of cluster redshift
- cluster's tSZ effect
- cluster's kSZ effect
- dusty galaxies

The last three sources have negligible effect on the polarisation estimators as they are partially polarised. Note that all these sources may effect polarisation and temperature estimators to different extents as the angular scales are weighed differently in both estimators.

The baseline simulations for bias calculations include 1' FWHM Gaussian beam, experimental noise level of $1\mu\text{K}'$ in temperature (which corresponds to a noise level of $\sqrt{2}\mu\text{K}'$ in polarisation) and no foregrounds unless otherwise stated. While the precise amount of bias depends on experimental beam size, noise-level, and foregrounds as they define the weighing of different angular scales of MLE, here we roughly quantify the magnitude of bias and give a direction to pursue future work in CMB-cluster lensing to reduce the systematic uncertainties. We report the systematic bias for a sample of 1,000,000 clusters each at a mass of $2 \times 10^{14} M_\odot$ and at redshift of 0.7 (except for redshift uncertainty case). The bias is calculated as follows:

$$b = \frac{M_{bias}}{M_{true}} - 1. \quad (3.17)$$

where M_{bias} is the final recovered mass when the bias source is included in the lensing analysis and M_{true} is the input mass. Error on the bias is obtained by calculating the scatter in 100 subsamples.

We report bias for all the sources considered in Table 3.1. Other than errors in redshift, all other sources of bias should be considered carefully to achieve sub-percent uncertainty as claimed for future CMB surveys (CMB-S4 Collaboration et al., 2016).

Bias source	Bias % at $\Delta T = 1.0 \mu\text{K} - \text{arcmin}$			
	Temperature T_{ML}		Polarization QU_{ML}	
	% bias	error	% bias	error
tSZ cleaning (1% residual signal)	-6.3	0.50	0	-
kSZ fitting (20% uncertainty)	-7.3	0.31	0	-
DG in the cluster	-4.5	1.70	-1.3	1.20
Redshift uncertainty	0.2	0.25	-0.3	0.90
Cluster positions	-7.5		-1.5	
Presence of undetectable haloes	2.5	0.25	6.3	0.92
Uncertainties in cluster mass profile				
$\kappa_{\text{NFW}} + \kappa_{\text{sub}}$	3.1	0.25	-0.6	0.92
κ_{Einasto}	-2.4		-2.5	
$\kappa_{\text{NFW}}^{\text{mod}}$	2.2		0.6	

Table 3.1: The percentage mass biases from various systematic uncertainties. A positive (negative) number means the recovered mass is over- (under-)estimated. The first three lines reflect the expected biases from astrophysical foregrounds; these are serious for the temperature estimator, but not the polarization estimator. The next two lines deal with uncertainties in where the cluster is located (whether in redshift or on the sky); these are likely to be manageable for both estimators. The last four lines relate to uncertainties in how the mass is distributed, whether due to projection effects from nearby, lower-mass haloes, or due to uncertainties in the average mass profile for galaxy clusters. These questions about the mass distribution are a concern for both temperature and polarization.

3.4.1 Halos along the line of sight

In addition to galaxy cluster, the lensing signal also depends on other halos present along the line of sight as well as the correlated halos. If the effect due to these halos isn't taken into account then the final results will be biased high. This is particularly a major concern for low mass haloes as they won't be detected by the survey. To quantify the effect of this bias we use Flender et al. (2016) simulations. The Flender et al. (2016) simulation is an N-body cosmological simulation with 17 million objects. For each cluster we randomly select a halo within a mass range of $M_{200} \in [1.8, 2.2] 10^{14} M_\odot$ and redshift range of [0.6, 0.8]. We simulate the CMB maps as explained earlier, however, instead of lensing the CMB with just the cluster convergence profile we lens it with all the convergence profiles which are within the 50' from the cluster center. Analysis proceeds normally after this - these lensed CMB maps are convolved by Gaussian beam after which

specified white experimental noise is added. As expected both polarisation and temperature estimators are biased high : $2.5 \pm 0.3\%$ for temperature MLE and $6.3 \pm 1.1\%$ for polarisation QU estimator. We can reduce the bias by taking two halo term into account, however, that will include more nuisance parameters increasing the statistical uncertainty of the final results.

Along with the correlated halos and halos along the line of sight, large scale filaments also bias the lensing analysis which is not considered here. Galaxy clusters are not isolated objects, they are generally found in large scale filaments. Also, clusters with ellipticity along the line of sight have higher tSZ increasing the probability of their detection in tSZ surveys. The scope of finding the bias due to the large filaments and selection function is outside the scope of this thesis. Its worth noting that in order to fully realise the potential of future surveys in obtaining sub-percent mass uncertainties, we need to work bias due to large scale filaments and cluster ellipticity. Accurate and reliable simulations of structure formation on large volumes are needed in order to handle this source of systematic error at the sub-percent level.

3.4.2 Cluster mass profiles

As mentioned the lensing estimators assume a density profile which will certainly differ from the true cluster profile. Any difference between the assumed mass profile and true cluster profile will bias the final results. In this work we assume the clusters to follow an NFW profile. However, studies have shown that for massive clusters the density profile deviates significantly from NFW at radius $r \geq 0.5 \times R_{200}$ (Diemer and Kravtsov, 2014). It is unknown whether these deviations will be larger or smaller for lower mass clusters. Also a recent study has shown that for analysis involving stacked halos Einasto profile (Einasto and Haud, 1989) provides a better estimate (Child et al., 2018). Here we consider three density profiles in order to estimate the bias.

- A modified version of the NFW profile which drops off more rapidly with radius

$$\kappa_{\text{NFW}}^{\text{mod}}(x) = \begin{cases} \kappa_{\text{NFW}} & ; x \leq 0.75\theta_{200} \\ \kappa_{\text{NFW}} \times m(i, j) & ; 0.75\theta_{200} < x \leq 1.5\theta_{200} \\ 0 & ; \text{otherwise} \end{cases} \quad (3.18)$$

where $m(i,j)$ is a Hanning two-dimensional (2D) apodization kernel. We create the 2D apodization kernel as $m(i,j) = m(i) \times m(j)$ with $m(i) = \frac{1}{2} \left[1 - \cos \left(\frac{2\pi(i-n/2)}{n} \right) \right]$, where i and j are pixel indices in the $n \times n$ map.

- A change to the cuspiness of cluster core in the NFW profile following King and Schneider (2001)

$$\kappa_{\text{NFW}}^{\text{sub}}(x) = \begin{cases} \kappa_{\text{NFW}} + \sum_{i=1}^3 \kappa_{\text{sub}}^i & ; x \leq 1' \\ \kappa_{\text{NFW}} & ; \text{otherwise}; \end{cases} \quad (3.19)$$

- The Einasto profile (Einasto and Haud, 1989)

$$\rho(r)_{\text{Ein}} = \rho_0 \exp \left(-\frac{2}{\alpha} \left[\left(\frac{r}{R_s} \right)^\alpha - 1 \right] \right) \quad (3.20)$$

with the shape parameter $\alpha = 0.18$ (Ludlow et al., 2013). The Einasto convergence profile is obtained by inserting this into Eq.(3.5).

In each of the three cases we lens CMB by the assumed cluster profile, however, we use NFW profile to calculate our model. Assuming the wrong cluster profile biases the results from -2.5% to 3.8% as shown in Table 3.1. A similar study was done on optical weak-lensing analysis by Sereno et al. (2016) who used NFW profile in the model and Einasto profile in the simulated data; Sereno et al. (2016) found a bias of -2 to 7 % depending on the cluster mass. This level of bias is larger than the statistical mass uncertainties expected for the proposed future experiment (CMB-S4 Collaboration et al., 2016), and a significant challenge for upcoming experiments. More work will be required to accurately measure the cluster mass profiles as a function of radius if we are to achieve the full potential of galaxy cluster cosmology.

3.4.3 Cluster miscentering

Any difference between the true cluster center and the model will result in a bias. Misestimation of the cluster center even by a small amount results in underestimation of cluster mass as we lose some of the lensing signal. To quantify the effect of miscentering, we draw an offset from a normal distribution $N(0, \sigma^2)$ and lens the CMB with offset clusters to obtain simulated data, however, model doesn't take the offset into account. Fig. 3.4 shows the bias in the final results

as a function of offset for both temperature (orange squares) and polarisation estimators (black triangles). As expected the bias increases with the rms offset, ‘ σ ’. The bias in temperature estimator is smaller than polarisation is because the temperature estimator draws more information from smaller angular scales than the polarisation estimator. Note that here we haven’t considered foregrounds, considering foregrounds would decrease the weight of smaller angular scales. For survey with higher experimental noise, larger beams and foregrounds the bias due to miscentering will be smaller.

The typical offset between the SZ-centroid and the X-ray or brightest central galaxy (BCG) is of the order of $0.5'$ (von der Linden et al., 2014; Song et al., 2012; Sereno et al., 2016). For $0.5'$ offset the mass is underestimated by $7.5 \pm 0.3\%$ for temperature estimator and $1.5 \pm 1.3\%$ for polarisation estimator. For a given constraint on the offset, a correction could be easily applied to eliminate the bias, however, that will result in a slight decrease of SNR. Neglecting the foreground power, one would need to know the rms offset σ by 2% (8%) in order to achieve sub-percent uncertainty for the temperature (polarisation) MLE. However, adding foregrounds will reduce the weight of the information from smaller angular scales and lessen the requirement of how well the positional uncertainty must be known.

3.4.4 Bias due to redshift uncertainty

Upcoming surveys such as (Benson et al., 2014; The Simons Observatory Collaboration et al., 2019; CMB-S4 Collaboration et al., 2016) are expected to return tens to hundreds of thousands of clusters. At these numbers obtaining spectroscopic redshift for each cluster will be infeasible. Instead we likely rely on red sequence redshifts up to a redshift ~ 1.5 and lower limits on the redshift for clusters at even higher redshifts. The current state of the art for red sequence redshifts can be seen in the DES `redMaPPer` catalog, where the *photo-z* errors are $\sigma_z = 0.01(1+z)$ for $z \leq 0.7$ and $\sigma_z = 0.02(1+z)$ for $z \sim 0.9$ (Rykoff et al., 2016). We examined the effect of the expected redshift uncertainty by considering a redshift scatter for individual clusters. We conservatively take the redshift errors to be

$$\sigma_z = \begin{cases} 0.02(1+z); & z < 1 \\ 0.06(1+z); & z > 1 \end{cases}$$

We create mock lensed CMB maps for four sets of redshifts redshifts $z \in$

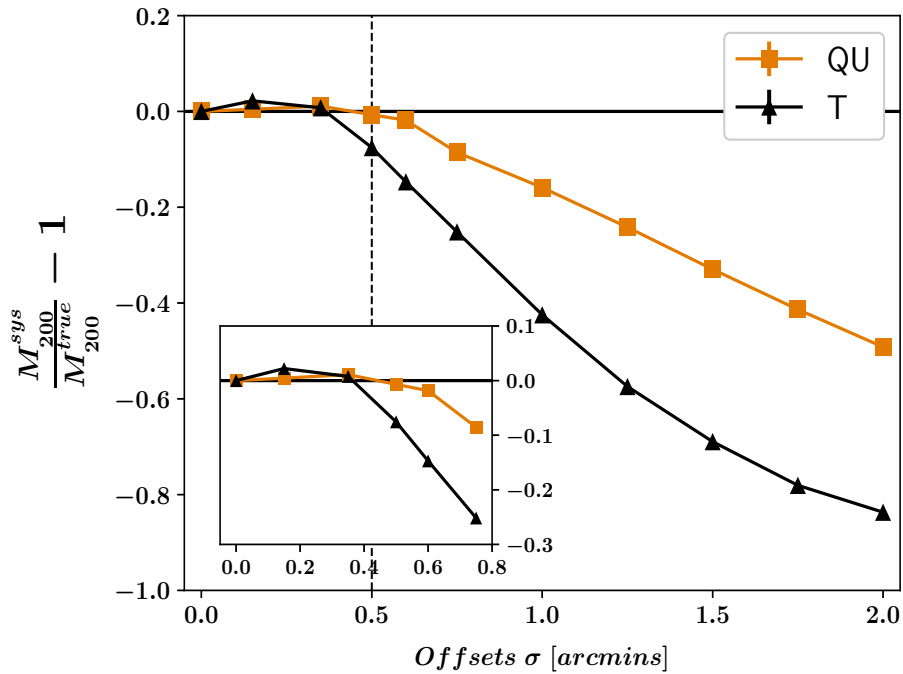


Figure 3.4: The positional offset between the assumed and true cluster centroid will bias the estimate low for T_{ML} (black triangles) and QU_{ML} (orange squares) estimators. The typical positional offset of $0.5'$ (von der Linden et al., 2014; Song et al., 2012; Sereno et al., 2016) is marked with the vertical dashed line. The error bars are derived using estimates gathered by repeating the test 100 times.

[0.5, 1, 1.5, 2]. While constructing the pixel-pixel covariance matrix we use the ‘measured’ redshift, $z+\sigma_z$, for each cluster. The resulting bias is listed in Table 3.1. We do not detect a mass bias at any redshift.

3.4.5 Bias due to the kinematic SZ signal

CMB photons get doppler shifted due to the relative motion of the galaxy cluster with respect to the CMB rest frame, this is known as kinematic Sunyaev-Zel’dovich effect (kSZ) (Sunyaev and Zel’dovich, 1972). While the kSZ effect is an order magnitude smaller than the tSZ, unlike tSZ effect, the kSZ effect has the same spectral dependence as that of CMB. We cannot combine multiple frequency channels to eliminate the kSZ effect. However, we can use polarisation information as the kSZ effect is largely unpolarised (Sazonov and Sunyaev, 1999).

To quantify the kSZ bias on the temperature estimators we consider the publicly available kSZ maps and halo catalog from Flender et al. (2016) simulations.

These are full sky simulations in the healpix (Górski et al., 2005) pixelisation scheme with nside of 8192 corresponding to 0.42 arcminute resolution. Within the mass range of $M_{200} \in [1.8 \times 10^{14}, 2.2 \times 10^{14}] M_\odot$ and $z \in [0.6, 0.8]$ the catalog has 20,000 halos. For each cluster in the simulated data we randomly pick clusters from this set of 20,000 halos. For each cluster we take a $50' \times 50'$ cutout centered around the halo, smooth it with experimental Gaussian beam of $\text{FWHM} = 1'$ and add it to the lensed cluster cutout.

Final results are significantly biased low at 41% level if the kSZ effect is not taken into account while modeling the pixel-pixel covariance matrix. We get similarly large levels of bias when we use an analytical model for the cluster kSZ signal instead of extracting them from N-body simulations. Modelling the optical depth of the clusters using the Battaglia (2016) profile and drawing the cluster velocities from a normal distribution $N(0, \sigma^2)$ with scatter $\sigma = 350 \text{ km/s}$, we obtained a 32% bias in the recovered lensing mass.

If we take the effect of kSZ while modeling the pixel-pixel covariance matrix then as expected we eliminate the bias. However, we don't exactly know the kSZ effect of a single cluster. According to current estimates the uncertainty in kSZ prediction is 20% for a single galaxy cluster. The reason for the uncertainty is the complex cluster baryonic physics which is not very well understood. To determine the bias that would result due to the uncertainty in kSZ effect, we test including 20% uncertainty in the kSZ modeling for the pixel-pixel covariance matrix. This results in a low bias of $7.5 \pm 0.4 \%$, the stated bias can either be low or high depending on underestimation or overestimation of kSZ. Interpolating linearly between the kSZ uncertainty and the bias, we find that 2-3% uncertainty in kSZ would lead to sub-percent systematic uncertainty. Given the current uncertainties in kSZ estimation, it acts as a serious obstacle in using temperature information of CMB-cluster lensing for future CMB surveys.

3.4.6 Thermal Sunayev-Zel'dovich effect

Here we give a brief review of thermal Sunayev-Zel'dovich (tSZ) effect and is explained in detail in the next chapter. CMB photons while passing through galaxy cluster are inverse compton scattered of high energetic electrons present in the cluster's hot intra cluster medium. This results in excess of photons at higher frequency and deficit of photons at lower frequency, this is known as tSZ effect. tSZ effect is an order of magnitude greater than lensing signal and will induce

significant statistical and systematic uncertainties if not taken into account. In the next two chapters we discuss in detail about the methods through which we eliminate the tSZ bias in QE estimator. Here, we quantify the tSZ bias in the MLE and discuss the methods that can be used to reduce the bias. We consider two different approaches:

- use frequency channels to eliminate the tSZ
- model the tSZ effect in the pixel-pixel covariance matrix

Either approaches has the potential to completely eliminate the bias, however, due to imperfect knowledge of the instrument calibration or the tSZ profile may leave residual bias.

To evaluate the performance of each approach, we use Compton y maps produced on a $5^\circ \times 5^\circ$ box at resolution $2.5'$ from the smoothed-particle hydrodynamics (SPH) simulations of McCarthy et al. (2014). Neglecting relativistic corrections, we convert the Compton y maps into temperature at an observing frequency according to:

$$\Delta T = y T_{\text{CMB}} \left[x \left(\frac{e^{x/2} + e^{-x/2}}{e^{x/2} - e^{-x/2}} \right) \right] \quad (3.21)$$

where $x = \frac{h\nu}{k_B T_{\text{CMB}}}$, ν is the frequency in GHz, $T_{\text{CMB}} = 2.73$ K, k is the Boltzmann constant, and h is the Planck constant.

tSZ frequency cleaning

Using the spectral dependence of tSZ we can eliminate it by using CMB maps observed at different frequency channels. In this chapter we assume the CMB is observed at 90 GHz and 150 GHz channels with Gaussian beam of FWHM $1.7'$ and $1'$ respectively. Using a linear combination 90 and 150 GHz channels, we obtain tSZ free map as follows:

$$\tilde{T}(\hat{\mathbf{n}}) = \frac{f \tilde{T}_{150}(\hat{\mathbf{n}}) - T_{90}(\hat{\mathbf{n}})}{f - 1} \quad (3.22)$$

where

$$\tilde{T}_{150}(\hat{\mathbf{n}}) = T(\hat{\mathbf{n}})_{150} * \frac{B_{90}(\hat{\mathbf{n}})}{B_{150}(\hat{\mathbf{n}})} \quad (3.23)$$

is the 150 GHz map convolved by the ratio of the 90 and 150 GHz beam functions. The factor ‘ f ’ is ratio of tSZ amplitude in 90 and 150 GHz.

We also assume that the experimental noise level in both 90 and 150 GHz channels is $1 \mu\text{K}'$. Under these assumptions using a tSZ free map will eliminate the bias ($b = 0.0 \pm 0.7\%$). However, it degrades the final SNR by a factor of three as shown in Baxter et al. (2015). In practice, it is unlikely to obtain a precise value of factor ‘f’ due the uncertainties in frequency band widths or errors in relative calibration of frequency bands. To evaluate the bias in the final results due to the uncertainties in the factor ‘f’, we use simulations. We assume an uncertainty of 1% in f, which is overly conservative for future CMB surveys but comparable to that of current surveys. An error in f will result in leakage of tSZ in the final tSZ free maps and will bias the results. For 1% uncertainty in ‘f’ we find the final results to be biased low by -6.3 ± 0.7 percent. The bias can shift depending on whether the SZ leakage is over estimated or under estimated.

tSZ has no power at 217 GHz and one might consider of using 217 GHz frequency channel instead of creating tSZ free maps. However, the power of dusty galaxies increase significantly with frequency. So, the foreground power in 217 GHz channel is much more than 90 or 150 GHz channels. In addition to that, we should also take into account the contamination due to the correlation between the tSZ and cosmic infrared background due to these dusty galaxies. Current estimates find the correlation co-efficient to be $0.113^{+0.057}_{-0.054}$ (George et al., 2015); estimating the tSZ-CIB signal at 220 GHz would yeild a signal nearly three quarters of the tSZ signal at 150 GHz. In order to use 217 GHz channel, more work needs to be done in constraining the tSZ-CIB correlation.

tSZ fitting

Another way to tackle tSZ signal is by modeling it in pixel-pixel covariance matrix. We calculate the expected tSZ contribution using SPH simulations from McCarthy et al. (2014). As one expects, with perfect knowledge of tSZ we get a bias consistent with zero ($b = 1.0 \pm 0.6\%$). However, similar to tSZ frequency cleaning the bias increases quickly if the tSZ contribution is mis-estimated. Misestimating the tSZ signal by 1% leads to significant (order 6%) shifting the recovered mass. Given that the current uncertainties in modeling the tSZ signal from galaxy clusters are at least an order of magnitude larger, it will be extremely challenging to achieve the sub-percent precision necessary to make this approach viable.

3.4.7 Dusty galaxies in the cluster and other foregrounds

Galaxy clusters are known to host overdensities of dusty galaxies, with several papers measuring the resulting tSZ-CIB correlation (Dunkley et al., 2013; George et al., 2015; Planck Collaboration et al., 2016c). We describe our modeling of these DG overdensities⁵ in the Appendix A.2.3. If ignored, the tSZ-CIB correlation may substantially bias the recovered masses from temperature estimators, especially at higher frequencies. The emission from dusty galaxies rises sharply with frequency, by an order of magnitude in μK_{CMB}^2 from 90 to 150 GHz and again from 150 to 220 GHz. Polarization estimators (at least at 150 GHz and lower frequencies) are essentially unaffected due to the lower polarization fraction of dusty galaxies (expected to be less than 4% (Manzotti et al., 2017; Seiffert et al., 2007)). The tSZ-CIB correlated power could be handled analogously to either the tSZ fitting or cleaning approaches in §3.4.6. However, a multi-frequency cleaning scheme will be less effective than for the tSZ effect since the spectral dependence of thermal dust emission varies between individual galaxies. Here we look only at bias for the fitting approach where the pixel-pixel covariance due to the clustered dusty galaxies is folded into the likelihood. The recovered mass is somewhat low: $b = 4.5 \pm 1.7\%$. The existence of a bias (higher than 2σ) is slightly surprising since one would expect zero bias in the perfect information limit, and the significance is low enough that it may be a statistical fluke. The dramatic increase in the uncertainty – from 0.25% to 1.7% – reflects the plateauing of the dotted line in right panel of Fig. 3.3. Unsubtracted foreground power effectively sets a lower bound on the instrumental noise.

3.5 A look into the future

In this final section we forecast the cluster mass uncertainties from CMB-cluster lensing for the AdvACT , Simons Array, and SPT-3G experiments, which we will collectively refer to as the Stage III experiments, as well as the proposed CMB-S4 experiment. In addition to presenting estimated mass uncertainties for the fiducial versions of these experiments, we examine how the mass uncertainty depends on the beam size and map noise levels. This information can be used to evaluate design tradeoffs while planning future experiments.

⁵For implementation reasons, in this section, we include all foregrounds mentioned in the Appendix A.2, even ones that are not correlated with the cluster itself, such as radio galaxies.

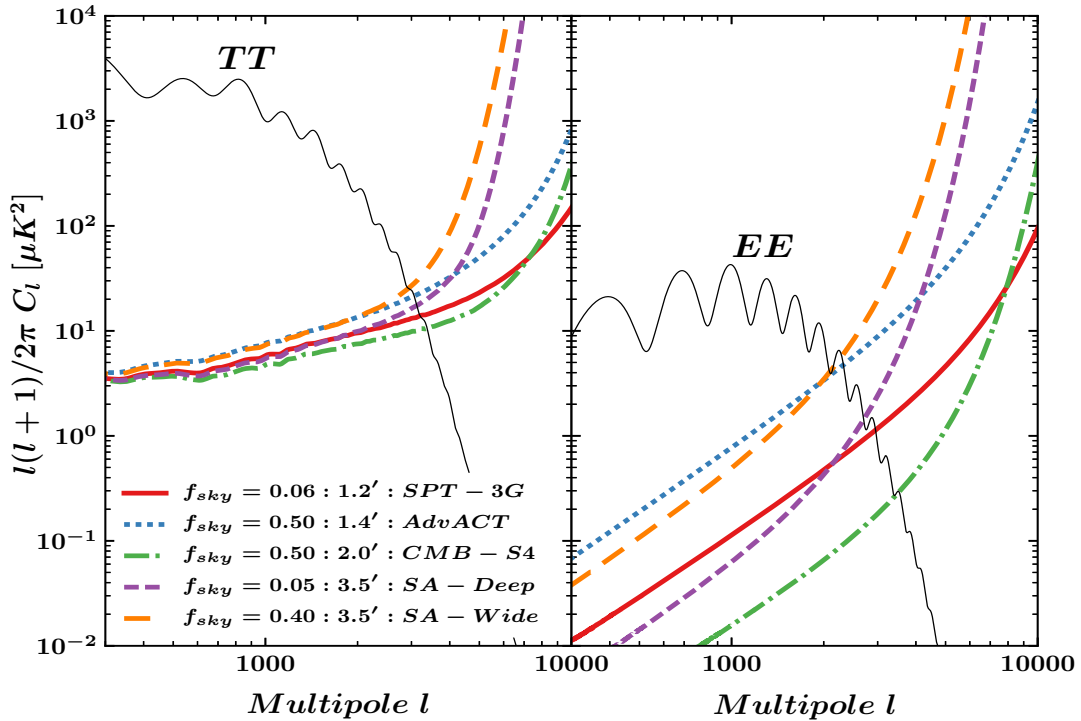


Figure 3.5: The expected residual foreground and noise power spectrum for the future CMB experiments. The 90, 150, and 220 GHz channels have been combined using a constrained ILC technique to remove the tSZ effect while minimizing other extragalactic foregrounds and instrumental power. The left and the right panels correspond to temperature and polarization respectively. The plateauing of the residual temperature spectrum reflects the limited foreground removal possible with three frequency channels. Specifications about each experiment are listed in Table 3.2.

3.5.1 *Expected lensing mass uncertainties for future CMB experiments*

We expect the next generation of CMB experiments, which will have substantially more detectors and a concomitant reduction in map noise levels, to dramatically improve the cluster mass calibration possible from CMB-cluster lensing. The experimental configuration of all the experiments considered is given in Table 3.2. Three options for telescope size (and therefore beam sizes) are listed for the proposed CMB-S4 experiment. While current results have mass uncertainties of order $\geq 20\%$ (Baxter et al., 2015; Madhavacheril et al., 2015; Planck Collaboration et al., 2016a), we will show that stage III experiments to reach 3% and CMB-S4

Experiment	ΔT [$\mu\text{K}\text{-arcmin}$]			f_{sky}	Effective beam [θ_{FWHM}]	# of clusters (N_{clus})	T_{ML} (ILC)	QU_{ML} (ILC)	
	90	150	220						
CMB - S4	1.0	1.0	1.0	0.50	1.0'	100,000	0.87%	0.83%	
					2.0'		0.95%	0.98%	
					3.5'		1.20%	1.60%	
SPT-3G	4.5	2.5	4.5	0.06	1.2'	10,000	3.28%	6.12%	
AdvACT	8.0	7.0	25.0	0.50	1.4'		4.35%	>15%	
Simons Array - Deep	1.5	1.5	4.7	0.05	3.5'		4.41%	8.45%	
Simons Array - Wide	5.5	5.5	20.0	0.40			5.86%	>15%	

Table 3.2: The forecasted mass uncertainties for large-aperture future CMB experiments. We combine data from 90, 150, and 220 GHz to clean the extragalactic foregrounds using a constrained ILC method designed to remove the tSZ signal while minimizing the residual foreground power and instrumental noise. For polarization, the ILC is essentially optimal weighting of the bands for minimum noise.

to approach 1%.

There are two reasons for the improvements. First, with more detectors comes lower map noise levels (and larger survey areas). The deepest current experiments reach approximately $5 \mu\text{K}\text{-arcmin}$ in temperature; the Stage III surveys (AdvACT (Henderson et al., 2016); Simons Array (Suzuki et al., 2016), and SPT-3G (Benson et al., 2014)) forecast a few $\mu\text{K}\text{-arcmin}$; and projections for CMB-S4 are $\sim 1 \mu\text{K}\text{-arcmin}$. Lower noise improves the lensing significance on any individual galaxy cluster. Second, lower noise levels and larger survey areas translate into substantially more galaxy clusters. Current ground-based SZ cluster catalogs have fewer than 1000 clusters (Hasselfield et al., 2013; Bleem et al., 2015), but SPT-3G is forecast to find 8000 clusters (Benson et al., 2014), AdvACT 10,000 clusters (Henderson et al., 2016) and we assume ad-hoc that CMB-S4 will find 100,000 clusters. In addition to the internally discovered clusters, optical surveys like DES (Rykoff et al., 2016), and in the future LSST (LSST Science Collaboration et al., 2009) and Euclid (Refregier et al., 2010), will yield extremely large numbers of galaxy clusters within the CMB survey regions, as will the X-ray satellite eROSITA (Merloni et al., 2012). This method is perfectly suited to determining the mass calibration for these external cluster catalogs as well.

To provide realistic estimates of the mass uncertainties, we perform a constrained internal linear combination (ILC) of data from 90, 150, and 220 GHz

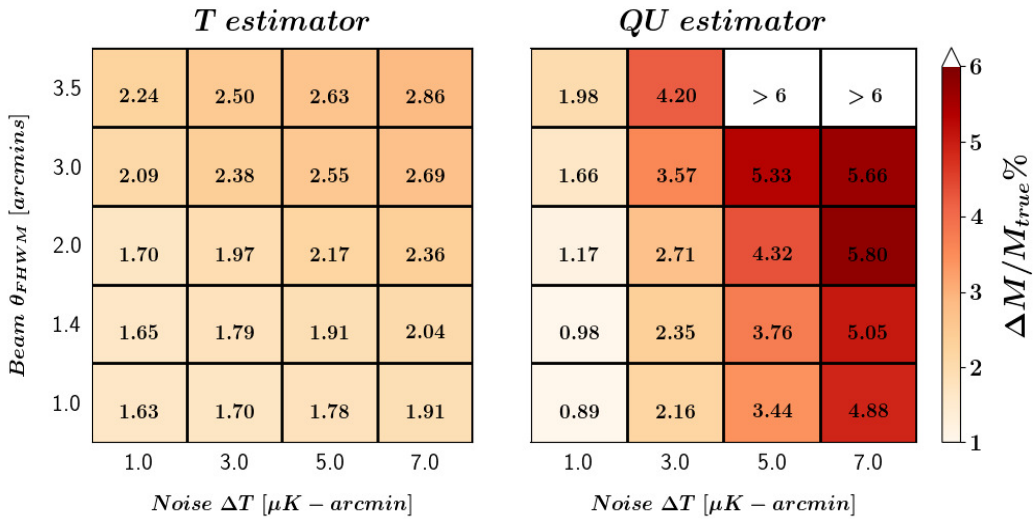


Figure 3.6: The performance of the polarization MLE is very sensitive both to the angular resolution and map noise level of an experiment; the gains for the temperature MLE are much smaller. The numbers correspond to the CMB-cluster lensing mass uncertainty (in percent) of the cluster sample containing 100,000 clusters after the addition of foregrounds (dotted lines in right panel of Fig. 3.3). Improving the beam from $3.5'$ to $1'$ enhances the SNR by a factor of two for the CMB-S4 noise levels. The saturation of T_{ML} is due to the larger impact of foregrounds on the temperature maps.

channels based on the **SMICA** (Spectral Matching Independent Component Analysis) algorithm (Cardoso et al., 2008; Planck Collaboration et al., 2014a) to eliminate the tSZ signal from the temperature data and minimize the residual power in other extragalactic foregrounds and instrumental noise in both temperature and polarization.⁶ The resulting power spectra of the instrumental noise and residual foregrounds for different CMB experiments are shown in Fig. 3.5. At $\ell \leq 2000$, the temperature curves are dominated by residual foreground power as three frequency bands are insufficient to completely eliminate the foreground power in the assumed model (see Appendix). As a result, the temperature noise curves converge at $\ell \leq 2000$ despite the very different noise levels of the experiments. During this process, we convolve the 90 and 220 GHz spectra by the ratio of 150 GHz beam and their native beams, so that the final effective beam size matches 150 GHz.

⁶Note that unlike in Fig 3.3 we consider the effect of relative beam and noise levels of different frequency channels

The expected performance of each experiment is given in Table 3.2. One significant uncertainty is the number of clusters to assume for each experiment. As accurately modeling the survey selections functions for SZ, optical, and X-ray surveys is beyond the scope of this work, we make the simplifying assumption that all Stage III experiments will have 10,000 clusters and the CMB-S4 experiment will have 100,000 clusters. This is of order the number expected to be discovered through the tSZ effect by the SPT-3G (8000 clusters; Benson et al. (2014)) or AdvACT (10,000 clusters; Henderson et al. (2016)), but likely an over-estimate for the Simons Array due to its larger 3.5' beam size. On the other hand, the experimental beam size is irrelevant when predicting the size of cluster samples from optical or X-ray surveys that overlap with the CMB surveys. The DES or LSST surveys should provide samples with more than 50,000 clusters for all of the Stage III CMB experiments (Rykoff et al., 2016; LSST Science Collaboration et al., 2009). Given a specific sample size, the mass uncertainty can be obtained by rescaling the numbers provided in Table 3.2 by $\sqrt{\frac{N_{\text{sample}}}{N_{\text{clus}}}}$.

Even considering concerns about potential biases from astrophysical signals, the temperature channel will be extremely important for the cluster mass estimates from the Stage III CMB experiments. The mass uncertainty on the fiducial 10,000 cluster sample is similar in temperature from all three experiments, with a range from 3.3% (SPT-3G) to 5.9% (the Simons Array wide survey). These uncertainties are as large as the likely systematic uncertainties, and the statistical uncertainties on polarization are higher by a factor of two or more. As an example of scaling the results with sample size, we replace the fiducial sample size by the expected number counts for SZ-discovered clusters with SPT-3G (8000) and optically detected clusters from the DES (50,000). SPT-3G would achieve a 3.6% mass uncertainty with a sample of 8000 SZ-selected clusters and a 1.5% uncertainty on a sample of 50,000 optically-selected clusters. The shallow portions of the Simons Array or AdvACT surveys cannot contribute much for the polarization estimator; lower noise levels are essential. The polarization estimator can be within a factor of two for the deep surveys of the Simons Array or SPT-3G. For instance, the polarization estimator for SPT-3G on 8000 clusters yields a 6.8% mass calibration, to be compared to the 3.6% mass calibration from temperature (ignoring systematic uncertainties).

The lower level of systematic uncertainty for polarization comes into play for the CMB-S4 experiment. First, for the extremely low noise levels of CMB-S4,

the performance of the temperature and polarization channels is nearly identical (0.95% vs. 0.98%) for an instrument with $2'$ beam resolution. Second, the magnitude of the temperature-only systematic errors (primarily from the SZ effect) is now several times larger than the raw statistical uncertainties, and would dominate the temperature error budget. We can expect cluster mass calibrations from CMB-S4's polarization data at the 1% level.

The mass calibration forecasts in Table 3.2 are highly complementary to and competitive with the masses obtained by stacking optical weak lensing measurements. For example, LSST hopes to achieve a mass uncertainty of 1% by stacking few thousands of clusters at redshifts $z < 0.5$ (LSST Science Collaboration et al., 2009). At high redshifts, since the number density of background galaxies decrease rapidly, the constraints from optical lensing measurements tend to weaken. Calibrating the high redshift end of the mass function is the true power of CMB-cluster lensing which will allow us to place important constraints on the redshift evolution of mass-observable scaling relations out to high redshifts $z \geq 1.5$.

3.5.2 Optimizing survey design: SNR as a function of beam size and map noise levels

There are plans underway to build a substantially more sensitive CMB experiment, CMB-S4 (CMB-S4 Collaboration et al., 2016), with work already underway both on design studies and planning for CMB-S4 and on pathfinder experiments to CMB-S4 such as the Simons Observatory. There is a wide spectrum of science drivers for these experiments, of which CMB-cluster lensing is only one. However, it is useful to consider what CMB-S4 design choices would be optimal for cluster mass calibration. In this section, we consider two lever arms: map noise levels and angular resolution (beam size). In all cases, we assume three frequency bands centered at 90, 150 and 220 GHz with equal noise levels and beam sizes that scale as the wavelength. We do not consider the number or relative weight of frequency bands, although these decisions will be important for handling astrophysics foregrounds in the temperature estimator.

In Fig. 3.6, we present the mass uncertainties on a sample of 100,000 clusters from the temperature and polarization estimators for a grid of five different beam sizes $\theta_{\text{FWHM}} = 1', 1.^4, 2', 3', 3.^5$, and four temperature map noise levels (1, 3, 5, or $7 \mu\text{K-arcmin}$). We have simplified the problem by using only 150 GHz data with no foreground removal. As a result, the quoted uncertainties are likely

to be too large for both temperature and polarization estimators. However, the qualitative conclusions are robust to this assumption as will be shown below by spot-checking the results with a full ILC analysis.

Notably, the temperature results show only a minor improvement (< 20%) going from 7 to 1 $\mu\text{K}\text{-arcmin}$ noise levels. The plateauing occurs because the instrumental noise is already smaller than the foreground power. Although the exact level may be off, these 150 GHz only results are consistent with the picture from the full, 3-frequency ILC analysis shown in Fig. 3.5. In that figure, the residual foreground and noise power curves for temperature are essentially the same, whether from CMB-S4, from small and deep Stage III surveys, or from wide and shallow Stage III surveys. In short, foreground residual power dominates the results even at the lower sensitivities of the Stage III experiments. The temperature estimator also shows a fairly modest effect from reducing the beam size: a factor of 3.5 reduction in beam size from 3. $'$ 5 to 1' only improves the mass uncertainty by a factor of 1.35. This is because the foreground power floor limits the use of small-scale modes where the beam size matters most.

In contrast, as seen in the right panel of Fig. 3.6, the fidelity with which the QU polarization estimator recovers cluster masses is strongly dependent on the experimental noise level and beam size. The clear improvements are because polarization estimator is still noise instead of residual foreground dominated. Improving map noise levels from 3 to 1 $\mu\text{K}\text{-arcmin}$ improves the SNR on CMB-cluster lensing by a factor of 2.4 (the equivalent change for the temperature estimator is only 1.04). Similarly, reducing the beam size three fold from 3' to 1' leads to an improvement by a factor of 1.9. Both the beam size and instrumental noise levels matter for the performance of the polarized CMB-cluster lensing estimator.

Finally, we confirm this picture by extending these 150 GHz-only predictions to 3-band data using the ILC method. We assume equal temperature map noise levels of 1 $\mu\text{K}\text{-arcmin}$ at 90, 150 and 220 GHz, with a beam size that scales with the wavelength. We consider three 150 GHz beam sizes, 1', 2', and 3. $'$ 5, with the results tabulated in Table 3.2. The improvement as a function of the beam size is consistent between the 150 GHz and ILC cases. While the improvement is only marginal for the temperature channel, the mass uncertainty from the polarization estimator drops to 0.83% for a 1' beam, a factor of 1.9 better than the results for a 3. $'$ 5 beam. The corresponding improvement for 150 GHz only is slightly better,

at a factor of 2.2.

3.6 Conclusion

We have developed MLEs to optimally extract lensing information from the temperature (T) and polarization (Q/U) maps of the CMB. We show a Q/U based MLE recovers as much information as an estimator using E and B mode maps. We also show that the temperature MLE performs better than the standard QE by a factor of two at very low noise levels in the absence of astrophysical foregrounds; the performance gain is not significant for the polarization estimator due to the lower SNR. We consider the effects of these foregrounds on the cluster lensing estimators, finding at 150 GHz that astrophysical foregrounds have no impact on the polarization MLE and set an effective noise floor of a few $\mu\text{K}\text{-arcmin}$ on the temperature MLE unless removed using multi-frequency data.

We quantify the systematic uncertainties due to astrophysical foregrounds (the tSZ effect, kSZ effect or dusty galaxies), uncertainty in the cluster position or redshift, projection effects from nearby lower-mass haloes, and uncertainty in the cluster mass profile. We find that the dusty galaxies in the cluster are likely to bias the temperature(polarisation) MLE at -4.5%(-1.3%) level. The biases due to uncertainty in the cluster position or redshift are manageable for both temperature and polarization. Lower mass haloes near the galaxy cluster lead to an overestimate of the cluster masses at the 2.5 to 6.3% level, and will need to be carefully accounted for using simulations. The uncertainties in the cluster mass profile can shift the cluster mass either up or down by up to a few percent. Better measurements of the cluster mass profile are needed to reduce this uncertainty.

The clusters own SZ signals induce significant bias on temperature MLE. The kSZ effect has the same spectral dependance as that of CMB and cannot be removed using multiple frequency channels; it will induce a bias of -7.3% on temperature MLE. tSZ induce significant biases on MLE estimators if not taken into account. tSZ is an order of magnitude greater than lensing signal and if not taken into account will kill the lensing signal. We can exploit multiple frequency channels to remove tSZ, however, that will decrease the SNR by a factor of three (Baxter et al., 2015). In the next two chapter we will introduce modified QE to eliminate the tSZ bias with negligible decrease in SNR.

Finally, we present forecasts for the mass uncertainties from upcoming CMB experiments, combining multiple frequency bands with an ILC technique to min-

imize the instrumental noise and astrophysical foregrounds. The AdvACT, Simons Array and SPT-3G experiments will achieve mass calibration uncertainties of order 3 - 6% for a sample containing 10,000 clusters, with the temperature channel being crucial to these mass constraints. With the even lower noise levels of CMB-S4 and a $2'$ beam, we find the statistical mass uncertainty from either the temperature or polarization MLEs falls to just below 1% with 100,000 clusters. We expect polarization to be the main information channel for CMB-S4 given the potential biases due to the temperature foregrounds. Finally, we consider how the performance of CMB-S4 depends on the assumed noise level or beam size, finding that a factor of three reduction in either the beam size or noise level leads to roughly a factor of two improvement on the mass calibration from the polarization MLE. CMB-S4 has the potential to transform galaxy cluster cosmology by reducing the current 20% mass uncertainty on galaxy clusters twentyfold to $\sim 1\%$.

Chapter 4

modified quadratic estimator

Overview

During my thesis, we developed modified quadratic estimator (QE) to eliminate the bias due thermal Sunyaev Zel'dovich (SZ) effect. We give a brief review thermal Sunayev-Zel'dovich effect (refer Sunyaev and Zel'dovich (1970) for a detailed review) and its effect on cluster lensing in the §4.2.1. Then we discuss the modifications of the QE to remove SZ bias in §4.2. We explain the data sets used for the project in §4.3, model fitting in §4.4, verification of our new method using simulations in §4.5, and quantify systematics in §4.5.2. Finally we conclude in with results in §4.6.

4.1 Thermal Sunayev-Zel'dovich effect

Cosmic microwave background (CMB) photons get inverse Thompson scattered off the high energy electrons present in the intra cluster medium of a galaxy cluster, resulting in a deficiency of photons at lower frequencies and excess of photons at higher frequencies. This phenomena is called thermal Sunayev-Zel'dovich effect (SZ). SZ is a small effect and to illustrate it we have shown CMB spectral distortion for a fictional galaxy cluster of mass 1000 times more than of a typical galaxy cluster in Fig. 4.1. The solid black curve represents the intensity of CMB as a function of frequency before its interaction with hot intracluster medium; solid blue represents the same after its interaction. As shown in the Fig. 4.1, due to SZ effect CMB intensity decreases below a frequency of 220 GHz and increases at higher frequencies.

The fractional change in temperature is given by

$$\frac{\Delta T_{SZ}}{T_{CMB}} = f(x)y = f(x) \int n_e \frac{k_B T_e}{m_e c^2} \sigma_T dl \quad (4.1)$$

where y is Compton y -parameter, n_e is the electron number density, m_e is the

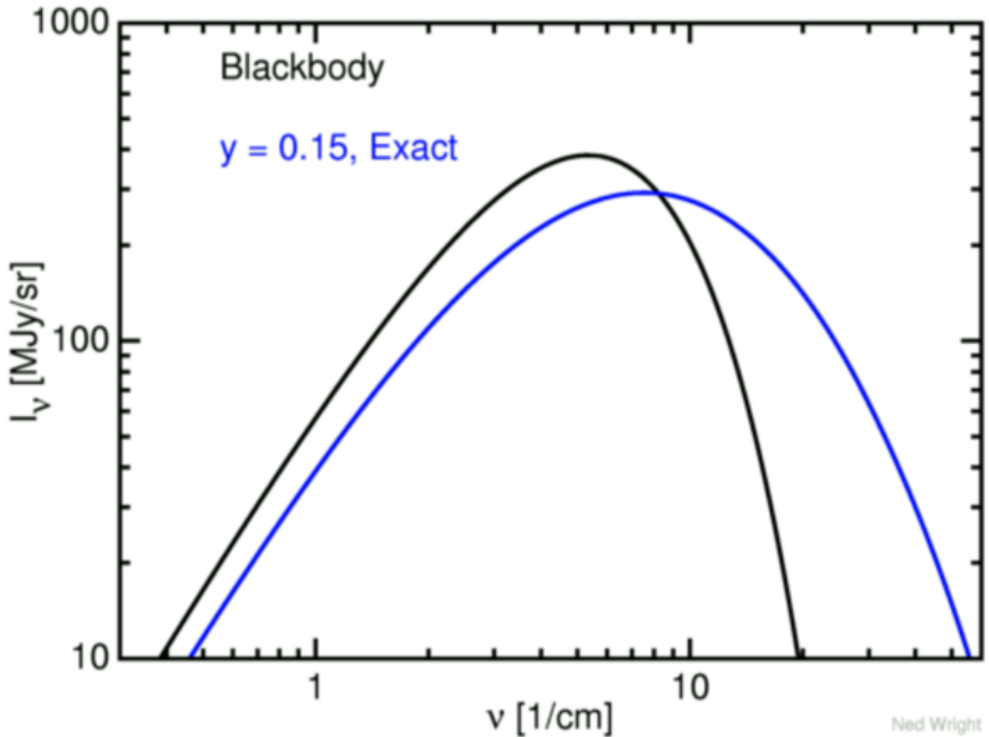


Figure 4.1: The plot shows the intensity of CMB as function of frequency before (black) and after (blue) it passes through a cluster.

electron rest mass, c is the speed of light, T_e is the electron temperature, σ_T is the Thompson cross-section, and $f(x)$ is the dimensionless frequency given by

$$f(x) = \left(x \frac{e^x + 1}{e^x - 1} - 4 \right) (1 + \delta_{SZE}(x, T_e)) \quad (4.2)$$

where $\delta_{SZE}(x, T_e)$ is the relativistic correction to the frequency dependence.

As can be inferred from Eq. 4.1 SZ effect is independent of redshift and has potential to detect high redshift clusters, where the cluster abundance critically depends on underlying cosmological model. CMB surveys use SZ effect to detect galaxy clusters, clusters appears as blue blob at frequencies lesser than 220 GHz. Fig. 4.2 shows a galaxy cluster of mass $M_{200m}^1 = 5 * 10^{14} M_\odot$ as seen by CMB survey in 90 GHz and 150 GHz channels . Effect of SZ signal on CMB lensing is discussed in 4.2.1.

¹ M_{200m} is defined as the mass of the cluster within a radius R_{200} , within which the cluster density is 200 times the critical density of the Universe at cluster redshift

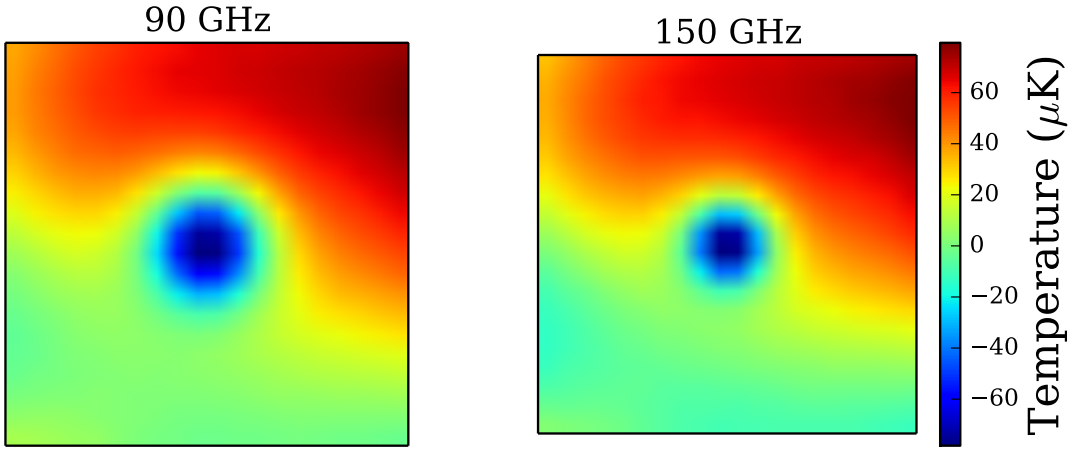


Figure 4.2: A galaxy cluster of mass $M_{200m} = 5 * 10^{14} M_\odot$ as seen in a CMB survey with following specifications : 1.'7 beam at 90 GHz (left panel) and 1'beam at 150 GHz (right panel).

4.2 QUADRATIC ESTIMATOR

As mentioned in the previous chapter, lensing remaps the unlensed CMB field. To a first order approximation it can be written as

$$T(\hat{n}) \approx \tilde{T} + \nabla T \cdot \vec{\alpha}(\hat{n}) \quad (4.3)$$

$$T(\hat{n}) - \tilde{T} \approx \nabla T \cdot \vec{\alpha}(\hat{n}) \quad (4.4)$$

where \tilde{T} represents the unlensed temperature field, \hat{n} is the direction vector, $\vec{\alpha}$ is the deflection angle which depends on the cluster mass. While this is just a first order approximation it holds particularly well for CMB lensing. This can be understood as follows:

- typical size of galaxy cluster is of the order of few arc minutes ($z > 0.3$)
- primordial CMB doesn't have power at such small scales due to diffusion damping Silk (1968) and can be approximated as a gradient.

For a given cluster mass and redshift, the magnitude of this dipole scales linearly with the magnitude of the CMB gradient. This correlation between the unlensed CMB gradient and lensing signal is exploited by the quadratic estimator to estimate cluster mass. Below we provide a brief mathematical formalism for temperature quadratic estimator and it generalises for polarisation. One is encouraged to refer Hu et al. (2007) for a detailed review.

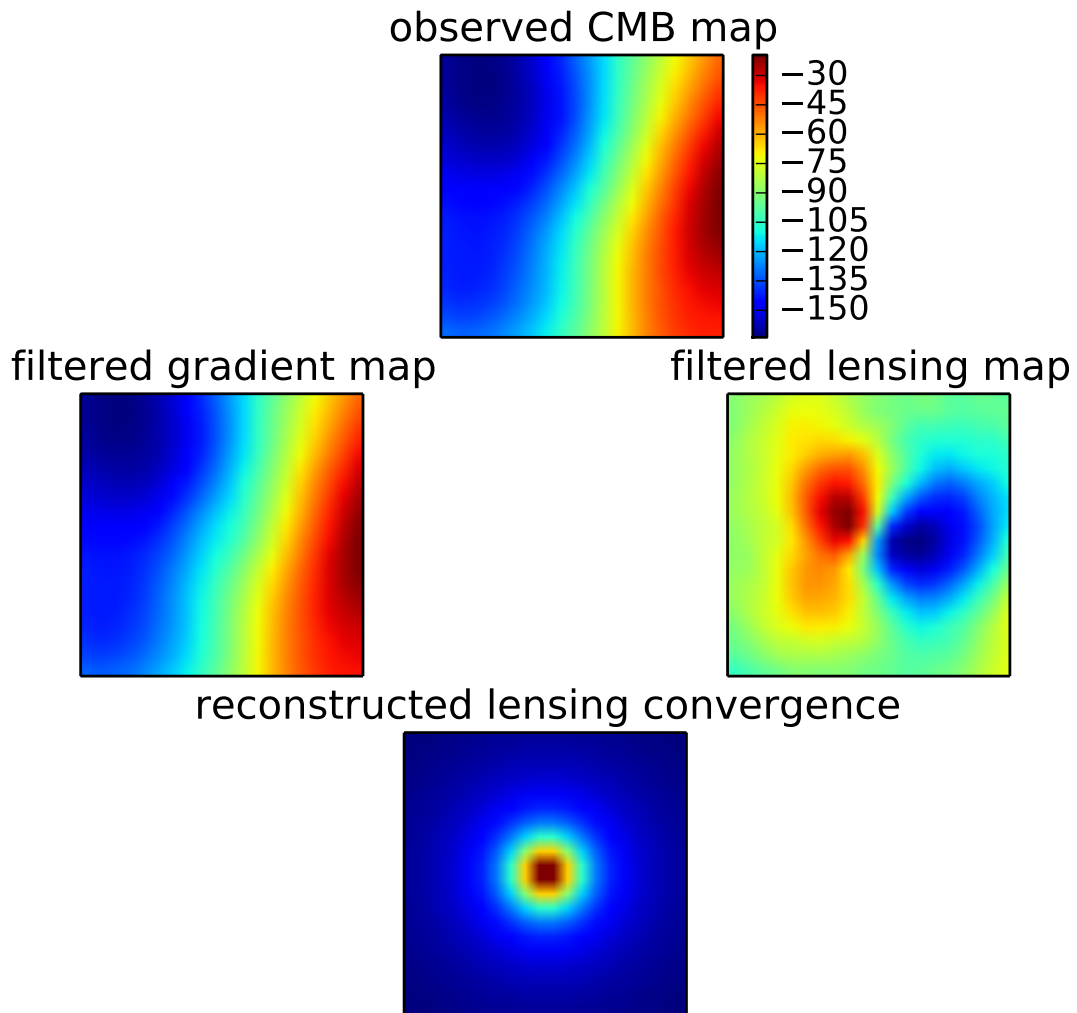


Figure 4.3: Schematic representation of quadratic estimator. Top panel shows the observed CMB temperature map which acts as the input. The observed map is passed through the filters to obtain large scale gradient map (left middle panel) and small scale lensing map (right middle panel). QE extracts the correlation between panel gradient map and lensing map to obtain reconstructed lensing convergence profile shown in panel the bottom panel

Under the gradient approximation, we construct an estimator of lensing convergence by multiplying the lensing map and the gradient map. The gradient approximation doesn't hold for all Fourier modes, only for the modes which are correlated by reconstruction. We filter maps in the Fourier space to isolate modes for which the gradient approximation is valid.

We obtain gradient and lensing maps as follows,

$$L(\hat{n}) = \int \frac{d^2l}{(2\pi)^2} e^{il.\hat{n}} W_l^T T_l \quad (4.5)$$

$$G(\hat{n}) = \nabla \left(\int \frac{d^2l}{(2\pi)^2} e^{il.\hat{n}} W_l^{TT} T_l \right) \quad (4.6)$$

where $G(\hat{n})$, $L(\hat{n})$ are filtered gradient and lensing maps, T_l is the observed temperature map in Fourier space, and l is the angular multipole. Fourier filters W_l^T and W_l^{TT} are given by

$$W_l^T = (C_l^{TT} + N_l^{TT})^{-1} \quad (4.7)$$

$$W_l^{TT} = \tilde{C}_l^{TT} (C_l^{TT} + N_l^{TT})^{-1} \quad (4.8)$$

where $\tilde{C}_l^{TT}, C_l^{TT}$ is the unlensed and large scale structure lensed CMB power spectrum obtained from CAMB, N_l^{TT} is the experimental noise power spectrum. With filtered gradient and lensing maps in hand we can write down the expression for lensing convergence profile as

$$\hat{k}_l = -A_l \int d^2\hat{n} e^{i\hat{n}.l} \text{Re} \nabla \cdot [G(\hat{n}) L^*(\hat{n})] \quad (4.9)$$

where A_l is the normalisation parameter given by

$$\frac{1}{A_l} = \frac{2}{l^2} \int \frac{d^2l_1}{4\pi^2} (l.l_1) W_l^{TT} W_l^T (\tilde{C}_{l_1}^{TT}(l.l_1) + \tilde{C}_{l_2}^{TT}(l.l_2)) \quad (4.10)$$

where $l = l_1 + l_2$.

mitigating magnification bias:

Galaxy cluster magnifies the background image and decreases the observed temperature gradient behind it, which leads to a low bias in lensing reconstruction. The bias is due to the overlap in scales between the unlensed gradient field and lensed temperature field. Though wiener filter reduces the bias, the filter cannot remove the bias. We can reduce the bias further by exploiting the prior knowledge on unlensed CMB power spectrum. From Fig. 4.4, which shows the unlensed rms gradient as a function of multipoles, it is evident that most of the power for the gradient map comes from scales below $l < 2000$. By low pass filtering the gradient map, we separate the unlensed gradient and the lensed temperature field with

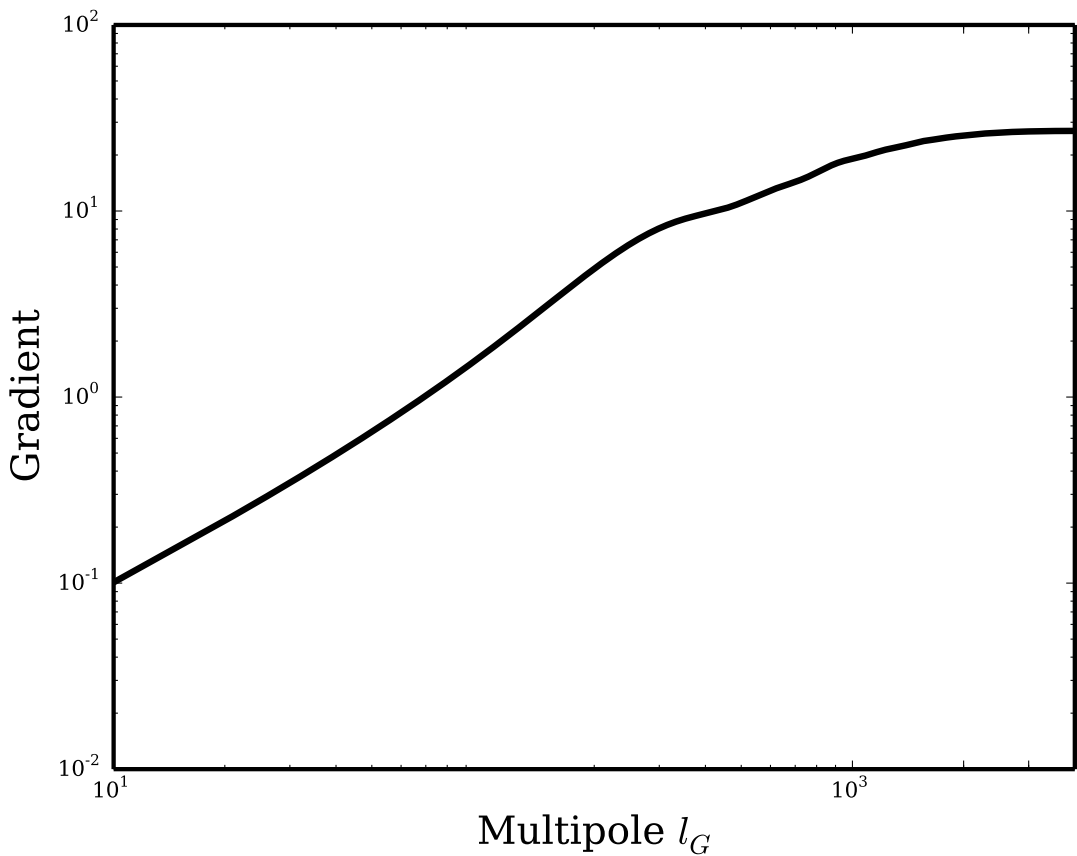


Figure 4.4: Gradient of temperature field as a function of low pass filter $l = l_G$. It is dominated by multipoles below 2000.

almost no loss in SNR (signal to noise ratio).

The schematic representation of quadratic estimator is shown in Fig. 4.3². Top panel is the 10'X 10' cutout of the observed temperature map. This is filtered in the fourier space (using Eqs. 4.8) to obtain the filtered gradient and lensed maps, shown in middle right and left panels respectively. Lensing convergence map is reconstructed by extracting the correlations between lensing and gradient maps which is shown in the bottom panel.

4.2.1 *removing SZ induced bias*

Though SZ is small spectral effect, it is still much higher than the lensing signal. It is an order of magnitude greater than the lensing signal and hence induces a significant systematic and statistical uncertainty if not taken into account. In this

²note that it is an ideal case, we haven't used either experimental noise level or foregrounds which are present in the real data

section we describe the modifications of quadratic estimator which eliminates the SZ induced bias, in the next chapter we discuss the method to reduce SZ induced variance. Fig. 4.5 shows the effect of SZ on the lensing convergence profile. In the left panel of figure we show the stacked lensing convergence profile of 1000 clusters each with a mass of $2 \times 10^{14} M_{\odot}$ and an experimental noise of $3 \mu\text{K}'$ with no SZ and on the right panel is with the SZ. As can be inferred from the plot, presence of SZ induces a blue blob in the center and hence resulting in a negative bias.

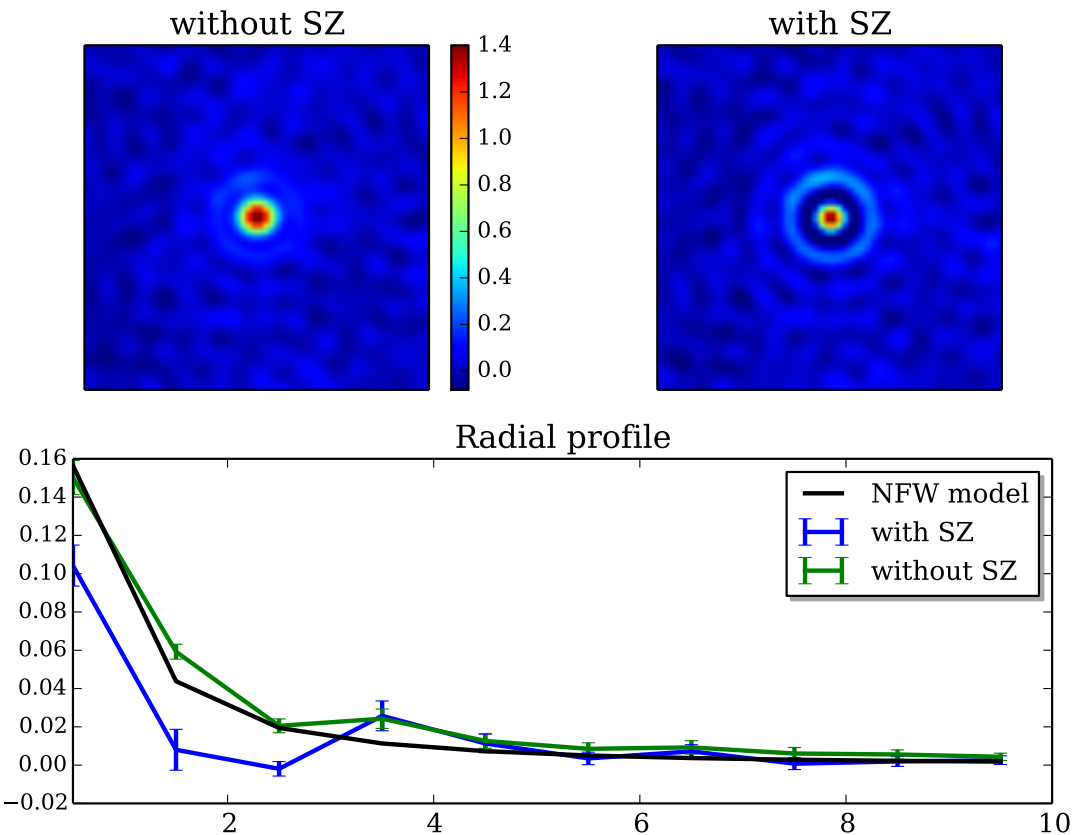


Figure 4.5: Effect of SZ on lensing convergence profile. On the top panel we show the lensing convergence profile for a stack of 1000 cluster each at a mass of $M_{200m} = 2 \times 10^{14} M_{\odot}$ and a redshift of $z = 0.7$ with experimental white noise level of $3 \mu\text{K}'$ – arcmin; left panel is without SZ and right panel is with SZ. On the bottom panel we have radial profile of the same in solid blue (without SZ) and green (with SZ) curves; black curve is the radial profile of the input NFW profile.

While designed to pull the lensing induced correlations, QE is equally sensitive to any other signal present in both G and L maps. SZ present in both maps

results in a low bias if not taken into account 4.5. Two methods have been discussed in literature to eliminated/mitigate the SZ bias: one of the ways to eliminate SZ bias is by using SZ free maps, which are constructed by exploiting the spectral dependance of SZ signal. However, this results in an increased statistical uncertainty in the reconstructed convergence profile. Another way to mitigate the bias is by using a more stringent low pass filter on the gradient map, having a robust separation of scales between gradient map and small scale map reduces SZ correlation. While this can reduce the bias significantly, poor gradient estimation results in an increased statistical uncertainty.

During my thesis we came up with a novel approach to completely remove the SZ bias. Any foreground signal which is present in both the maps (gradient and lensing) will lead to a systematic bias, so by getting rid of the foreground signal in one of the maps (either G or L) should eliminate the bias completely. As shown in Fig. 4.4, most of the gradient estimation comes from multipoles $l < 2000$ where CMB is not limited by experimental noise. So, natural choice would be to eliminate SZ in the gradient map by using linear combination of different frequencies. In modified quadratic estimator, eqn 3.6 becomes,

$$G(\hat{n}) = \nabla \left(\int \frac{d^2 l}{(2\pi)^2} e^{il \cdot \hat{n}} W_l^{TT} T_l^{SZ_{free}} \right) \quad (4.11)$$

where $T_l^{SZ_{free}}$ is an SZ-free map.

4.3 Data

In order estimate the mass of a cluster catalog all we need is cluster location and CMB map corresponding to cluster location. Both catalog and CMB map can come from the same experiment or from different experiments whose survey areas overlap. In our case we used data sets from two different experiments: CMB maps from South Pole Telescope explained in §4.3.1 and optical cluster catalog from Dark Energy Survey explained in §4.3.2

4.3.1 *South Pole Telescope*

South Pole Telescope (SPT) is a 10 meter diameter, wide field, offset Gregorian telescope (SPT, Carlstrom et al., 2011; Padin et al., 2008) located at the Amundsen-Scott South Pole station. The SPT has been operating since early 2007 and has completed two surveys so far: SPT-SZ (2007 -2011) and SPTpol

(2012-2016). Extremely dry and stable atmosphere of the South Pole makes it one of the best available sites on Earth for observing at millimeter and sub-millimeter wavelengths.

SPTpol 500 deg² survey

SPTpol is the second polarisation sensitive camera installed on the 10-meter South Pole Telescope (SPT, Padin et al., 2008; Carlstrom et al., 2011). The SPTpol focal plane consists of 1536 polarization-sensitive transition edge sensor bolometers (360 at 95 GHz and 1176 at 150 GHz) (Austermann et al., 2012). The SPTpol 500 deg² survey spans fifteen degrees of declination, from -65 to -50 degrees, and four hours of right ascension, from 22h to 2h. We briefly summarize the observation strategy, map making, and beam characterization, we suggest interested reader to refer Henning et al. (2018) for further details.

In this work, we use CMB temperature maps from observations between April 2013 and September 2016 in frequency bands centered at approximately 95 GHz and 150 GHz. Over this period, SPT used two different strategies to observe the field. From April 2013 upto May 2014 SPT observed the field in lead-trail strategy; for the rest of the observation period SPT adopted full-field strategy. In lead trail strategy the field is split into two halve in right ascension. Lead field is scanned first for a period of 2 hours, immediately followed by a 2 hour trail field scan. During lead-trail scan field and elevation steps are set such that the entire observation occurs over the same azimuth range. In order to increase sensitivity at large angular scales, SPT adopted full-field strategy for the rest of its observation period, where constant-elevation scans were made across the entire range of right ascension over 2 hour period.

The telescope beam and pointing solutions were characterized by observing Venus. SPTpol made seven observations of Venus. From these seven observations we calculate the 21 independent cross power spectra and take the average to characterize beam B_l . The beam covariance is estimated as the noise variance of these 21 independent cross-spectra. Broadening of beam is caused by two sources: rms pointing error and finite size of Venus. However, during the analysis it was found that broadening due to finite size of Venus (which was ~ 11 arc seconds) is negligible. The final telescope beam along with the pointing jitter roughly corresponds to a $\theta_{\text{FWHM}} = 1.^{\circ}22$ ($1.^{\circ}7$) Gaussian for the 150 (95) GHz dataset.

The raw data is composed of digitised time-ordered data (TOD) for each

detector that are converted into CMB temperature units. We bin the TOD into two different maps using a flat-sky approximation in the Sanson-Flamsteed projection (Calabretta and Greisen, 2002; Schaffer et al., 2011). To construct the first map, in which we aim to reconstruct the small-scale lensing signal, we remove large-scale modes $\ell \leq 300$, bandpass filter the TOD in the range of approximately $300 \leq \ell_x \leq 20,000$, and bin them into $0.^{\circ}5$ square pixels. For the second map, intended for estimation of the large-scale CMB gradient, we apply minimal TOD filtering by only removing modes below $\ell_x \leq 30$, and bin them into $3'$ square pixels. While we only use the data from the 150 GHz channel for the first map, the latter is a SZ signal cleaned map produced by linearly combining the 95 and 150 GHz channels. We use this SZ-free map to reconstruct the background gradient of the CMB at the cluster locations. The minimal filtering on this map allows us to recover large-scale modes which indeed helps in a better estimation of the background gradient. The $0.^{\circ}5$ resolution of 150 GHz temperature map has a white noise level of $\Delta_T = 6 \mu\text{K}'$ estimated using a jackknife approach. The low-resolution SZ-free combination is noisier with $\Delta_T \sim 17 \mu\text{K}'$. Fig. ?? shows the noise power spectrum of temperature and polarisation maps. Top panel in the figure represents the temperature noise power spectrum, bottom two panels correspond to polarisation stokes Q and U maps.

4.3.2 DES and the redMaPPer catalog

The Dark Energy Survey (DES) was a $\sim 5000 \text{ deg}^2$, optical to near-infrared survey conducted using the Dark Energy Camera (Flaugher et al., 2015) mounted on the 4-meter Victor Blanco telescope at Cerro Tololo Observatory in Chile and has recently finished its survey. For this analysis, we use the cluster catalog obtained from the first three years of DES observations, which almost covers the SPTpol 500 deg^2 survey.

The cluster catalog was derived using the redMaPPer (RM) algorithm (Rykoff et al., 2014). RM is an optical cluster-finding algorithm which detects candidates by identifying over-densities of luminous red galaxies with luminosity greater than 20% of L_* . It is based on our understanding that galaxy clusters are agglomerations of galaxies containing old and subsequently red stars. The algorithm iteratively assigns membership and centering probabilities for each red galaxy identified as belonging to a cluster candidate. A weighted sum of the membership probabilities, richness λ , is assigned to each candidate. The centre comes

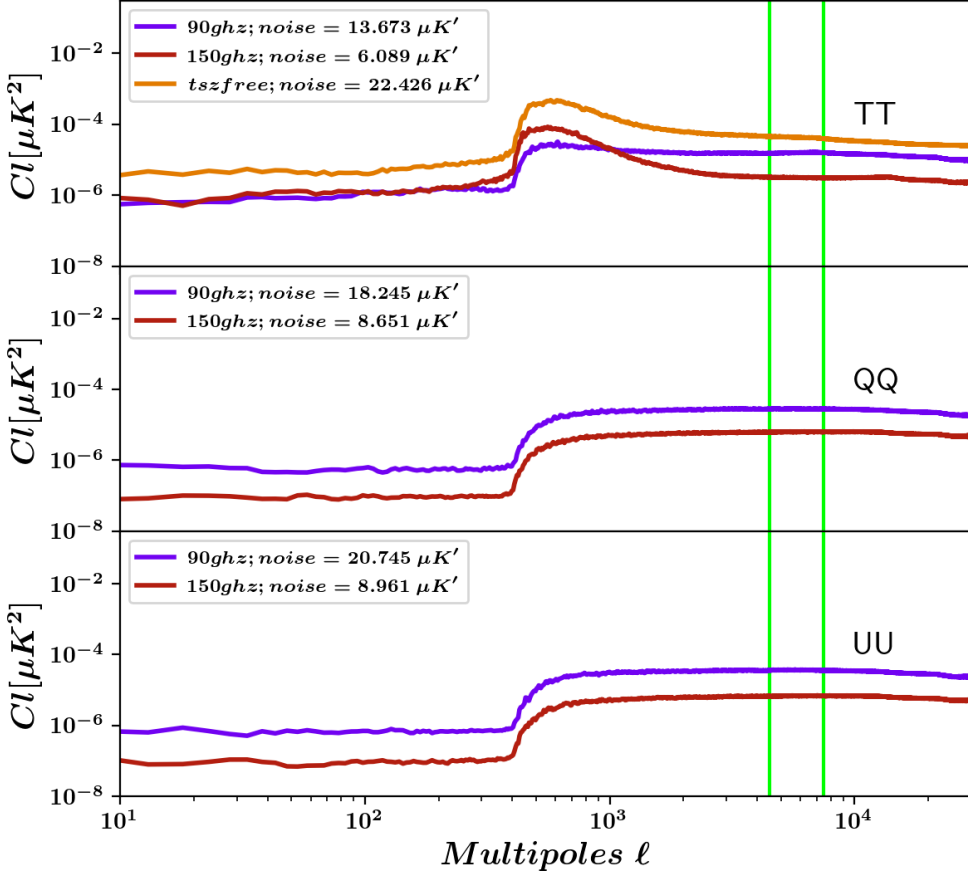


Figure 4.6: SPTpol noise power spectrum of temperature and polarisation maps.

from the galaxy with the highest centering probability. The DES RM catalog contains two samples: a flux-limited sample and a volume-limited sample. The flux-limited sample has more high-redshift clusters detected from deep fields in the survey. On the other hand, the volume-limited sample is independent of survey depth, complete above a luminosity threshold McClintock et al. (2018), and normally preferred for cosmological analysis. See Rykoff et al. (2016) for more information on the application of RM to the DES survey data.

The RM cluster catalog version employed in this analysis is y3_gold:v6.4.22. The Year-3 gold catalogue is based on the previous catalog from the Year-1 data (Drlica-Wagner et al., 2018) with some updates described in Morganson et al.

(2018). The catalog contains 54,112 clusters above richness $\lambda \geq 20$ in the flux-limited sample and 21,094 clusters in the volume-limited sample. Of these, 5,828 (2,428) clusters from the flux(volume)-limited sample lie within the SPTpol 500 deg² survey in the redshift range $0.1 \leq z \leq 0.95$ (0.90). We additionally remove clusters near the survey edges with more than 5% masked pixels or within 10' distance from any bright (≥ 6 mJy at 150 GHz) point sources detected in the SPTpol temperature map. These cuts leave 4,003 (1,741) clusters with $\lambda \geq 20$ from the flux(volume)-limited sample with a median redshift of $\tilde{z} = 0.77$ (0.48). The error in the cluster photo- z estimates are small with $\hat{\sigma}_z = 0.01(1+z)$ (Rozo et al., 2016).

4.3.3 CLUSTER CUTOUTS

We extract 300'square box form SPTpol temperature maps at the DES cluster locations. While the boxsize is much larger than the virial radius of the cluster, it is necessary to robustly approximate the background gradient. This is because much of the gradient power comes from larger scale modes, reducing the analysis to a smaller box will reduce the SNR of the mass estimation. These cutouts are then passed through the pipeline to extract lensing convergence profile, after which we limit the modelling and likelihood calculations to 10'box around a cluster to lessen the computational effort.

As mentioned before, the lensing signal is weak for individual cluster and we need to stack lensing convergence profiles to increase the SNR of detection. Thus the stacked convergence map is simply:

$$\hat{\kappa} = \frac{\sum_j w_j [\hat{\kappa}_j - \langle \hat{\kappa}_j \rangle]}{\sum_j w_j} - \hat{\kappa}_{\text{MF}}, \quad (4.12)$$

where $\hat{\kappa}_j$ refers to reconstructed convergence map of cluster j and the weighting scheme w is described below. From the stacked map, we remove all modes above the SPTpol 150 GHz beam scale of $\theta_{\text{FWHM}} \sim 1.^{\circ}2$. We also remove an estimate of the mean-field $\hat{\kappa}_{\text{MF}}$ from this stacked convergence map. The mean-field arises because of two reasons. One because the temperature maps are apodized using a Hanning window with a 10' edge taper to reduce edge effects which induces undesired mode correlation. The other reason is the presence of inhomogeneous noise in the survey region. We obtain the mean field bias by stacking the convergence maps reconstructed at 50,000 random locations in the maps.

Weighting scheme: While using SZ-free gradient map we completely eliminated the SZ-induced bias, SZ present in the lensing map induces extra variance. SZ variance is proportional to the SZ brightness and as expected is higher for massive clusters scaling roughly as $M^{5/3}$. In the next chapter, we will discuss in detail a refined mQE to suppress the SZ induced variance. However, here we just down weigh the clusters based on their SZ variance. We decompose the weights assigned for each cluster into two components: inverse noise variance weight and SZ weight. The inverse-noise-variance weight, w_k , constructed from the observed standard deviation σ_κ in the reconstructed SPTpol convergence maps in a ring between $10'$ and $30'$ around the cluster. The noise in convergence is proportional to the noise in the associated gradient map and increases, as expected, when ℓ_G is reduced.

The second³ weight comes from the noise in the convergence maps due to the presence of SZ signal in the second leg of the QE, the SPTpol 150 GHz map. We obtain this second set of weights, w_{SZ} , using simulations. For every cluster in the DES sample, we reconstruct the convergence profile using a simulated SZ-free gradient map and a 150 GHz map with SZ signal assuming an Arnaud profile (Arnaud et al., 2010) with a log-normal scatter of 20% in the $Y_{\text{SZ}} - M$ relation. We pass these simulated cutouts through our pipeline and we turn off cluster lensing as the objective here is to only get an estimate of the SZ-induced noise in the convergence maps. A total of 25 simulations were used to get the noise estimate for each DES cluster. The weights are estimated as $w_{\text{SZ}} = 1/\sigma_{\text{SZ}}^2$, where σ_{SZ} is the standard deviation of the ‘null’ convergence map within an angular distance of $10'$ from the cluster centre. The errors increase with richness and take a power law form parameterized as $\sigma_{\text{SZ}}(\lambda) = \sigma_0 \lambda^\alpha$ with values $(\sigma_0, \alpha) = (0.0045, 1.55)$. The results are unchanged if we derive the weights using the SZ signal from Sehgal et al. (2010). The total weight is now:

$$w = \frac{1}{\sigma_\kappa^2 + \sigma_{\text{SZ}}^2}. \quad (4.13)$$

Introducing w_{SZ} down weighs the most massive clusters, reducing the contribution of clusters with $\lambda \geq 60$ to less than 1% in the final stacked sample. Note that we have only 40 clusters above $\lambda > 40$ and down weighing doesn’t sig-

³We note that for the mean-field reconstructed from random locations, we only apply the weight $w = 1/\sigma_\kappa^2$ for stacking.

nificantly reduce the SNR. However for future low noise surveys down weighing will suppress the contribution of large number of clusters. An alternative to this down-weighting is to swap the maps in the two legs of the QE (i.e. the 150 GHz map for the gradient estimation and the SZ-free map to reconstruct lensing) for clusters with $\sigma_{\text{SZ}} > \sigma_\kappa$, which is approximately true for clusters with $\lambda > 40$. However, this results in a minimal gain as the SPTpol SZ-free map has a higher noise ($\times 3$) compared to the SPTpol 150 GHz maps. In the next chapter, we discuss the template fitting approach used to reduce the SZ variance significantly.

4.4 Model Fitting

With the cluster cutouts obtained from 4.3.3 and method to extract convergence profile (4.2) in hand, we are ready to fit model to the observed convergence. To obtain the mass of the cluster, we need to compare the observed lensing profile to the convergence model generated using an assumed halo mass profile. The observed lensing convergence profile of cluster has contributions from its own halo density (k_{1h}) as well as from the correlated structures along the line of sight known as two halo term (k_{2h}). For k_{1h} , we assume the galaxy cluster density to follow Navarro Frenk White (NFW) profile and in 4.5.2 we quantify the robustness of this assumption by using Einasto profile (Einasto and Haud, 1989). A NFW halo profile is characterized by its scale radius R_s , the dimensionless concentration parameter c , and the dimensionless characteristic over-density δ_c . The lensing convergence profile for NFW is obtained as discussed in the previous chapter ?? which we represent as $k(\theta)$. With the model prediction in hand, we can then write down the likelihood of observing the real data as:

$$-2 \ln \mathcal{L}(\hat{\kappa}(\theta) | M) = \sum_{\theta, \theta'=0}^{10'} [\hat{\kappa}(\theta) - \kappa(\theta)] \hat{C}_{\theta, \theta'}^{-1} [\hat{\kappa}(\theta') - \kappa(\theta')] \quad (4.14)$$

where $\hat{\kappa}(\theta)$, $\kappa(\theta)$ are the azimuthally averaged radial profiles of the stacked data and model convergences respectively, binned in 10 linearly spaced intervals with $\Delta\theta = 1'$. To obtain the covariance matrix we use a jackknife re-sampling technique. We divide the SPTpol 500 deg² region into $N = 500$ sub-fields and estimate the covariance matrix for the radially binned convergence profile as

$$\hat{C} = \frac{N-1}{N} \sum_{j=1}^{N=500} [\hat{\kappa}_j(\theta) - \langle \hat{\kappa}(\theta) \rangle] [\hat{\kappa}_j(\theta) - \langle \hat{\kappa}(\theta) \rangle]^T, \quad (4.15)$$

where $\hat{\kappa}_j(\theta)$ is the azimuthally binned stacked convergence of all the clusters in the j^{th} sub-field and $\langle \hat{\kappa}(\theta) \rangle$ is the ensemble average of all the 500 sub-fields. We test this approach by alternatively estimating the covariance matrix using 500 realizations of the random convergence stacks. We do not note any significant differences between the uncertainties estimated using the two approaches. We apply the Hartlap et al. (2007) correction to \hat{C}^{-1} to account for the noise in covariance estimation due to the finite number of jackknife re-sampling.

4.5 pipeline verification

In this section, we describe tests used to investigate the known and unknown systematic effects in the data and to validate the pipeline. We start with the test for unknown systematics through the “curl” null test (§4.5.1). Next we calculate the expected systematic error budget from known sources of systematic uncertainty (§4.5.2).

4.5.1 “*Curl*” null test

We perform a “curl” null test (Hu et al., 2007) at 4003 cluster locations from the DES RM Year-3 flux-limited sample. Specifically, we replace the divergence of the gradient field, $\nabla \cdot [G(\hat{\mathbf{n}})L^*(\hat{\mathbf{n}})]$, in Eq. (5.3) with the curl operator. Since the curl of a gradient field is zero, the reconstructed field should be consistent with zero unless there is a systematic bias in the data. The result of the curl test is shown in Fig. 4.5.1. We radially bin the test result similar to the cluster stack as described in §4.4 and compare it to a null signal. The test returns a probability to exceed (PTE) value of 0.26 consistent with a null signal.

4.5.2 Systematic error budget

Now we consider possible sources of systematic error. We estimate the bias due to each cluster’s SZ emission and residual foregrounds, the assumption of an underlying cluster profile, uncertainties in the DES RM mis-centering parameter f_{mis} , approximations to the filter transfer function (Eq. ??), uncertainties in the beam measurements, and the assumption of a background cosmology. Another source of systematic error is the uncertainties in the cluster redshifts estimated photometrically. However impact of photo- z errors was estimated to be negligible by Raghunathan et al. (2017), and we ignore them here.

We rely on the Sehgal et al. (2010) simulations to estimate the level of residual-

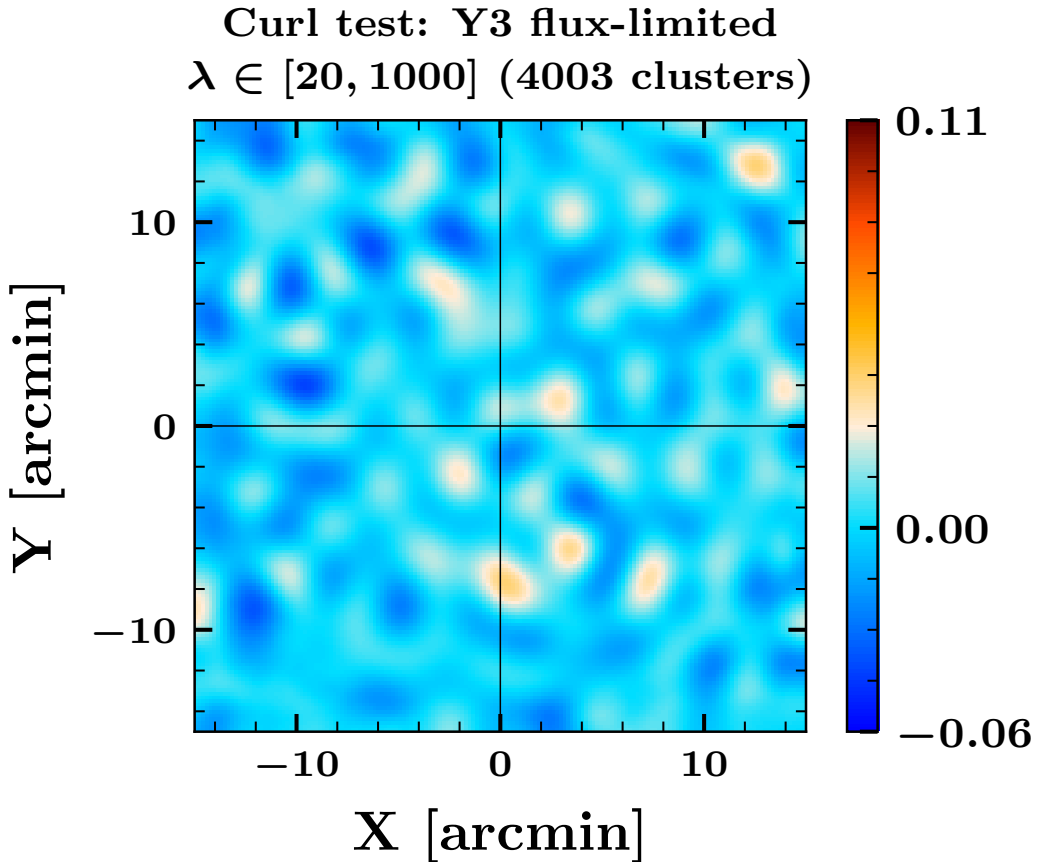


Figure 4.7: Stacked result of the curl test performed at the cluster locations by replacing the divergence operator in Eq. (5.3) with a curl operator. We obtain a PTE value of 0.26, consistent with a null result. For the ease of visual comparison we adopt the same colour scale as in Fig. 4.10.

SZ/foreground bias in the RM Year-3 flux-limited sample. In all the other cases we use the data and report the shift in the average lensing mass of the clusters in the RM Year-3 volume-limited sample obtained in §5.2. The combined systematic error budget is presented in Table ???. The systematic error calculated as a quadrature sum of the errors presented in Table ?? is much smaller than the statistical error in the measurements at a level of 0.15σ . Using a direct sum, the combined error budget is 0.27σ . The dominant error comes from the uncertainty in the DES RM cluster centroids shifting the mean lensing mass by 2.8%.

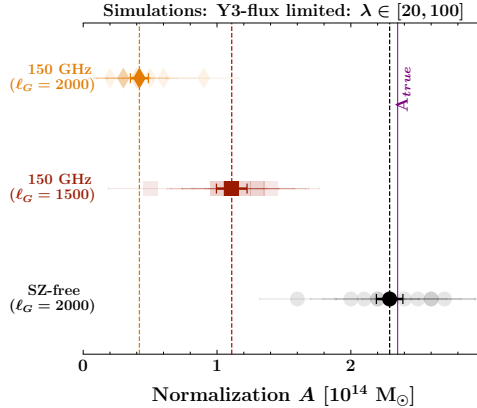


Figure 4.8: Quantifying the level of bias due to residual foregrounds and the SZ signal using S10 simulations. The recovered lensing mass, un-biased for the fiducial case with SZ-free map for gradient estimation and $l_G = 2000$ is shown as black circles. The equivalent biased results with just the 150 GHz map and $l_G = 1500$ (2000) cutoff scales for the gradient estimation are shown as red squares (orange diamonds). Each light shaded point corresponds to an individual simulation run with clusters from the ES RM Year-3 flux-limited sample. The darker data points are the values obtained for $10 \times$ the sample size

Cluster SZ signal and residual foregrounds

In this work we eliminate the bias due to SZ signal in the reconstructed lensing maps using maps to estimate the background gradient of the CMB. However, projecting just the SZ signal out tends to modify other frequency-dependent foregrounds, and the resultant map is not an optimal foreground-free CMB map for the lensing reconstruction. This enhancement of foregrounds generally acts as an additional source of noise and tends to increase the variance of the reconstructed lensing maps. At the cluster locations, however, an increase in foreground emission due to galaxies inside the cluster can introduce undesired mode coupling between the estimated gradient map and the lensing map resulting in a biased lensing signal. Since massive clusters host more galaxies, we can expect the bias to increase with the cluster mass or equivalently richness. Here we quantify this bias using the Sehgal et al. (2010) foreground simulations.

To this end, we begin with the simulated skies described in §??[in previous chapter](#), to which we then add simulated clusters, including the lensing signal (only the *1-halo* term), thermal and kinetic SZ effects, and emission associated with the cluster (e.g. from member galaxies). These simulations also include foregrounds uncorrelated with the clusters such as field radio galaxies. The addition

of foregrounds using Sehgal et al. (2010) simulations is described below. Note that the foreground maps, whether associated with the cluster or not, are not lensed by the cluster in these simulations. The number of simulated clusters and their redshifts and richesses are derived from the DES RM Year-3 flux-limited sample. The richesses and redshifts are converted to cluster masses according to the $M - \lambda$ relation (Eq. 4.17) with best-fit parameters from Melchior et al. (2017), $A_{M17} = 2.35 \times 10^{14} M_\odot$, $\alpha_{M17} = 1.12$, and $\beta_{M17} = 0.18$.

For foregrounds, we extract half-arcminute resolution $300' \times 300'$ cutouts of the 95 and 150 GHz Sehgal et al. (2010) simulations of the SZ, kSZ, radio, and infrared galaxies around halos corresponding to the mock cluster sample. We scale the SZ power down from the Sehgal et al. (2010) simulations by a factor of 1.75 to match the George et al. (2015) measurements. These foreground cutouts are added to our mock galaxy cluster lensed CMB datasets. The maps are then processed in the same way as explained in §?? to extract the SZ cleaned map and passed into the QE.

We present the results in Fig. 4.8. The true normalization is shown as the purple solid line. In the figure, the light shaded data points are the result for a single simulation run (~ 4000 clusters) and the darker data points are the results for $10\times$ the sample size. We obtain $A = 2.30 \pm 0.09 \times 10^{14} M_\odot$ (black circle) implying no significant residual foreground bias in the lensing measurements. This result also provides evidence that the lensing pipeline is unbiased.

Comparison to standard QE: We also use the Sehgal et al. (2010) simulations to compare the modified QE to the standard case using the 150 GHz map for the background CMB gradient estimation. In the standard case, the correlations introduced between the two maps by the foregrounds, the SZ signal in particular, can be alleviated by lowering the LPF threshold ℓ_G for the gradient map as in Eq. (??). As described in §??, the choice of ℓ_G is a trade-off between the level of foreground bias and the lensing S/N . Here we adopt $\ell_G = 2000$ and $\ell_G = 1500$ and note that the results are heavily biased in both cases: red squares (orange diamonds) for $\ell_G = 1500$ ($\ell_G = 2000$). The level of bias is higher when ℓ_G is set to 2000 compared to 1500, as expected. This bias is predominantly due to the SZ signal and can be reduced by removing massive clusters from the analysis as in Baxter et al. (2018). For comparison, when we apply a richness cut of $\lambda \in [20, 40]$ the lensing bias is reduced from 82% to 65% for $\ell_G = 2000$ and 52% to 35% for $\ell_G = 1500$. This cut removes ~ 500 massive clusters from the analysis.

This result can be compared to the conservative SZ-bias of 11% set by Baxter et al. (2018) with $\ell_G = 1500$ for the same richness range $\lambda \in [20, 40]$. Baxter et al. (2018) obtained a lower bias value as the high- ℓ modes in the SPT-SZ maps are down-weighted due to 4× higher noise.

Finally, a subtle point from the figure is that the mass constraints obtained using the 150 GHz map for gradient estimation (orange diamonds) are better ($\sim 14\%$) than those obtained using the SZ-free map for gradient estimation (black circles) despite adopting $\ell_G = 2000$ in both cases.

Cluster profile

In our fiducial analysis, we assume that the underlying halo profile of the clusters follows the NFW dark matter model. However, halos in real clusters deviations from the NFW profile have been observed (e.g., Diemer and Kravtsov, 2014), and Child et al. (2018) argued that the Einasto model is a better fit than NFW to stacked halo profiles.

In this section, we estimate the magnitude of a possible bias due to the assumption of the incorrect mass profile by using an Einasto profile (Einasto and Haud, 1989) to model the lensing convergence κ^{1h} . The lensing QE and subsequently the reconstructed convergence maps remain unchanged. The Einasto profile is defined as

$$\rho(r)_{\text{Ein}} = \rho_0 \exp\left(-\frac{2}{\alpha} \left[\left(\frac{r}{R_s}\right)^\alpha - 1\right]\right), \quad (4.16)$$

where $\alpha = 0.18$ is the shape parameter (Ludlow et al., 2013). As in the NFW analysis, the concentration c_{200} as a function of mass and cluster redshift is obtained using the Duffy et al. (2008) relation. We use the general framework for spherically symmetric halos defined in Raghunathan et al. (2017) and simply plug the above density profile into Eq. (2.9) of Raghunathan et al. (2017) to obtain the Einasto convergence $\kappa^{1h,\text{Ein}}$ profiles. The κ^{2h} term remains the same. For the Einasto case we see a negligible shift of 0.01σ compared to our fiducial result.

Uncertainties in filter transfer function and beam

As described in §4.3, the SPTpol map-making process is lossy, with noisy modes along the scan direction filtered out. The ideal, if computationally expensive, approach to handle the filtering would be an end-to-end simulation from the

TOD to the lensing reconstruction. In this work, we take a computationally much cheaper approach and approximate the filtering by the phenomenological fit to the filter transfer function in Fourier space given by Eq. (??). The major uncertainty is in the position of the high-pass filter (HPF) in the scan direction: this filters modes more strongly than the isotropic HPF, and the LPF is at angular scales that do not matter to the reconstruction. The estimated position for this HPF is $\ell_x = 300 \pm 20$. We also recompute the models for an assumed $\ell_x = 280$ and 320 to evaluate the shifts in the lensing masses. We note no significant effect (masses shift by roughly $\pm 0.02\sigma$), indicating that the uncertainty in the simplified filtering treatment causes negligible changes to our results.

Similarly, we also check the effect of errors in the telescope beam modeling B_ℓ that were derived using Venus observations (see §4.3.1). We find that the effect due to beam uncertainties in the final result is also negligible. The shift in the lensing mass is

Underlying cosmology

The systematic error arising due to the assumption of a background cosmology is quantified here. As described in earlier sections, in our fiducial analysis we use the Λ CDM cosmology obtained using the h_p 2015 datasets (Planck Collaboration et al., 2016b). Here we repeat the analysis by modifying the lensed CMB power spectra C_ℓ to include the 1σ errors to the h_p 2015 cosmological parameters. Modifying the background cosmology alters the weights of Eq. (??) in the lensing estimator and also the model convergence profiles $\kappa^{1h}(M, z)$ and $\kappa^{2h}(M, z)$. However, the effect due to background cosmology in the inferred lensing mass is negligible with a shift in the lensing mass

4.6 Results and Discussion

The main results of this work are the lensing-derived cluster mass constraints for the DES RM Year-3 cluster samples using SPTpol SZ-free \times 150 GHz temperature maps. Below, we first present the lensing mass estimates in §4.6.1 and use the lensing measurements from the DES Year-3 volume-limited sample to independently calibrate the $M - \lambda$ relation of the cluster sample in

4.6.1 *Stacked mass measurements*

In Fig. ??, we present the results of our stacked lensing measurements. The left (right) panel correspond to the convergence maps stacked at the location

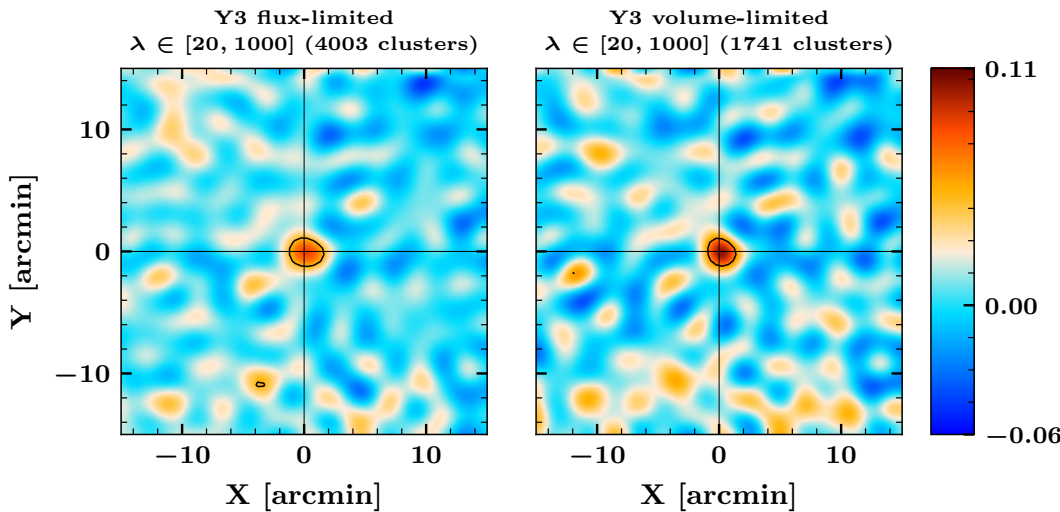


Figure 4.9: The inverse-variance weighted stacked convergence maps at the location of 4002 and 1741 clusters in the range $\lambda \in [20, 1000]$ from flux limited (left) and the volume-limited (right) samples of the DES RM Year-3 cluster catalog. The contour corresponds to the regions above 3.5σ . The null hypothesis of no-lensing is rejected at 8.7σ and 6.7σ for the two cases respectively.

of clusters in the DES Year-3 flux(volume)-limited sample. The variance in the flux-limited sample is lower than the volume-limited sample because the flux-limited sample has twice as many objects. An estimate of the mean-field has been subtracted from the maps. We reject the null hypothesis of no lensing with a significance of 8.7σ for the flux-limited sample of 4003 clusters. The obtained S/N is consistent with our expectations from the simulations shown as lighter black circles in Fig. ?? For the smaller volume-limited sample, the no-lensing hypothesis is ruled out at 6.7σ . The radially binned convergence profiles that are used to estimate the cluster masses are shown in Fig. ?? along with the best-fit model curves.

The ringing pattern is because of the sharp filtering of modes above the SPT-pol beam scale. The error bars plotted are the square root of the diagonal entries of the covariance matrix estimated using The recovered lensing masses for the stacked flux and volume-limited samples are According to expectations, the lensing masses shift up by 0.3σ when the 2 -halo term is excluded.

A higher mean mass is expected for the volume-limited sample. At redshifts above $z \sim 0.6$, galaxies at the luminosity threshold adopted by RM become too faint to be detected in the DES data. Consequently, the richness of the clusters is

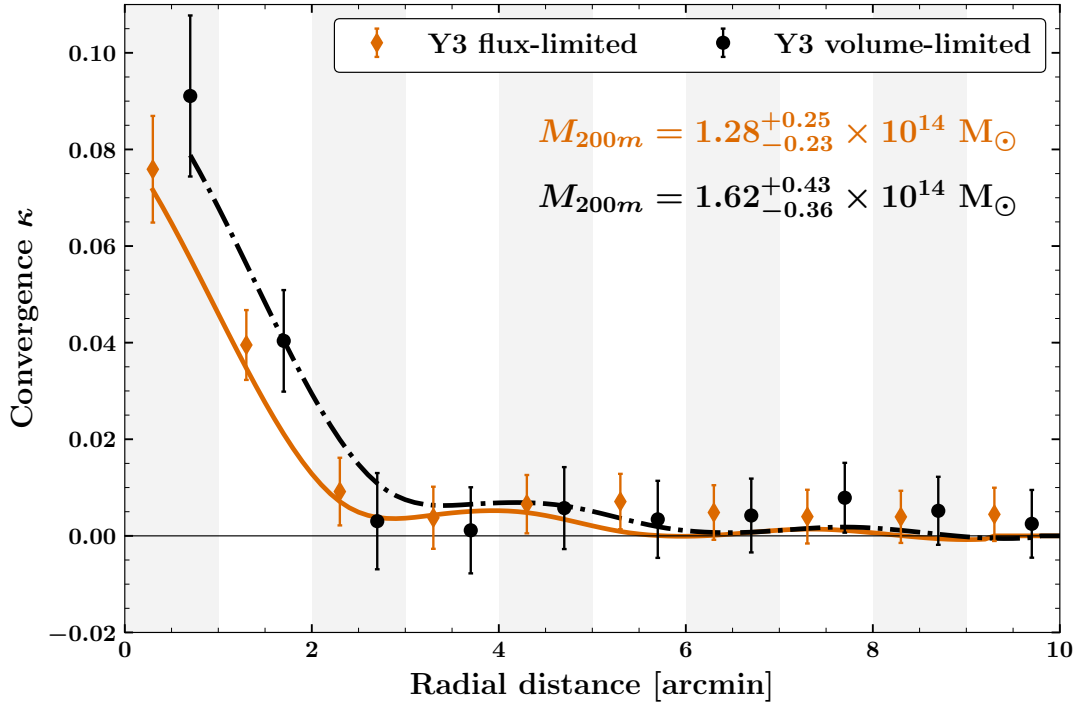


Figure 4.10: The azimuthally averaged radial profile of the stacked convergence maps from Fig. 3. The black circles and orange diamonds correspond to the flux and volume-limited Year-3 DES RM cluster samples. The error bars are the diagonal value of the covariance matrix estimated using the jackknife technique in Eq. (10). The data points for the two sample have been artificially shifted from the bin centres to avoid cluttering.

extrapolated from the subset of galaxies that are sufficiently bright to be detected. This extrapolation introduces additional noise in the richness estimates. The increased scatter leads to more low-mass systems scattering up to apparently rich systems, thereby lowering the mean mass of the selected halos. For this reason, we restrict our analysis to the volume-limited sample in the subsequent sections.

4.6.2 Mass-richness $M - \lambda$ scaling relation calibration

We now apply the lensing mass measurements from §4.6.1 to constrain the relationship between a cluster’s mass, M , and optical richness, λ , in the DES RM Year-3 volume-limited sample. We limit the analysis to just the volume-limited sample since the flux-limited sample has selection bias as explained above in §4.6.1. Following earlier weak-lensing analyses of RM clusters (Simet et al., 2018;

Melchior et al., 2017; McClintock et al., 2018), we use a power-law scaling relation for cluster mass, M , as a function of richness, λ , and redshift, z ,

$$M = A \left(\frac{\lambda}{40} \right)^\alpha \left(\frac{1+z}{1+0.35} \right)^\beta, \quad (4.17)$$

where A is a normalization parameter, and the exponents α and β are richness and redshift evolution parameters respectively. The pivot points for the richness and redshift evolution were set based on DES weak-lensing measurements of McClintock et al. (2018). The model for the stacked mass is

$$M(A, \alpha, \beta) \equiv M = \frac{\sum_j w_j M(\lambda_j, z_j)}{\sum_j w_j}, \quad (4.18)$$

where the sum runs over the number of clusters in the sample and the weight w for each cluster is given in Eq. (4.13).

We do not split the stacks into different richness or redshift bins. As a result, the data's sensitivity to the two evolution parameters is minimal and we apply informative priors to both. We perform a Markov chain Monte Carlo (MCMC) analysis using the publicly available *emcee* (Foreman-Mackey et al., 2013) code to sample the likelihood space.

4.6.3 Comparison to literature

We now compare our results to similar works from the literature performed with the RM cluster catalogs from the SDSS and DES experiments. Since the richness estimated for a given cluster from surveys A and B can vary slightly depending on the adopted data reduction and analysis choices, we include a small correction factor ϵ_{A-B} when comparing results from two surveys. We compute the ratio λ_A/λ_B for the overlapping clusters in the two surveys and simply set ϵ_{A-B} to the median value of the ratios. We find the richness estimates in DES Year-3 and Year-1 to be consistent with $\epsilon_{Y3-Y1} = 1$. For the rest, we set: $\epsilon_{Y3-SV} = 1.08$ and $\epsilon_{Y3-SDSS} = 0.93$ McClintock et al. (2018). The comparison after including this correction factor is presented in Fig. 4.12, which is similar to Fig. 15 in McClintock et al. (2018). The figure is normalized using the 1σ error from the current work with the Year-3 volume-limited DES RM catalog sample.

Each analysis uses a different cluster sample and lensing data. Simet et al. (2018) and Geach and Peacock (2017) use the SDSS RM catalog sample contain-

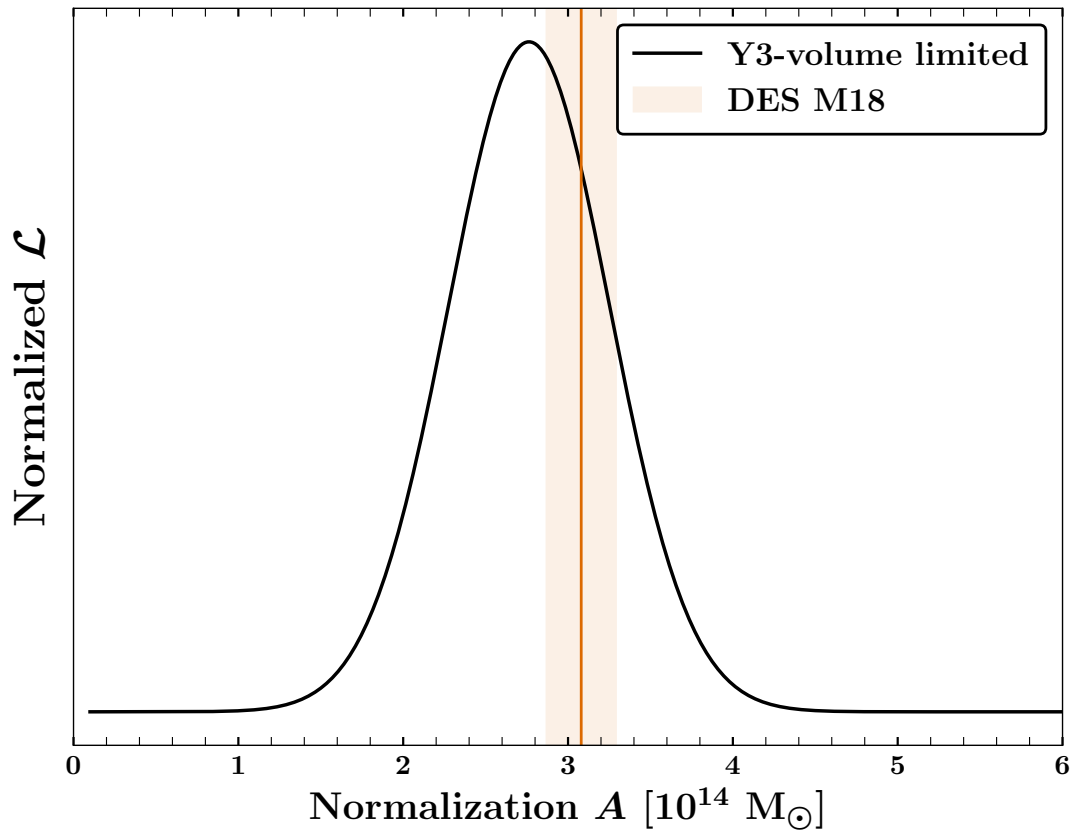


Figure 4.11: Marginalized posteriors of the normalization parameter A of the $M-\lambda$ relation for the volume-limited sample of the RM cluster-catalog. The result is consistent with the best-fit values obtained by DES weak-lensing measurements (M18), shown as the shaded region

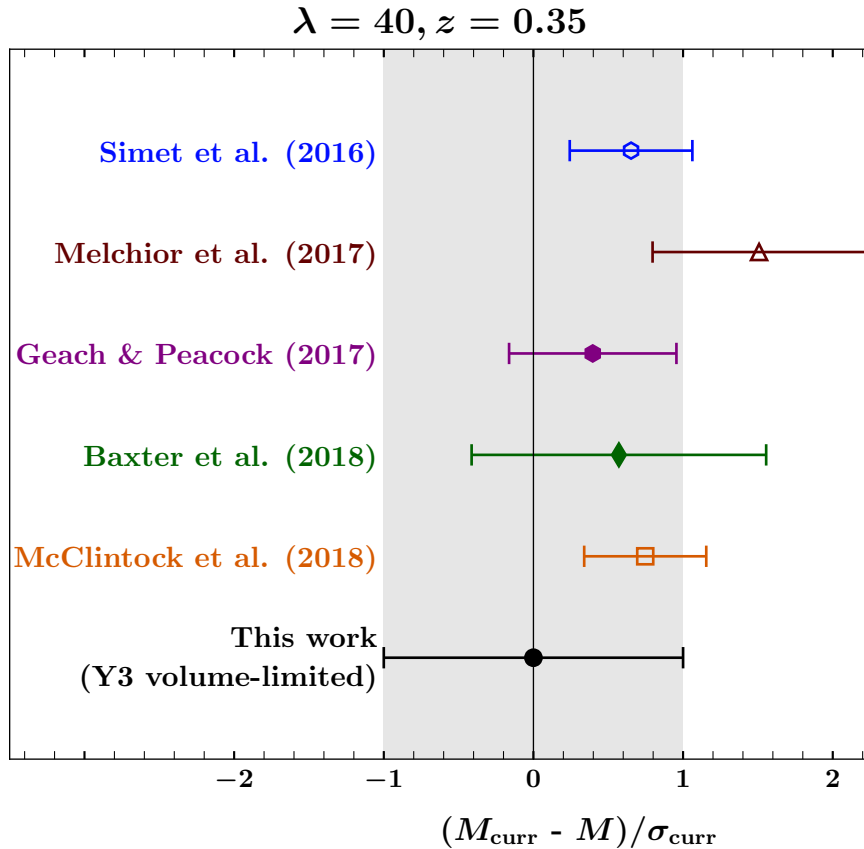


Figure 4.12: Comparison of M_{200m} mass estimates of galaxy clusters obtained using the $M-\lambda$ relation from different works in the literature using the RM cluster catalogs. The points have been normalized using the 1σ error from the analysis with the Year-3 volume-limited sample of the DES RM catalog. The filled (open) points represent measurements using the CMB-cluster lensing (galaxy weak-lensing) technique

ing roughly 26,000 clusters. Melchior et al. (2017) use the full catalog from the DES science verification data while Baxter et al. (2018) and McClintock et al. (2018) perform the analysis using the DES Year-1 volume-limited sample. The works by Geach and Peacock (2017) and Baxter et al. (2018) use the CMB-cluster lensing technique (filled points) with h_p and SPT-SZ CMB temperature maps. All the others use galaxy weak-lensing measurements and are represented as open points. As evident from the figure, our results are consistent with other similar works in the literature.

Chapter 5

Template Fitting

Modified Quadratic Estimator (mQE) developed in the last chapter completely eliminates the thermal Sunyaev-Zel'dovich (SZ) bias by using a SZ free gradient map. Though SZ bias is removed in mQE, SZ present in the second leg induces extra variance in the reconstructed lensing convergence profile. Unlike the variance due to other sources such as instrumental noise, uncorrelated foregrounds etc., SZ variance depends on the mass of the galaxy cluster. SZ variance scales roughly with the mass of cluster as $M^{5/3}$. For DES X SPTpol clusters which we used in the last chapter, we downweighed the massive clusters to take the SZ variance into account. This didn't have much effect on the final SNR as we had only few massive clusters. However, with future low noise CMB surveys such as SPT-3G, CMB-S4, Simons Observatory etc., downweighing won't be an optimal solution. The chapter is organised as follows: in §5.1 we describe the template fitting approach which will significantly reduce SZ variance, followed by results in §??. We forecast mass uncertainties future experiments using our proposed method in section 5.3 and then we finally conclude in section.

5.1 Method

In this section, I present template fitting approach which will significantly reduce the SZ variance in high mass cluster and/or low noise surveys. I then discuss the effect of SZ variance and experimental variance as a function of experimental noise and cluster mass.

5.1.1 *Template fitting to reduce the SZ variance*

An obvious way to eliminate this SZ variance is by using SZ-free maps for both the small-scale and gradient maps. Of course this would undo the advantages of the modified QE for the instrumental noise in the small scale map. One can also reduce this extra variance by projecting out a model template for the SZ signal, and thereby reducing the total amount of SZ power in the small-scale map. Given

the impossibility in creating a ‘perfect’ SZ template, the template fitting will not completely eliminate the SZ signal in the small-scale map. However, template fitting can significantly reduce the SZ power in the small-scale map, and thus reduce the SZ noise penalty on the lensing mass reconstruction.

To be unbiased, we must fit the template to a CMB-subtracted map or account for the information loss from template projection in the normalization factor A_l of Eqn. 5.3. The latter tact (correcting A_l) might have advantages if one needed to suppress multiple kinds of cluster emission, e.g., dusty and radio galaxies in addition to the thermal SZ effect. Projecting a template from the Compton- y map will either not help these other cluster signals. However, we expect these other signals to be small compared to the SZ flux for massive galaxy clusters. In this work, we take the first approach and fit the template to a Compton- y map created from a linear combination of 95 and 150 GHz maps. Effectively, we have used the different spectral dependence of the SZ and CMB to eliminate the CMB, and thus any correlation between the removed template and the lensing dipole in the CMB map.

We choose to use a radially symmetric template at the fixed cluster location in this work. Unless otherwise noted, we assume the beam to be a Gaussian with FWHM = 1' at 150 GHz and 1'.7 at 90 GHz. As this beam size is significantly large compared to the actual size of clusters at $z > 0.3$, clusters are approaching the effective point source limit where the specific details of their shape would not matter. Thus we choose to use a simple Gaussian template as the baseline template in this work. We also compare the results to template fitting with more physically motivated Arnaud profile (Arnaud et al., 2010), convolved by the experimental Gaussian beam. The residuals of removing a 2'.0 FWHM Gaussian from an Arnaud profile convolved by a 1'.7 beam are illustrated in Fig. 5.1. As argued above, the Gaussian significantly reduces the SZ signal despite the mismatch between the assumed profile and input SZ model. While there should be small variations in the typical size of the cluster’s SZ emission with mass and redshift, we neglect these variations and fix the size of the templates based on the expected median mass and redshift of the sample. One could easily adjust the template based on individual cluster redshift for a minimal increase in complexity.

As SZ and CMB have different frequency dependence, we use linear combination of 95 GHz and 150 GHz channels to obtain Compton- y maps. We then pull out a central $10' \times 10'$ cutout at the cluster location for fitting the template.

Since both the SZ emission and lensing signal extraction is concentrated within a few arcminutes of the cluster center, there is little reason to fit over a larger area. We allow for two free parameters in the fitting: the overall amplitude of the template, and a constant DC background level. While we include the DC term while fitting the template amplitude, we do not subtract DC level. Only the template is subtracted from the small-scale map.

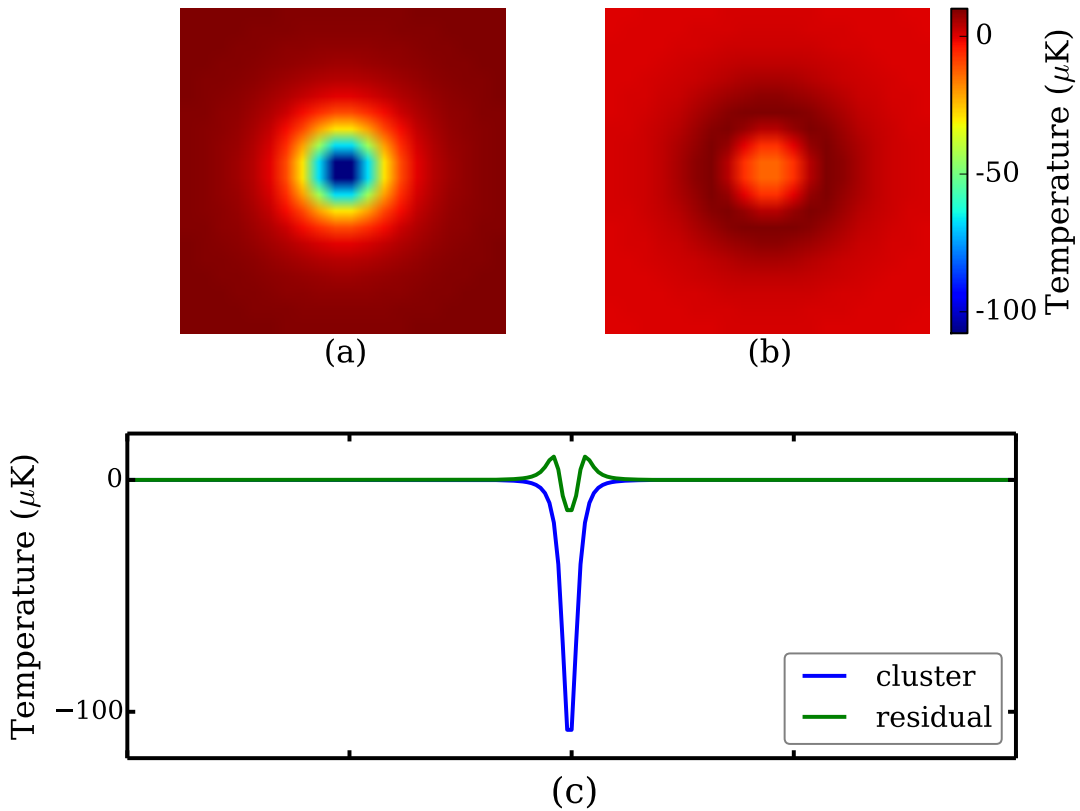


Figure 5.1: Template fitting significantly reduces SZ power, even with an imperfect match between the template and true SZ signal. The top left panel (a) shows the expected Arnaud profile for a galaxy cluster of mass $M_{200m} = 5 \times 10^{14} M_\odot$ at $z=0.7$ after being smoothed by Gaussian beam with FWHM = 1'.7. The top right panel (b) shows the residuals after subtracting the best-fit 2'.0 FWHM Gaussian (the amplitude is free, but the FWHM is fixed). The lower panel (c) shows one-dimensional slices through each panel: the solid, blue line is a slice through the beam-convolved Arnaud profile of (a), and the dashed green line is a slice through the residual map in (b).

With template fitting included, the Fourier transforms of the two maps used

by the quadratic estimator can be written down as:

$$G_\ell = i\ell W_\ell^G T_\ell^{\text{SZ-free}} \quad (5.1)$$

$$L_\ell = W_\ell^L (T_\ell - T_\ell^{\text{SZ-template}}) \quad (5.2)$$

where, G_ℓ is the large-scale gradient map and L_ℓ is the small-scale map. W_ℓ^G and W_ℓ^L are the Wiener filters to maximize the lensing signal Hu et al. (2007). The mm-wave map is T_ℓ while the constructed SZ-free map is $T_\ell^{\text{SZ-free}}$. Compared to the modified QE (Madhavacheril and Hill, 2018; Raghunathan et al., 2019a), the new element is the $T_\ell^{\text{SZ-template}}$ term representing the SZ template fit.

However the SZ emission in the small scale lensing map does add noise to the lensing reconstruction. Since under self-similarity the SZ flux, y , is expected to scale with cluster mass M as $y \propto M^{5/3}$ while the lensing signal is linear in mass, the additional SZ variance will generally be more important for high-mass clusters. The SZ variance will also be more important in low-noise surveys, i.e. when it is larger than the instrumental noise in the convergence map. Gravitational lensing of CMB by cluster induces a dipole kind of structure on the top of gradient. The correlation between the background gradient and lensing dipole is known as gradient approximation. The QE (Hu and Okamoto, 2002) exploits the gradient approximation to estimate the lensing convergence profile $\hat{\kappa}$. Gradient approximation doesn't hold for all Fourier modes, in fact it holds good for only those Fourier modes which are correlated by reconstruction. Specifically, the lensing convergence can be estimated from a weighted product of filtered versions of a gradient map $G(\hat{n})$ and small-scale lensing map $L(\hat{n})$:

$$\hat{\kappa}_\ell = -A_\ell \int d^2\hat{\mathbf{n}} e^{-i\hat{\mathbf{n}} \cdot \ell} \operatorname{Re}\{\nabla \cdot [G(\hat{\mathbf{n}}) L^*(\hat{\mathbf{n}})]\}. \quad (5.3)$$

Here, $\hat{\mathbf{n}}$ is the pointing unit vector, ℓ is angular multipole, and A_ℓ is a normalization factor.

While designed to pull out the lensing-induced correlations between large-scale and small-scale CMB anisotropy, the QE is also sensitive to correlations due to foreground emission. Of particular concern is the cluster's own SZ emission, which is typically an order of magnitude larger than lensing signal. Two ways have been discussed in literature to eliminate/reduce the SZ bias. One way is to exploit the multiple frequency dependence of SZ signal and use linear combination

of different frequencies to remove SZ. While this method completes eliminates SZ bias, it significantly increases the statistical uncertainty due to the higher noise level of the combined map. Another way is to lower the characteristic scale of the low pass filter on the gradient map as shown in Hu et al. (2007). Lowering the gradient cut results in separation of the modes present in gradient and small scale dipole map; hence reducing the unwanted correlation. However, a stronger low-pass filter obviously reduces the number of modes used to measure the gradient, and thus decreases the signal-to-noise.

On the other hand, the modified QE instead eliminates this bias without increasing the variance significantly by using an SZ-cleaned map for the large-scale gradient map. The large-scale gradient map is chosen because the CMB has much more power on large scales, so the noise penalty from SZ removal has minimal impact. Note that while multiple foregrounds can be removed in principle, in practice the focus has been on removing the SZ signal. This is simply because the SZ signal introduces the largest bias. With the SZ signal present in only one of the two maps, there is no SZ-induced correlation between the two maps and no net bias on the reconstruction of the lensing convergence.

5.1.2 Sources of uncertainty in the CMB-Cluster Lensing Measurement

Template fitting is intended to reduce the SZ variance, however it will do nothing for other sources of uncertainty such as instrumental noise, CMB sample variance and foreground emission (if not cleaned). Thus it will be useful to look at the relative magnitudes of these two terms, the SZ variance (σ_{SZ}^2) and the non-SZ variance (σ_κ^2), when interpreting the performance of template fitting in the next section.

The non-SZ variance depends on the survey parameters (i.e. instrumental noise, and the degree to which foregrounds are cleaned) but is independent of the cluster properties. We estimate the non-SZ variance, σ_κ^2 , using simulations of the CMB plus instrumental noise. Given the goal, we do not include the cluster's SZ emission. We apply the lensing pipeline to the simulated skies to estimate the convergence maps. We fit the convergence map to determine a mass, and take the scatter in these inferred masses over 1000 simulations to be σ_κ .

In contrast, the SZ variance should increase with cluster mass, M , roughly as $\sigma_{sz}^2 \propto M^{5/3}$, while being independent of the survey parameters. We estimate the

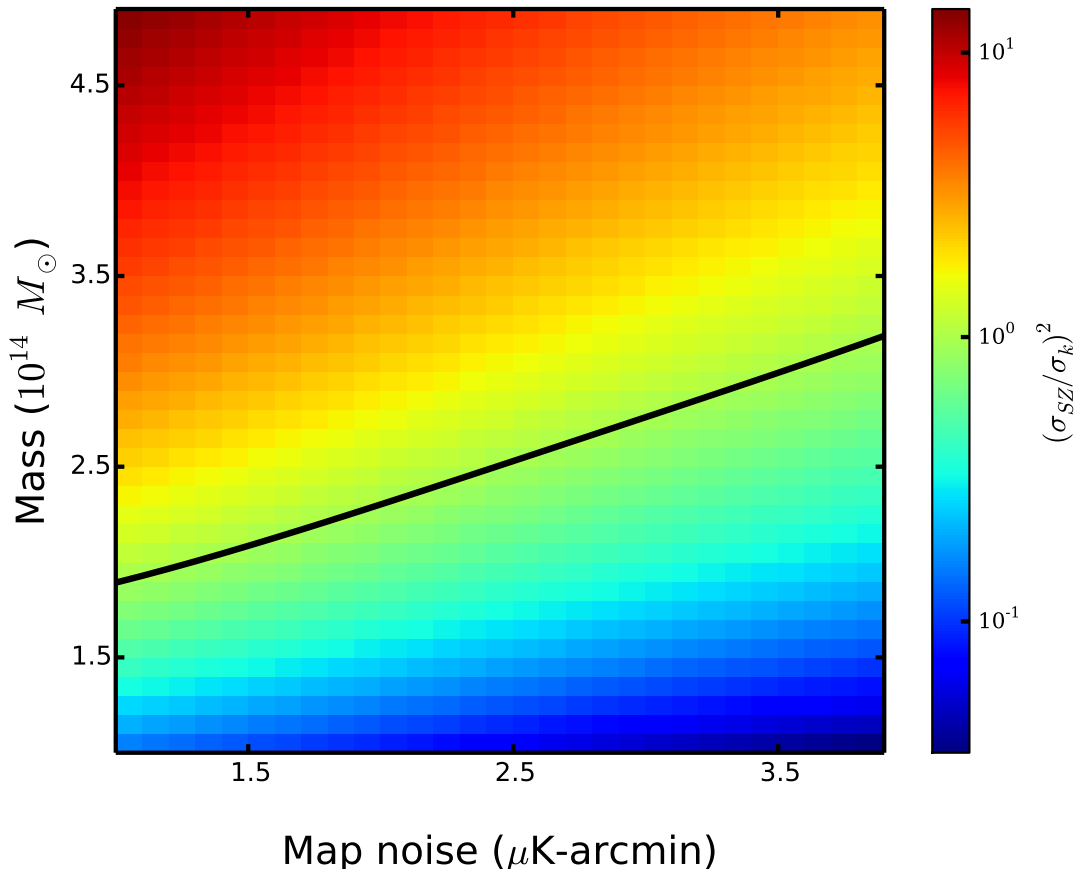


Figure 5.2: Ratio of SZ variance over kappa variance as a function of cluster mass and experimental noise level. As expected the ratio increases with mass for a given experimental noise level. The black solid line represents the points where the ratio SZ variance is equal to that of experimental noise.

SZ variance using the same suite of simulations, however now adding the cluster's SZ emission to the small-scale lensing map. We continue using an SZ-free map for other leg of the QE, the large-scale gradient map. As before, we estimate the convergence maps, fit for masses and take the scatter in these inferred masses to estimate $\sigma_{\text{SZ}}^2 + \sigma_{\kappa}^2$.

We present the ratio of the SZ to non-SZ variances, $\sigma_{\text{SZ}}^2/\sigma_{\kappa}^2$, as a function of survey noise level and cluster mass in Fig. 5.2. As expected, the ratio increases with mass at any given noise level. The black solid curve represents a ratio of unity when the SZ variance equals the non-SZ variance. We expect template fitting to significantly improve the mass uncertainties only for clusters above the black curve.

5.2 Results

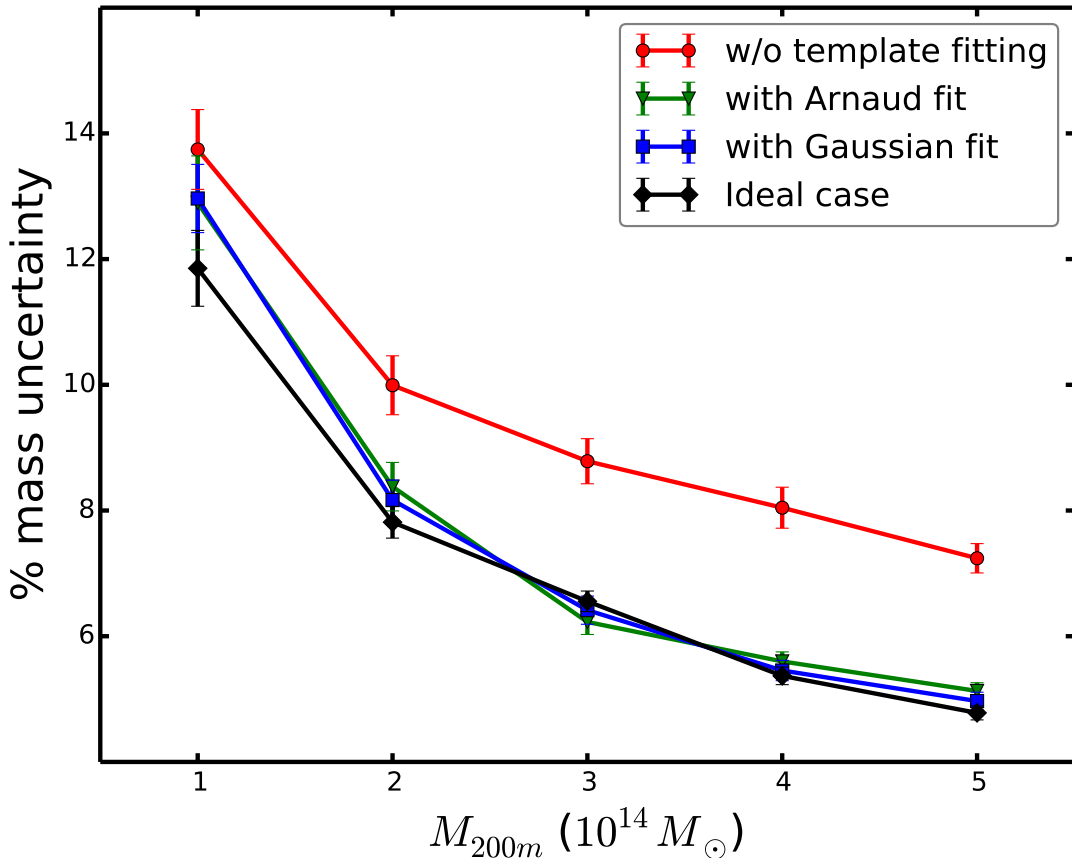


Figure 5.3: Projecting out an SZ template from the second leg of the modified QE improves the performance for all masses considered. Here we show the percentage mass uncertainties from three methods for a sample of 1000 clusters at a experimental noise level of $3 \mu\text{K}\text{-arcmin}$. All the curves use an SZ-free map for the gradient, but make different assumptions about the second, high-pass filtered map.

As shown in Fig. 5.3, we find that template fitting leads to a significant improvement in the final mass uncertainties for CMB-cluster lensing. For high-mass clusters, template fitting does nearly as well as in the idealized (non-physical) limit of having no SZ emission. In this figure, we are assuming an SPT-3G like experiment with FWHM of $1'$ and $1.7'$ at 150 GHz and 95 GHz respectively and a survey noise level of $3 \mu\text{K}\text{-arcmin}$. We compare four algorithms to estimate cluster masses. In all cases we use a SZ-free gradient map (from a linear combination of 95 and 150 GHz maps). First, the red solid line shows the performance

of the original modified QE without template fitting, where we have used SZ-free gradient map and 150GHz map with Arnaud SZ for the high pass filtered map. The second, black solid line shows the results for an idealized case, where we use a 150 GHz map without SZ for the high-pass filtered map. While this assumption is unphysical since there will be SZ emission at 150 GHz, it is useful as a representation of the performance limit for perfect SZ subtraction. Note that the relative performance improvement between the idealized and baseline case increases with mass as expected. For these survey parameters, the idealized case has 17% smaller uncertainties than the baseline for clusters of mass $1 \times 10^{14} M_{\odot}$ and 50% smaller for cluster masses of $5 \times 10^{14} M_{\odot}$. Template fitting recovers nearly all of this gain for high-mass clusters, as shown by the green triangles and blue squares (we have introduced an offset along mass axis for clarity). The two lines reflect different templates for subtraction. The green triangle shows the performance of projecting out an Arnaud SZ template from the small-scale map. The blue square shows the results when using a Gaussian template instead, which is slightly mismatched to the assumed SZ signal. There is no practical performance difference between the two templates. For these assumed survey parameters, both templates are essentially indistinguishable from the idealized perfect SZ removal case at masses above $2 \times 10^{14} M_{\odot}$. Template fitting does not do as well at lower masses. This can be understood by considering the zero-mass limit – where one tries to remove the SZ template from a map without SZ emission. The noisy estimate of the SZ template amplitude will set a non-zero, effective floor to the apparent SZ-like signal in this map. In the low-mass limit, SZ template removal will thus perform more poorly than the original estimator. The first signs of this transition can be seen in Fig. 5.3 when comparing the performance at $M_{200m} = 2 \times 10^{14} M_{\odot}$ to $1 \times 10^{14} M_{\odot}$.

5.2.1 Miscentering

Previous works have found a positional offset of 0.5' between the SZ and X-ray centroid (von der Linden et al., 2014) or location of the brightest central galaxy (BCG)(Song et al., 2012). Template fitting methods provides optimal results if cluster center is the SZ center. While this is not a problem for SZ selected clusters as both cluster and SZ center coincide, however, this may be a concern for clusters selected via X-ray or optical surveys. In such cases our new method will be optimal if we have additional fitting parameters for positional offsets. It

is important to note that in such cases we can't use high pass filtered map as the lensing induced "dipole" present in the HPF map biases our fitting to lower masses. This bias can be removed by combining different frequency channels to remove CMB with slight decrement in SNR.

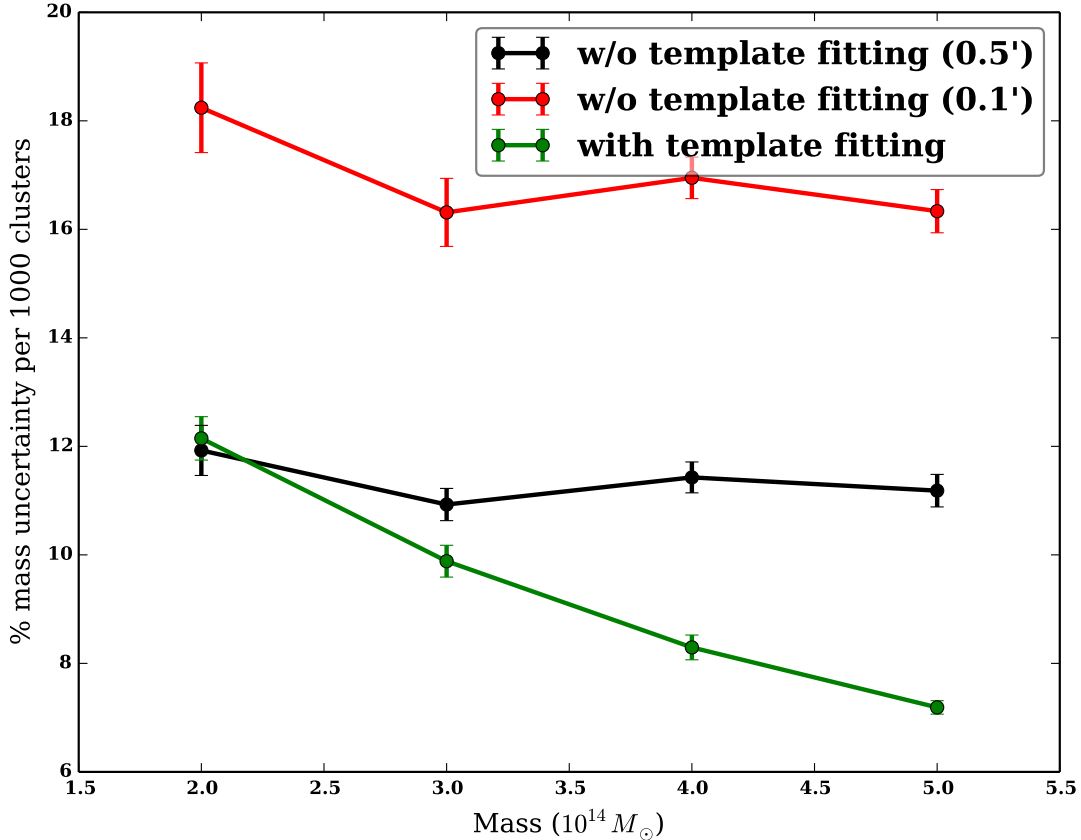


Figure 5.4: Our new method is robust to realistic SZ simulations. The red and black solid curves show the performance of modified QE for the Sehgal and Takahashi simulations respectively. The dashed lines show the improvement in each case when template fitting is used to reduce the SZ variance in the small-scale map. [SR: Change xlabel to M_{200m}].

5.2.2 Robustness of template fitting method

As shown in the last section, the refinement to the modified QE improves the fractional mass uncertainties significantly (above a mass threshold that depends on the survey noise) for the symmetric Arnaud profile. However, the question remains as to whether this improvement will continue with the more complex real SZ emission of galaxy clusters along with any other haloes along the line-of-sight.

To test this, we turn to the SZ simulations of Sehgal et al. (2010); Takahashi et al. (2017). As noted in §??, we draw SZ maps from these sims centered at the locations of similarly massed haloes. The results for these sims are shown in Fig. 5.5 for Gaussian template fitting. We have tested using both the Gaussian and Arnaud template fitting, and have found no appreciable difference. Red lines are for the Sehgal simulations and black lines for the Takahashi simulations. The solid lines are without template fitting, while the dashed lines show the improvement from template fitting in each case. The apparent flattening of the red curve is due the limited number of higher mass clusters in the Sehgal simulation. In this case of realistic SZ signals, however, we note that the performance is not equivalent to the idealized case presented as black solid curve in Fig. 5.3. This is due to the residual SZ signals in the map coming from the template mismatch and from adjacent haloes which we do not attempt to remove.

[ht]

5.3 Forecasts

We now consider the impact of this method on the performance of upcoming CMB surveys, SPT-3G (Bender et al., 2018), SO (The Simons Observatory Collaboration et al., 2019) and CMB-S4 (CMB-S4 Collaboration et al., 2016). For the latter two experiments, we only consider the large-aperture telescopes (LAT) with an experimental beam of $\theta_{\text{FWHM}} = 1.^{\circ}4$ at 150 GHz and covering 40% of the sky (see also Table ??). For SPT-3G, we assume a survey area of 1500 deg^2 and an experimental beam of $\theta_{\text{FWHM}} = 1.^{\circ}2$ at 150 GHz. We create a single cluster catalog realization for each experiment based on the noise levels at 150 GHz. Note that for simplicity, we make no attempt to use frequency information to remove other temperature foreground signals such as the the CIB, nor to improve the noise level on the Compton-y map. These assumptions are likely to mean that the simulated cluster list is conservative since we are not taking advantage of the multiple frequency bands in each of these experiments.

The three simulated cluster sample and assumed experimental parameters are passed through the cluster-lensing pipeline to estimate the mass uncertainty from CMB-cluster lensing on each stacked sample. For forecasts we picks SZ profiles from Takahashi et al. (2017) simulations and as mentioned before we randomly pick all the halos which fall within 5% of the desired mass and ± 0.2 of the desired redshift. The results are given in Table ???. We find that template fitting can

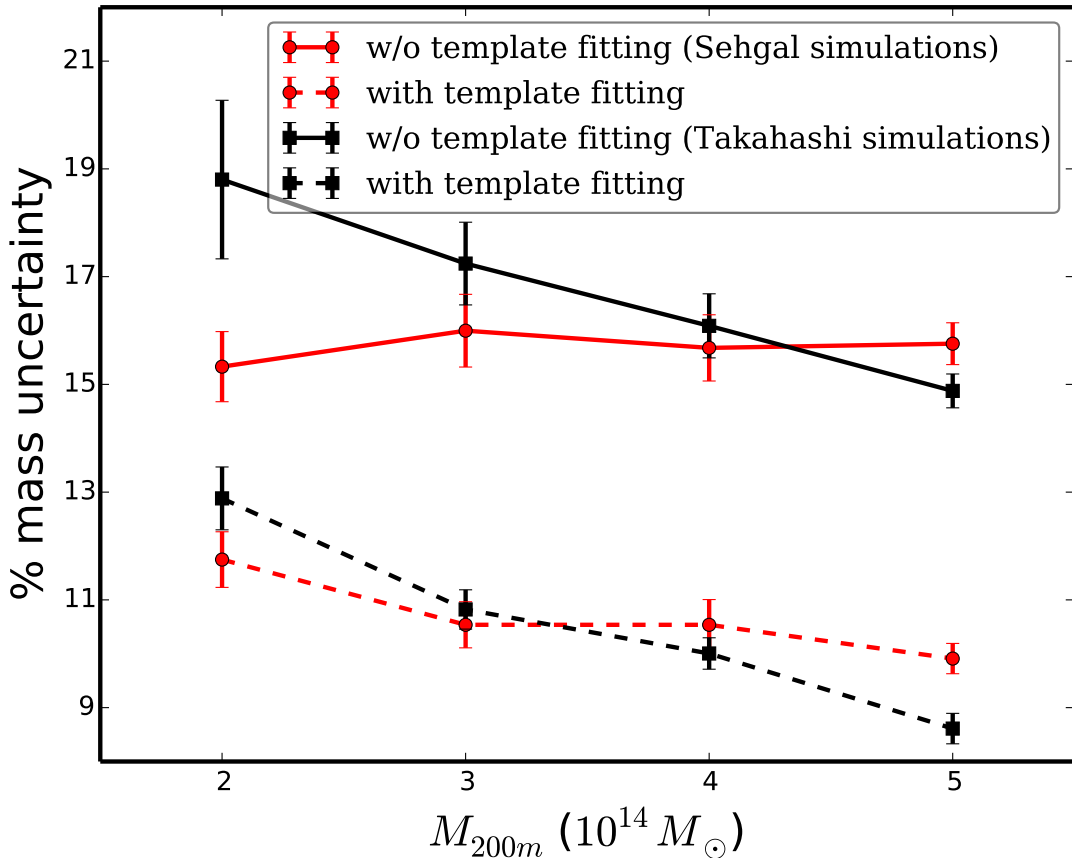


Figure 5.5: Our new method is robust to realistic SZ simulations. The red and black solid curves show the performance of modified QE for the Sehgal and Takahashi simulations respectively for a sample of 1000 clusters. The dashed lines show the improvement in each case when template fitting is used to reduce the SZ variance in the small-scale map. The plotted uncertainties are for a stack of 1000 galaxy clusters of the quoted mass at $z = 0.7$.

reduce the percentage mass uncertainty for SPT-3G, SO and CMB-S4 by 28%, 25% and 30% respectively.

5.4 Discussion and Conclusion

We have presented an improved version of the quadratic estimator (QE) to estimate galaxy cluster masses through CMB lensing. By projecting out an SZ template from the high-pass filtered leg of the QE, the algorithm substantially reduces the variance due to a cluster's own SZ emission. The SZ variance can be significant fraction of the total variance for high-mass clusters or low-noise surveys. Note that in the opposite limit of low masses or high noise (i.e. when

the SZ variance is negligible), this template fitting may slightly reduce the overall S/N.

While the performance of the template fitting does depend on the fidelity with which the template accurately represents the true SZ signal, these variations do not seem to be a significant issue. In part this is because upcoming CMB experiments will not have sufficient angular resolution to resolve most of the structure in the SZ emission; the instrumental beam at 150 GHz for a 6 m telescope is slightly larger than a typical high-redshift cluster. For mock SZ signals modeled using Arnaud profile, we find that the template removal approach reduces all of the additional variance due to the SZ signal. The improvement is not 100% for realistic SZ signals (Sehgal et al., 2010; Takahashi et al., 2017) because of the SZ emission from the adjacent haloes along the line-of-sight that we do not attempt to remove.

The method presented in this work is not limited to the small-scale lensing. For example, Madhavacheril and Hill (2018) demonstrated that the modified QE can also be employed to CMB lensing in general. However, as shown here the thermal SZ signal from clusters detected at high S/N adds extra variance in the reconstructed lensing maps. By using template fitting approach we reduced the variance significantly. In future CMB lensing work, we can use the template fitting approach instead of masking the massive galaxy clusters.

CMB-cluster lensing will be a key tool for galaxy cluster cosmology at high redshifts, while also providing a cross-check of optical weak lensing mass estimates at lower redshifts. For future surveys like CMB-S4 and Simons Observatory and for clusters above masses of $4 \times 10^{14} M_{\odot}$, we find that template fitting yields a factor of 1.4 reduction in the mass uncertainties. These results will help us in the quest to understand dark energy and the accelerating expansion of the Universe.

Bibliography

- M. Arnaud, G. W. Pratt, R. Piffaretti, H. Bohringer, J. H. Croston, and E. Pointecouteau. The universal galaxy cluster pressure profile from a representative sample of nearby systems (REXCESS) and the Y_{SZ} - M_{500} relation. *A&A*, 517:A92+, July 2010. doi: 10.1051/0004-6361/200913416.
- J. E. Austermann, K. A. Aird, J. A. Beall, D. Becker, A. Bender, B. A. Benson, L. E. Bleem, J. Britton, J. E. Carlstrom, C. L. Chang, H. C. Chiang, H.-M. Cho, T. M. Crawford, A. T. Crites, A. Datesman, T. de Haan, M. A. Dobbs, E. M. George, N. W. Halverson, N. Harrington, J. W. Henning, G. C. Hilton, G. P. Holder, W. L. Holzapfel, S. Hoover, N. Huang, J. Hubmayr, K. D. Irwin, R. Keisler, J. Kennedy, L. Knox, A. T. Lee, E. Leitch, D. Li, M. Lueker, D. P. Marrone, J. J. McMahon, J. Mehl, S. S. Meyer, T. E. Montroy, T. Natoli, J. P. Nibarger, M. D. Niemack, V. Novosad, S. Padin, C. Pryke, C. L. Reichardt, J. E. Ruhl, B. R. Saliwanchik, J. T. Sayre, K. K. Schaffer, E. Shirokoff, A. A. Stark, K. Story, K. Vanderlinde, J. D. Vieira, G. Wang, R. Williamson, V. Yefremenko, K. W. Yoon, and O. Zahn. SPTpol: an instrument for CMB polarization measurements with the South Pole Telescope. In *Society of Photo-Optical Instrumentation Engineers (SPIE) Conference Series*, volume 8452, September 2012. doi: 10.1117/12.927286.
- M. Bartelmann. Arcs from a universal dark-matter halo profile. *A&A*, 313:697–702, September 1996.
- N. Battaglia. The tau of galaxy clusters. *JCAP*, 2016(8):058, Aug 2016. doi: 10.1088/1475-7516/2016/08/058.
- E. J. Baxter, R. Keisler, S. Dodelson, K. A. Aird, S. W. Allen, M. L. N. Ashby, M. Bautz, M. Bayliss, B. A. Benson, L. E. Bleem, S. Bocquet, M. Brodwin, J. E. Carlstrom, C. L. Chang, I. Chiu, H.-M. Cho, A. Clocchiatti, T. M. Crawford, A. T. Crites, S. Desai, J. P. Dietrich, T. de Haan, M. A. Dobbs, R. J. Foley, W. R. Forman, E. M. George, M. D. Gladders, A. H. Gonzalez, N. W. Halverson, N. L. Harrington, C. Hennig, H. Hoekstra, G. P. Holder, W. L. Holzapfel, Z. Hou, J. D. Hrubes, C. Jones, L. Knox, A. T. Lee, E. M. Leitch, J. Liu, M. Lueker, D. Luong-Van, A. Mantz, D. P. Marrone,

- M. McDonald, J. J. McMahon, S. S. Meyer, M. Millea, L. M. Mocanu, S. S. Murray, S. Padin, C. Pryke, C. L. Reichardt, A. Rest, J. E. Ruhl, B. R. Saliwanchik, A. Saro, J. T. Sayre, K. K. Schaffer, E. Shirokoff, J. Song, H. G. Spieler, B. Stalder, S. A. Stanford, Z. Staniszewski, A. A. Stark, K. T. Story, A. van Engelen, K. Vanderlinde, J. D. Vieira, A. Vikhlinin, R. Williamson, O. Zahn, and A. Zenteno. A Measurement of Gravitational Lensing of the Cosmic Microwave Background by Galaxy Clusters Using Data from the South Pole Telescope. *ApJ*, 806:247, June 2015. doi: 10.1088/0004-637X/806/2/247.
- E. J. Baxter, S. Raghunathan, T. M. Crawford, P. Fosalba, Z. Hou, G. P. Holder, Y. Omori, S. Patil, E. Rozo, T. M. C. Abbott, J. Annis, K. Aylor, A. Benoit-Lévy, B. A. Benson, E. Bertin, L. Bleem, E. Buckley-Geer, D. L. Burke, J. Carlstrom, A. Carnero Rosell, M. Carrasco Kind, J. Carretero, C. L. Chang, H.-M. Cho, A. T. Crites, M. Crocce, C. E. Cunha, L. N. da Costa, C. B. D’Andrea, C. Davis, T. de Haan, S. Desai, J. P. Dietrich, M. A. Dobbs, S. Dodelson, P. Doel, A. Drlica-Wagner, J. Estrada, W. B. Everett, A. Fausti Neto, B. Flaugher, J. Frieman, J. García-Bellido, E. M. George, E. Gaztanaga, T. Giannantonio, D. Gruen, R. A. Gruendl, J. Gschwend, G. Gutierrez, N. W. Halverson, N. L. Harrington, W. G. Hartley, W. L. Holzapfel, K. Honscheid, J. D. Hrubes, B. Jain, D. J. James, M. Jarvis, T. Jeltema, L. Knox, E. Krause, K. Kuehn, S. Kuhlmann, N. Kuropatkin, O. Lahav, A. T. Lee, E. M. Leitch, T. S. Li, M. Lima, D. Luong-Van, A. Manzotti, M. March, D. P. Marrone, J. L. Marshall, P. Martini, J. J. McMahon, P. Melchior, F. Menanteau, S. S. Meyer, C. J. Miller, R. Miquel, L. M. Mocanu, J. J. Mohr, T. Natoli, B. Nord, R. L. C. Ogando, S. Padin, A. A. Plazas, C. Pryke, D. Rapetti, C. L. Reichardt, A. K. Romer, A. Roodman, J. E. Ruhl, E. Rykoff, M. Sako, E. Sanchez, J. T. Sayre, V. Scarpine, K. K. Schaffer, R. Schindler, M. Schubnell, I. Sevilla-Noarbe, E. Shirokoff, M. Smith, R. C. Smith, M. Soares-Santos, F. Sobreira, Z. Staniszewski, A. Stark, K. Story, E. Suchyta, G. Tarle, D. Thomas, M. A. Troxel, K. Vanderlinde, J. D. Vieira, A. R. Walker, R. Williamson, Y. Zhang, and J. Zuntz. A Measurement of CMB Cluster Lensing with SPT and DES Year 1 Data. *MNRAS*, February 2018. doi: 10.1093/mnras/sty305.
- A. N. Bender, P. A. R. Ade, Z. Ahmed, A. J. Anderson, J. S. Avva, K. Aylor, P. S. Barry, R. Basu Thakur, B. A. Benson, L. S. Bleem, S. Bocquet, K. Byrum, J. E. Carlstrom, F. W. Carter, T. W. Cecil, C. L. Chang, H. M. Cho, J. F. Cliche, T. M. Crawford, A. Cukierman, T. de Haan, E. V. Denison, J. Ding, M. A. Dobbs, S. Dodelson, D. Dutcher, W. Everett, A. Foster, J. Gallicchio, A. Gilbert, J. C. Groh, S. T. Guns, N. W. Halverson, A. H. Harke-Hosemann, N. L. Harrington, J. W. Henning, G. C. Hilton, G. P. Holder, W. L. Holzapfel, N. Huang, K. D. Irwin, O. B.

- Jeong, M. Jonas, A. Jones, T. S. Khaire, L. Knox, A. M. Kofman, M. Korman, D. L. Kubik, S. Kuhlmann, C. L. Kuo, A. T. Lee, E. M. Leitch, A. E. Lowitz, S. S. Meyer, D. Michalik, J. Montgomery, A. Nadolski, T. Natoli, H. Nguyen, G. I. Noble, V. Novosad, S. Padin, Z. Pan, J. Pearson, C. M. Posada, W. Quan, S. Raghunathan, A. Rahlin, C. L. Reichardt, J. E. Ruhl, J. T. Sayre, E. Shirokoff, G. Smecher, J. A. Sobrin, A. A. Stark, K. T. Story, A. Suzuki, K. L. Thompson, C. Tucker, L. R. Vale, K. Vanderlinde, J. D. Vieira, G. Wang, N. Whitehorn, W. L. K. Wu, V. Yefremenko, K. W. Yoon, and M. R. Young. Year two instrument status of the SPT-3G cosmic microwave background receiver. In *Millimeter, Submillimeter, and Far-Infrared Detectors and Instrumentation for Astronomy IX*, volume 10708 of *Society of Photo-Optical Instrumentation Engineers (SPIE) Conference Series*, page 1070803, Jul 2018. doi: 10.1117/12.2312426.
- B. A. Benson, P. A. R. Ade, Z. Ahmed, S. W. Allen, K. Arnold, J. E. Austermann, A. N. Bender, L. E. Bleem, J. E. Carlstrom, C. L. Chang, H. M. Cho, J. F. Cliche, T. M. Crawford, A. Cukierman, T. de Haan, M. A. Dobbs, D. Dutcher, W. Everett, A. Gilbert, N. W. Halverson, D. Hanson, N. L. Harrington, K. Hattori, J. W. Henning, G. C. Hilton, G. P. Holder, W. L. Holzapfel, K. D. Irwin, R. Keisler, L. Knox, D. Kubik, C. L. Kuo, A. T. Lee, E. M. Leitch, D. Li, M. McDonald, S. S. Meyer, J. Montgomery, M. Myers, T. Natoli, H. Nguyen, V. Novosad, S. Padin, Z. Pan, J. Pearson, C. Reichardt, J. E. Ruhl, B. R. Saliwanchik, G. Simard, G. Smecher, J. T. Sayre, E. Shirokoff, A. A. Stark, K. Story, A. Suzuki, K. L. Thompson, C. Tucker, K. Vanderlinde, J. D. Vieira, A. Vikhlinin, G. Wang, V. Yefremenko, and K. W. Yoon. SPT-3G: a next-generation cosmic microwave background polarization experiment on the South Pole telescope. In *Society of Photo-Optical Instrumentation Engineers (SPIE) Conference Series*, volume 9153 of *Society of Photo-Optical Instrumentation Engineers (SPIE) Conference Series*, page 1, July 2014. doi: 10.1117/12.2057305.
- Suman Bhattacharya, Salman Habib, Katrin Heitmann, and Alexey Vikhlinin. Dark Matter Halo Profiles of Massive Clusters: Theory versus Observations. *ApJ*, 766(1):32, Mar 2013. doi: 10.1088/0004-637X/766/1/32.
- L. E. Bleem, B. Stalder, M. Brodwin, M. T. Busha, M. D. Gladders, F. W. High, A. Rest, and R. H. Wechsler. A New Reduction of the Blanco Cosmology Survey: An Optically Selected Galaxy Cluster Catalog and a Public Release of Optical Data Products. *ApJS*, 216:20, January 2015. doi: 10.1088/0067-0049/216/1/20.
- M. R. Calabretta and E. W. Greisen. Representations of celestial coordinates in FITS. *A&A*, 395:1077–1122, December 2002. doi: 10.1051/0004-6361:20021327.
- Jean-François Cardoso, Maude Le Jeune, Jacques Delabrouille, Marc Betoule, and Guil-

- laume Patanchon. Component Separation With Flexible Models—Application to Multichannel Astrophysical Observations. *IEEE Journal of Selected Topics in Signal Processing*, 2(5):735–746, Nov 2008. doi: 10.1109/JSTSP.2008.2005346.
- J. E. Carlstrom, P. A. R. Ade, K. A. Aird, B. A. Benson, L. E. Bleem, S. Busetti, C. L. Chang, E. Chauvin, H.-M. Cho, T. M. Crawford, A. T. Crites, M. A. Dobbs, N. W. Halverson, S. Heimsath, W. L. Holzapfel, J. D. Hrubes, M. Joy, R. Keisler, T. M. Lanting, A. T. Lee, E. M. Leitch, J. Leong, W. Lu, M. Lueker, D. Luong-van, J. J. McMahon, J. Mehl, S. S. Meyer, J. J. Mohr, T. E. Montroy, S. Padin, T. Plagge, C. Pryke, J. E. Ruhl, K. K. Schaffer, D. Schwan, E. Shirokoff, H. G. Spieler, Z. Staniszewski, A. A. Stark, C. Tucker, K. Vanderlinde, J. D. Vieira, and R. Williamson. The 10 Meter South Pole Telescope. *PASP*, 123:568–581, May 2011. doi: 10.1086/659879.
- Tzu-Ching Chang, Ue-Li Pen, Jeffrey B. Peterson, and Patrick McDonald. Baryon Acoustic Oscillation Intensity Mapping of Dark Energy. *PRL*, 100(9):091303, Mar 2008. doi: 10.1103/PhysRevLett.100.091303.
- Hillary L. Child, Salman Habib, Katrin Heitmann, Nicholas Frontiere, Hal Finkel, Adrian Pope, and Vitali Morozov. Halo Profiles and the Concentration-Mass Relation for a Λ CDM Universe. *ApJ*, 859(1):55, May 2018. doi: 10.3847/1538-4357/aabf95.
- CMB-S4 Collaboration, K. N. Abazajian, P. Adshead, Z. Ahmed, S. W. Allen, D. Alonso, K. S. Arnold, C. Baccigalupi, J. G. Bartlett, N. Battaglia, B. A. Benson, C. A. Bischoff, J. Borrill, V. Buza, E. Calabrese, R. Caldwell, J. E. Carlstrom, C. L. Chang, T. M. Crawford, F.-Y. Cyr-Racine, F. De Bernardis, T. de Haan, S. di Serego Alighieri, J. Dunkley, C. Dvorkin, J. Errard, G. Fabbian, S. Feeney, S. Ferraro, J. P. Filippini, R. Flauger, G. M. Fuller, V. Gluscevic, D. Green, D. Grin, E. Grohs, J. W. Henning, J. C. Hill, R. Hlozek, G. Holder, W. Holzapfel, W. Hu, K. M. Huffenberger, R. Keskitalo, L. Knox, A. Kosowsky, J. Kovac, E. D. Kovetz, C.-L. Kuo, A. Kusaka, M. Le Jeune, A. T. Lee, M. Lilley, M. Loverde, M. S. Madhavacheril, A. Mantz, D. J. E. Marsh, J. McMahon, P. D. Meerburg, J. Meyers, A. D. Miller, J. B. Munoz, H. N. Nguyen, M. D. Niemack, M. Peloso, J. Peloton, L. Pogosian, C. Pryke, M. Raveri, C. L. Reichardt, G. Rocha, A. Rotti, E. Schaan, M. M. Schmitfull, D. Scott, N. Sehgal, S. Shandera, B. D. Sherwin, T. L. Smith, L. Sorbo, G. D. Starkman, K. T. Story, A. van Engelen, J. D. Vieira, S. Watson, N. Whitehorn, and W. L. Kimmy Wu. CMB-S4 Science Book, First Edition. *ArXiv e-prints*, October 2016.
- Ryan J. Cooke, Max Pettini, Kenneth M. Nollett, and Regina Jorgenson. The Primordial Deuterium Abundance of the Most Metal-poor Damped Lyman- α System. *ApJ*,

- 830(2):148, Oct 2016. doi: 10.3847/0004-637X/830/2/148.
- B. Diemer and A. V. Kravtsov. Dependence of the Outer Density Profiles of Halos on Their Mass Accretion Rate. *ApJ*, 789:1, July 2014. doi: 10.1088/0004-637X/789/1/1.
- S. Dodelson. *Modern Cosmology*. Academic Press, 2003.
- S. Dodelson. CMB-cluster lensing. *PRD*, 70(2):023009, July 2004. doi: 10.1103/PhysRevD.70.023009.
- A. Drlica-Wagner, I. Sevilla-Noarbe, E. S. Rykoff, R. A. Gruendl, B. Yanny, D. L. Tucker, B. Hoyle, A. Carnero Rosell, G. M. Bernstein, K. Bechtol, M. R. Becker, A. Benoit-Lévy, E. Bertin, M. Carrasco Kind, C. Davis, J. de Vicente, H. T. Diehl, D. Gruen, W. G. Hartley, B. Leistedt, T. S. Li, J. L. Marshall, E. Neilson, M. M. Rau, E. Sheldon, J. Smith, M. A. Troxel, S. Wyatt, Y. Zhang, T. M. C. Abbott, F. B. Abdalla, S. Allam, M. Banerji, D. Brooks, E. Buckley-Geer, D. L. Burke, D. Capozzi, J. Carretero, C. E. Cunha, C. B. D'Andrea, L. N. da Costa, D. L. DePoy, S. Desai, J. P. Dietrich, P. Doel, A. E. Evrard, A. Fausti Neto, B. Flaugher, P. Fosalba, J. Frieman, J. García-Bellido, D. W. Gerdes, T. Giannantonio, J. Gschwend, G. Gutierrez, K. Honscheid, D. J. James, T. Jeltema, K. Kuehn, S. Kuhlmann, N. Kuropatkin, O. Lahav, M. Lima, H. Lin, M. A. G. Maia, P. Martini, R. G. McMahon, P. Melchior, F. Menanteau, R. Miquel, R. C. Nichol, R. L. C. Ogando, A. A. Plazas, A. K. Romer, A. Roodman, E. Sanchez, V. Scarpine, R. Schindler, M. Schubnell, M. Smith, R. C. Smith, M. Soares-Santos, F. Sobreira, E. Suchyta, G. Tarle, V. Vikram, A. R. Walker, R. H. Wechsler, J. Zuntz, and DES Collaboration. Dark Energy Survey Year 1 Results: The Photometric Data Set for Cosmology. *ApJS*, 235:33, April 2018. doi: 10.3847/1538-4365/aab4f5.
- A. R. Duffy, J. Schaye, S. T. Kay, and C. Dalla Vecchia. Dark matter halo concentrations in the Wilkinson Microwave Anisotropy Probe year 5 cosmology. *MNRAS*, 390:L64–L68, October 2008. doi: 10.1111/j.1745-3933.2008.00537.x.
- J Dunkley, E Calabrese, J Sievers, G.E Addison, N Battaglia, E.S Battistelli, J.R Bond, S Das, M.JDevlin, R DÃijnner, J.W Fowler, M Gralla, A Hajian, M Halpern, M Hasselfield, A.D Hincks, R Hlozek, J.P Hughes andK.D Irwin, A Kosowsky, T Louis, T.A Marriage, D Marsden, F Menanteau, K Moodley, M Niemack, M.R Nolta, L.A Page, B Partridge, N Sehgal, D.N Spergel, S.T Staggs, E.R Switzer, H Trac, and E Wollack. The atacama cosmology telescope: likelihood for small-scale CMB data. *Journal of Cosmology and Astroparticle Physics*, 2013(07):025–025, jul 2013. doi: 10.1088/1475-7516/2013/07/025. URL <https://doi.org/10.1088%2F1475-7516%2F2013%2F07%2F025>.
- J. Einasto and U. Haud. Galactic models with massive corona. I - Method. II - Galaxy.

- A&A*, 223:89–106, October 1989.
- D. J. Fixsen, E. S. Cheng, J. M. Gales, J. C. Mather, R. A. Shafer, and E. L. Wright. The Cosmic Microwave Background Spectrum from the Full COBE FIRAS Data Set. *ApJ*, 473:576, December 1996. URL http://adsabs.harvard.edu/cgi-bin/nph-bib_query?bibcode=1996ApJ...473..576F&db_key=AST.
- B. Flaugher, H. T. Diehl, K. Honscheid, T. M. C. Abbott, O. Alvarez, R. Angstadt, J. T. Annis, M. Antonik, O. Ballester, L. Beaufore, G. M. Bernstein, R. A. Bernstein, B. Bigelow, M. Bonati, D. Boprie, D. Brooks, E. J. Buckley-Geer, J. Campa, L. Cardiel-Sas, F. J. Castander, J. Castilla, H. Cease, J. M. Cela-Ruiz, S. Chappa, E. Chi, C. Cooper, L. N. da Costa, E. Dede, G. Derylo, D. L. DePoy, J. de Vicente, P. Doel, A. Drlica-Wagner, J. Eiting, A. E. Elliott, J. Emes, J. Estrada, A. Fausti Neto, D. A. Finley, R. Flores, J. Frieman, D. Gerdes, M. D. Gladders, B. Gregory, G. R. Gutierrez, J. Hao, S. E. Holland, S. Holm, D. Huffman, C. Jackson, D. J. James, M. Jonas, A. Karcher, I. Karliner, S. Kent, R. Kessler, M. Kozlovsky, R. G. Kron, D. Kubik, K. Kuehn, S. Kuhlmann, K. Kuk, O. Lahav, A. Lathrop, J. Lee, M. E. Levi, P. Lewis, T. S. Li, I. Mandrichenko, J. L. Marshall, G. Martinez, K. W. Merritt, R. Miquel, F. Muñoz, E. H. Neilsen, R. C. Nichol, B. Nord, R. Ogando, J. Olsen, N. Palaio, K. Patton, J. Peoples, A. A. Plazas, J. Rauch, K. Reil, J.-P. Rheault, N. A. Roe, H. Rogers, A. Roodman, E. Sanchez, V. Scarpine, R. H. Schindler, R. Schmidt, R. Schmitt, M. Schubnell, K. Schultz, P. Schurter, L. Scott, S. Serrano, T. M. Shaw, R. C. Smith, M. Soares-Santos, A. Stefanik, W. Stuermer, E. Suchyta, A. Sypniewski, G. Tarle, J. Thaler, R. Tighe, C. Tran, D. Tucker, A. R. Walker, G. Wang, M. Watson, C. Weaverdyck, W. Wester, R. Woods, B. Yanny, and DES Collaboration. The Dark Energy Camera. *Astrophysical Journal*, 150:150, November 2015. doi: 10.1088/0004-6256/150/5/150.
- Samuel Flender, Lindsey Bleem, Hal Finkel, Salman Habib, Katrin Heitmann, and Gilbert Holder. Simulations of the Pairwise Kinematic Sunyaev-Zel'dovich Signal. *ApJ*, 823(2):98, Jun 2016. doi: 10.3847/0004-637X/823/2/98.
- D. Foreman-Mackey, D. W. Hogg, D. Lang, and J. Goodman. emcee: The MCMC Hammer. *PASP*, 125:306, March 2013. doi: 10.1086/670067.
- J. E. Geach and J. A. Peacock. Cluster richness-mass calibration with cosmic microwave background lensing. *Nature Astronomy*, 1:795–799, November 2017. doi: 10.1038/s41550-017-0259-1.
- E. M. George, C. L. Reichardt, K. A. Aird, B. A. Benson, L. E. Bleem, J. E. Carlstrom, C. L. Chang, H. M. Cho, T. M. Crawford, A. T. Crites, T. de Haan, M. A. Dobbs, J. Dudley, N. W. Halverson, N. L. Harrington, G. P. Holder, W. L. Holzapfel, Z. Hou,

- J. D. Hrubes, R. Keisler, L. Knox, A. T. Lee, E. M. Leitch, M. Lueker, D. Luong-Van, J. J. McMahon, J. Mehl, S. S. Meyer, M. Millea, L. M. Mocanu, J. J. Mohr, T. E. Montroy, S. Padin, T. Plagge, C. Pryke, J. E. Ruhl, K. K. Schaffer, L. Shaw, E. Shirokoff, H. G. Spieler, Z. Staniszewski, A. A. Stark, K. T. Story, A. van Engelen, K. Vanderlinde, J. D. Vieira, R. Williamson, and O. Zahn. A Measurement of Secondary Cosmic Microwave Background Anisotropies from the 2500 Square-degree SPT-SZ Survey. *ApJ*, 799(2):177, Feb 2015. doi: 10.1088/0004-637X/799/2/177.
- K. M. Górski, E. Hivon, A. J. Banday, B. D. Wandelt, F. K. Hansen, M. Reinecke, and M. Bartelmann. HEALPix: A Framework for High-Resolution Discretization and Fast Analysis of Data Distributed on the Sphere. *ApJ*, 622:759–771, April 2005. doi: 10.1086/427976.
- Laura Grego, John E. Carlstrom, Erik D. Reese, Gilbert P. Holder, William L. Holzapfel, Marshall K. Joy, Joseph J. Mohr, and Sandeep Patel. Galaxy Cluster Gas Mass Fractions from Sunyaev-Zeldovich Effect Measurements: Constraints on Ω_M . *ApJ*, 552(1):2–14, May 2001. doi: 10.1086/320443.
- J. Hartlap, P. Simon, and P. Schneider. Why your model parameter confidences might be too optimistic. Unbiased estimation of the inverse covariance matrix. *A&A*, 464: 399–404, March 2007. doi: 10.1051/0004-6361:20066170.
- M. Hasselfield, M. Hilton, T. A. Marriage, G. E. Addison, L. F. Barrientos, N. Battaglia, E. S. Battistelli, J. R. Bond, D. Crichton, S. Das, M. J. Devlin, S. R. Dicker, J. Dunkley, R. Dünner, J. W. Fowler, M. B. Gralla, A. Hajian, M. Halpern, A. D. Hincks, R. Hložek, J. P. Hughes, L. Infante, K. D. Irwin, A. Kosowsky, D. Marsden, F. Menanteau, K. Moodley, M. D. Niemack, M. R. Nolta, L. A. Page, B. Partridge, E. D. Reese, B. L. Schmitt, N. Sehgal, B. D. Sherwin, J. Sievers, C. Sifón, D. N. Spergel, S. T. Staggs, D. S. Swetz, E. R. Switzer, R. Thornton, H. Trac, and E. J. Wollack. The Atacama Cosmology Telescope: Sunyaev-Zel'dovich selected galaxy clusters at 148 GHz from three seasons of data. *JCAP*, 7:008, July 2013. doi: 10.1088/1475-7516/2013/07/008.
- S. W. Henderson, R. Allison, J. Austermann, T. Baildon, N. Battaglia, J. A. Beall, D. Becker, F. De Bernardis, J. R. Bond, E. Calabrese, S. K. Choi, K. P. Coughlin, K. T. Crowley, R. Datta, M. J. Devlin, S. M. Duff, J. Dunkley, R. Dünner, A. van Engelen, P. A. Gallardo, E. Grace, M. Hasselfield, F. Hills, G. C. Hilton, A. D. Hincks, R. Hložek, S. P. Ho, J. Hubmayr, K. Huffenberger, J. P. Hughes, K. D. Irwin, B. J. Koopman, A. B. Kosowsky, D. Li, J. McMahon, C. Munson, F. Nati, L. Newburgh, M. D. Niemack, P. Niraula, L. A. Page, C. G. Pappas, M. Salatino, A. Schillaci, B. L. Schmitt, N. Sehgal, B. D. Sherwin, J. L. Sievers, S. M. Simon, D. N.

- Spergel, S. T. Staggs, J. R. Stevens, R. Thornton, J. Van Lanen, E. M. Vavagiakis, J. T. Ward, and E. J. Wollack. Advanced ACTPol Cryogenic Detector Arrays and Readout. *Journal of Low Temperature Physics*, 184:772–779, August 2016. doi: 10.1007/s10909-016-1575-z.
- J. W. Henning, J. T. Sayre, C. L. Reichardt, P. A. R. Ade, A. J. Anderson, J. E. Austermann, J. A. Beall, A. N. Bender, B. A. Benson, L. E. Bleem, J. E. Carlstrom, C. L. Chang, H. C. Chiang, H.-M. Cho, R. Citron, C. Corbett Moran, T. M. Crawford, A. T. Crites, T. de Haan, M. A. Dobbs, W. Everett, J. Gallicchio, E. M. George, A. Gilbert, N. W. Halverson, N. Harrington, G. C. Hilton, G. P. Holder, W. L. Holzapfel, S. Hoover, Z. Hou, J. D. Hrubes, N. Huang, J. Hubmayr, K. D. Irwin, R. Keisler, L. Knox, A. T. Lee, E. M. Leitch, D. Li, A. Lowitz, A. Manzotti, J. J. McMahon, S. S. Meyer, L. Mocanu, J. Montgomery, A. Nadolski, T. Natoli, J. P. Nibarger, V. Novosad, S. Padin, C. Pryke, J. E. Ruhl, B. R. Saliwanchik, K. K. Schaffer, C. Sievers, G. Smecher, A. A. Stark, K. T. Story, C. Tucker, K. Vanderlinde, T. Veach, J. D. Vieira, G. Wang, N. Whitehorn, W. L. K. Wu, and V. Yefremenko. Measurements of the Temperature and E-mode Polarization of the CMB from 500 Square Degrees of SPTpol Data. *ApJ*, 852:97, January 2018. doi: 10.3847/1538-4357/aa9ff4.
- Benjamin Horowitz, Simone Ferraro, and Blake D. Sherwin. Reconstructing small-scale lenses from the cosmic microwave background temperature fluctuations. *MNRAS*, 485(3):3919–3929, May 2019. doi: 10.1093/mnras/stz566.
- W. Hu and M. White. A CMB polarization primer. *New Astronomy*, 2:323–344, 1997. astro-ph/9706147.
- W. Hu, S. DeDeo, and C. Vale. Cluster mass estimators from CMB temperature and polarization lensing. *New Journal of Physics*, 9:441–+, December 2007. doi: 10.1088/1367-2630/9/12/441.
- Wayne Hu and Takemi Okamoto. Mass reconstruction with cmb polarization. *Astrophys.J.*, 574:566–574, 2002. doi: 10.1086/341110.
- Edwin Hubble. A Relation between Distance and Radial Velocity among Extra-Galactic Nebulae. *Proceedings of the National Academy of Science*, 15(3):168–173, Mar 1929. doi: 10.1073/pnas.15.3.168.
- A. Jenkins, C. S. Frenk, S. D. M. White, J. M. Colberg, S. Cole, A. E. Evrard, H. M. P. Couchman, and N. Yoshida. The mass function of dark matter haloes. *MNRAS*, 321: 372–384, February 2001.
- L. J. King and P. Schneider. Cluster mass profiles from weak lensing II. *A&A*, 369: 1–15, Apr 2001. doi: 10.1051/0004-6361:20010030.

- R. A. Knop, G. Aldering, R. Amanullah, P. Astier, G. Blanc, M. S. Burns, A. Conley, S. E. Deustua, M. Doi, R. Ellis, S. Fabbro, G. Folatelli, A. S. Fruchter, G. Garavini, S. Garmond, K. Garton, R. Gibbons, G. Goldhaber, A. Goobar, D. E. Groom, D. Hardin, I. Hook, D. A. Howell, A. G. Kim, B. C. Lee, C. Lidman, J. Mendez, S. Nobili, P. E. Nugent, R. Pain, N. Panagia, C. R. Pennypacker, S. Perlmutter, R. Quimby, J. Raux, N. Regnault, P. Ruiz-Lapuente, G. Sainton, B. Schaefer, K. Schahmaneche, E. Smith, A. L. Spadafora, V. Stanishev, M. Sullivan, N. A. Walton, L. Wang, W. M. Wood-Vasey, and N. Yasuda. New Constraints on Ω_M , Ω_Λ , and w from an Independent Set of 11 High-Redshift Supernovae Observed with the Hubble Space Telescope. *ApJ*, 598(1):102–137, Nov 2003. doi: 10.1086/378560.
- J. M. Kovac, E. M. Leitch, C. Pryke, J. E. Carlstrom, N. W. Halverson, and W. L. Holzapfel. Detection of polarization in the cosmic microwave background using DASI. *Nature*, 420:772, December 2002.
- A. Lewis and A. Challinor. Weak gravitational lensing of the CMB. *Physics Reports*, 429:1–65, June 2006. doi: 10.1016/j.physrep.2006.03.002.
- LSST Science Collaboration, P. A. Abell, J. Allison, S. F. Anderson, J. R. Andrew, J. R. P. Angel, L. Armus, D. Arnett, S. J. Asztalos, T. S. Axelrod, and et al. LSST Science Book, Version 2.0. *ArXiv e-prints*, December 2009.
- A. D. Ludlow, J. F. Navarro, M. Boylan-Kolchin, P. E. Bett, R. E. Angulo, M. Li, S. D. M. White, C. Frenk, and V. Springel. The mass profile and accretion history of cold dark matter haloes. *MNRAS*, 432:1103–1113, June 2013. doi: 10.1093/mnras/stt526.
- M. Madhavacheril, N. Sehgal, R. Allison, N. Battaglia, J. R. Bond, E. Calabrese, J. Caliguri, K. Coughlin, D. Crichton, R. Datta, M. J. Devlin, J. Dunkley, R. Dünner, K. Fogarty, E. Grace, A. Hajian, M. Hasselfield, J. C. Hill, M. Hilton, A. D. Hincks, R. Hlozek, J. P. Hughes, A. Kosowsky, T. Louis, M. Lungu, J. McMahon, K. Moodley, C. Munson, S. Naess, F. Nati, L. Newburgh, M. D. Niemack, L. A. Page, B. Partridge, B. Schmitt, B. D. Sherwin, J. Sievers, D. N. Spergel, S. T. Staggs, R. Thornton, A. Van Engelen, J. T. Ward, E. J. Wollack, and Atacama Cosmology Telescope Collaboration. Evidence of Lensing of the Cosmic Microwave Background by Dark Matter Halos. *Physical Review Letters*, 114(15):151302, April 2015. doi: 10.1103/PhysRevLett.114.151302.
- M. S. Madhavacheril and J. C. Hill. Mitigating Foreground Biases in CMB Lensing Reconstruction Using Cleaned Gradients. *PRD*, (98):023534, July 2018. doi: 10.1103/PhysRevD.98.023534.
- A. B. Mantz, A. von der Linden, S. W. Allen, D. E. Applegate, P. L. Kelly, R. G.

- Morris, D. A. Rapetti, R. W. Schmidt, S. Adhikari, M. T. Allen, P. R. Burchat, D. L. Burke, M. Cataneo, D. Donovan, H. Ebeling, S. Shandera, and A. Wright. Weighing the giants - IV. Cosmology and neutrino mass. *MNRAS*, 446:2205–2225, January 2015. doi: 10.1093/mnras/stu2096.
- A. Manzotti, K. T. Story, W. L. K. Wu, J. E. Austermann, J. A. Beall, A. N. Bender, B. A. Benson, L. E. Bleem, J. J. Bock, J. E. Carlstrom, C. L. Chang, H. C. Chiang, H. Cho, R. Citron, A. Conley, T. M. Crawford, A. T. Crites, T. de Haan, M. A. Dobbs, S. Dodelson, W. Everett, J. Gallicchio, E. M. George, A. Gilbert, N. W. Halverson, N. Harrington, J. W. Henning, G. C. Hilton, G. P. Holder, W. L. Holzapfel, S. Hoover, Z. Hou, J. D. Hrubes, N. Huang, J. Hubmayr, K. D. Irwin, R. Keisler, L. Knox, A. T. Lee, E. M. Leitch, D. Li, J. J. McMahon, S. S. Meyer, L. M. Mocanu, T. Natoli, J. P. Nibarger, V. Novosad, S. Padin, C. Pryke, C. L. Reichardt, J. E. Ruhl, B. R. Saliwanchik, J. T. Sayre, K. K. Schaffer, G. Smecher, A. A. Stark, K. Vanderlinde, J. D. Vieira, M. P. Viero, G. Wang, N. Whitehorn, V. Yefremenko, and M. Zemcov. CMB Polarization B-mode Delensing with SPTpol and Herschel. *ArXiv e-prints*, January 2017.
- J. C. Mather, E. S. Cheng, D. A. Cottingham, Jr. Eplee, R. E., D. J. Fixsen, T. Hewagama, R. B. Isaacman, K. A. Jensen, S. S. Meyer, P. D. Noerdlinger, S. M. Read, L. P. Rosen, R. A. Shafer, E. L. Wright, C. L. Bennett, N. W. Boggess, M. G. Hauser, T. Kelsall, Jr. Moseley, S. H., R. F. Silverberg, G. F. Smoot, R. Weiss, and D. T. Wilkinson. Measurement of the Cosmic Microwave Background Spectrum by the COBE FIRAS Instrument. *ApJ*, 420:439, Jan 1994. doi: 10.1086/173574.
- I. McCarthy, A. M. C. Le Brun, J. Schaye, and G. P. Holder. The thermal Sunyaev-Zel'dovich effect power spectrum in light of Planck. *MNRAS*, 440:3645–3657, June 2014. doi: 10.1093/mnras/stu543.
- T. McClintock, T. N. Varga, D. Gruen, E. Rozo, E. S. Rykoff, T. Shin, P. Melchior, J. DeRose, S. Seitz, J. P. Dietrich, E. Sheldon, Y. Zhang, A. v. der Linden, T. Jeltema, A. B. Mantz, A. K. Romer, S. Allen, M. R. Becker, A. Bermeo, S. Bhargava, M. Costanzi, S. Everett, A. Farahi, N. Hamaus, W. G. Hartley, D. L. Hollowood, B. Hoyle, H. Israel, P. Li, N. MacCrann, G. Morris, A. Palmese, A. A. Plazas, G. Pollina, M. M. Rau, M. Simet, M. Soares-Santos, M. A. Troxel, C. V. Cervantes, R. H. Wechsler, J. Zuntz, T. M. C. Abbott, F. B. Abdalla, S. Allam, J. Annis, S. Avila, S. L. Bridle, D. Brooks, D. L. Burke, A. C. Rosell, M. C. Kind, J. Carretero, F. J. Castander, M. Crocce, C. E. Cunha, C. B. D'Andrea, L. N. da Costa, C. Davis, J. De Vicente, H. T. Diehl, P. Doel, A. Drlica-Wagner, A. E. Evrard, B. Flaugher, P. Fosalba, J. Frieman, J. García-Bellido, E. Gaztanaga, D. W. Gerdes, T. Giannan-

- tonio, R. A. Gruendl, G. Gutierrez, K. Honscheid, D. J. James, D. Kirk, E. Krause, K. Kuehn, O. Lahav, T. S. Li, M. Lima, M. March, J. L. Marshall, F. Menanteau, R. Miquel, J. J. Mohr, B. Nord, R. L. C. Ogando, A. Roodman, E. Sanchez, V. Scarpine, R. Schindler, I. Sevilla-Noarbe, M. Smith, R. C. Smith, F. Sobreira, E. Suchyta, M. E. C. Swanson, G. Tarle, D. L. Tucker, V. Vikram, A. R. Walker, and J. Weller. Dark Energy Survey Year 1 Results: Weak Lensing Mass Calibration of redMaPPer Galaxy Clusters. *MNRAS*, October 2018. doi: 10.1093/mnras/sty2711.
- P. Melchior, D. Gruen, T. McClintock, T. N. Varga, E. Sheldon, E. Rozo, A. Amara, M. R. Becker, B. A. Benson, A. Bermeo, S. L. Bridle, J. Clampitt, J. P. Dietrich, W. G. Hartley, D. Hollowood, B. Jain, M. Jarvis, T. Jeltema, T. Kacprzak, N. MacCrann, E. S. Rykoff, A. Saro, E. Suchyta, M. A. Troxel, J. Zuntz, C. Bonnett, A. A. Plazas, T. M. C. Abbott, F. B. Abdalla, J. Annis, A. Benoit-Lévy, G. M. Bernstein, E. Bertin, D. Brooks, E. Buckley-Geer, A. Carnero Rosell, M. Carrasco Kind, J. Carretero, C. E. Cunha, C. B. D’Andrea, L. N. da Costa, S. Desai, T. F. Eifler, B. Flaugher, P. Fosalba, J. García-Bellido, E. Gaztanaga, D. W. Gerdes, R. A. Gruendl, J. Gschwend, G. Gutierrez, K. Honscheid, D. J. James, D. Kirk, E. Krause, K. Kuehn, N. Kuropatkin, O. Lahav, M. Lima, M. A. G. Maia, M. March, P. Martini, F. Menanteau, C. J. Miller, R. Miquel, J. J. Mohr, R. C. Nichol, R. Ogando, A. K. Romer, E. Sanchez, V. Scarpine, I. Sevilla-Noarbe, R. C. Smith, M. Soares-Santos, F. Sobreira, M. E. C. Swanson, G. Tarle, D. Thomas, A. R. Walker, J. Weller, and Y. Zhang. Weak-lensing mass calibration of redMaPPer galaxy clusters in Dark Energy Survey Science Verification data. *MNRAS*, 469:4899–4920, August 2017. doi: 10.1093/mnras/stx1053.
- J.-B. Melin and J. G. Bartlett. Measuring cluster masses with CMB lensing: a statistical approach. *A&A*, 578:A21, June 2015. doi: 10.1051/0004-6361/201424720.
- A. Merloni, P. Predehl, W. Becker, H. Böhringer, T. Boller, H. Brunner, M. Brusa, K. Dennerl, M. Freyberg, P. Friedrich, A. Georgakakis, F. Haberl, G. Hasinger, N. Meidinger, J. Mohr, K. Nandra, A. Rau, T. H. Reiprich, J. Robrade, M. Salvato, A. Santangelo, M. Sasaki, A. Schwope, J. Wilms, and t. German eROSITA Consortium. eROSITA Science Book: Mapping the Structure of the Energetic Universe. *ArXiv e-prints*, September 2012.
- E. Morganson, R. A. Gruendl, F. Menanteau, M. Carrasco Kind, Y.-C. Chen, G. Dauves, A. Drlica-Wagner, D. N. Friedel, M. Gower, M. W. G. Johnson, M. D. Johnson, R. Kessler, F. Paz-Chinchón, D. Petracick, C. Pond, B. Yanny, S. Allam, R. Armstrong, W. Barkhouse, K. Bechtol, A. Benoit-Lévy, G. M. Bernstein, E. Bertin, E. Buckley-Geer, R. Covarrubias, S. Desai, H. T. Diehl, D. A. Goldstein, D. Gruen,

- T. S. Li, H. Lin, J. Marriner, J. J. Mohr, E. Neilsen, C.-C. Ngeow, K. Paech, E. S. Rykoff, M. Sako, I. Sevilla-Noarbe, E. Sheldon, F. Sobreira, D. L. Tucker, W. Wester, and DES Collaboration. The Dark Energy Survey Image Processing Pipeline. *PASP*, 130(7):074501, July 2018. doi: 10.1088/1538-3873/aab4ef.
- J. F. Navarro, C. S. Frenk, and S. D. M. White. The Structure of Cold Dark Matter Halos. *ApJ*, 462:563–+, May 1996. doi: 10.1086/177173.
- J. F. Navarro, C. S. Frenk, and S. D. M. White. A Universal Density Profile from Hierarchical Clustering. *ApJ*, 490:493–+, December 1997. doi: 10.1086/304888.
- S. Padin, Z. Staniszewski, R. Keisler, M. Joy, A. A. Stark, P. A. R. Ade, K. A. Aird, B. A. Benson, L. E. Bleem, J. E. Carlstrom, C. L. Chang, T. M. Crawford, A. T. Crites, M. A. Dobbs, N. W. Halverson, S. Heimsath, R. E. Hills, W. L. Holzapfel, C. Lawrie, A. T. Lee, E. M. Leitch, J. Leong, W. Lu, M. Lueker, J. J. McMahon, S. S. Meyer, J. J. Mohr, T. E. Montroy, T. Plagge, C. Pryke, J. E. Ruhl, K. K. Schaffer, E. Shirokoff, H. G. Spieler, and J. D. Vieira. South pole telescope optics. *Appl. Opt.*, 47(24):4418–4428, 2008.
- Sanjaykumar Patil, Srinivasan Raghunathan, and Christian L. Reichardt. Suppressing the thermal SZ-induced variance in CMB-cluster lensing estimators. *arXiv e-prints*, art. arXiv:1905.07943, May 2019.
- A. A. Penzias and R. W. Wilson. A Measurement of Excess Antenna Temperature at 4080 Mc/s. *ApJ*, 142:419–421, July 1965. URL http://adsabs.harvard.edu/cgi-bin/nph-bib_query?bibcode=1965ApJ...142..419P&db_key=AST.
- Planck Collaboration, P. A. R. Ade, N. Aghanim, C. Armitage-Caplan, M. Arnaud, M. Ashdown, F. Atrio-Barandela, J. Aumont, C. Baccigalupi, A. J. Banday, and et al. Planck 2013 results. XII. Diffuse component separation. *A&A*, 571:A12, Nov 2014a. doi: 10.1051/0004-6361/201321580.
- Planck Collaboration, P. A. R. Ade, N. Aghanim, C. Armitage-Caplan, M. Arnaud, M. Ashdown, F. Atrio-Barandela, J. Aumont, C. Baccigalupi, A. J. Banday, and et al. Planck 2013 results. XXIV. Constraints on primordial non-Gaussianity. *A&A*, 571:A24, Nov 2014b. doi: 10.1051/0004-6361/201321554.
- Planck Collaboration, P. A. R. Ade, N. Aghanim, M. Arnaud, M. Ashdown, J. Aumont, C. Baccigalupi, A. J. Banday, R. B. Barreiro, J. G. Bartlett, and et al. Planck 2015 results. XXIV. Cosmology from Sunyaev-Zeldovich cluster counts. *A&A*, 594:A24, September 2016a. doi: 10.1051/0004-6361/201525833.
- Planck Collaboration, P. A. R. Ade, N. Aghanim, M. Arnaud, M. Ashdown, J. Aumont, C. Baccigalupi, A. J. Banday, R. B. Barreiro, J. G. Bartlett, and et al. Planck 2015 results. XIII. Cosmological parameters. *A&A*, 594:A13, September 2016b. doi:

10.1051/0004-6361/201525830.

Planck Collaboration, P. A. R. Ade, N. Aghanim, M. Arnaud, J. Aumont, C. Baccigalupi, A. J. Banday, R. B. Barreiro, J. G. Bartlett, N. Bartolo, and et al. Planck 2015 results. XXIII. The thermal Sunyaev-Zeldovich effect-cosmic infrared background correlation. *A&A*, 594:A23, Sep 2016c. doi: 10.1051/0004-6361/201527418.

Planck Collaboration, N. Aghanim, Y. Akrami, M. Ashdown, J. Aumont, C. Baccigalupi, M. Ballardini, A. J. Banday, R. B. Barreiro, N. Bartolo, S. Basak, R. Battye, K. Benabed, J. P. Bernard, M. Bersanelli, P. Bielewicz, J. J. Bock, J. R. Bond, J. Borrill, F. R. Bouchet, F. Boulanger, M. Bucher, C. Burigana, R. C. Butler, E. Calabrese, J. F. Cardoso, J. Carron, A. Challinor, H. C. Chiang, J. Chluba, L. P. L. Colombo, C. Combet, D. Contreras, B. P. Crill, F. Cuttaia, P. de Bernardis, G. de Zotti, J. Delabrouille, J. M. Delouis, E. Di Valentino, J. M. Diego, O. Doré, M. Douspis, A. Ducout, X. Dupac, S. Dusini, G. Efstathiou, F. Elsner, T. A. Enßlin, H. K. Eriksen, Y. Fantaye, M. Farhang, J. Fergusson, R. Fernandez-Cobos, F. Finelli, F. Forastieri, M. Frailis, E. Franceschi, A. Frolov, S. Galeotta, S. Galli, K. Ganga, R. T. Génova-Santos, M. Gerbino, T. Ghosh, J. González-Nuevo, K. M. Górski, S. Gratton, A. Gruppuso, J. E. Gudmundsson, J. Hamann, W. Handley, D. Herranz, E. Hivon, Z. Huang, A. H. Jaffe, W. C. Jones, A. Karakci, E. Keihänen, R. Keskitalo, K. Kiiveri, J. Kim, T. S. Kisner, L. Knox, N. Krachmalnicoff, M. Kunz, H. Kurki-Suonio, G. Lagache, J. M. Lamarre, A. Lasenby, M. Lattanzi, C. R. Lawrence, M. Le Jeune, P. Lemos, J. Lesgourgues, F. Levrier, A. Lewis, M. Liguori, P. B. Lilje, M. Lilley, V. Lindholm, M. López-Caniego, P. M. Lubin, Y. Z. Ma, J. F. Macías-Pérez, G. Maggio, D. Maino, N. Mandolesi, A. Mangilli, A. Marcos-Caballero, M. Maris, P. G. Martin, M. Martinelli, E. Martínez-González, S. Matarrese, N. Mauri, J. D. McEwen, P. R. Meinhold, A. Melchiorri, A. Mennella, M. Migliaccio, M. Millea, S. Mitra, M. A. Miville-Deschénes, D. Molinari, L. Montier, G. Morgante, A. Moss, P. Natoli, H. U. Nørgaard-Nielsen, L. Pagano, D. Paoletti, B. Partridge, G. Patanchon, H. V. Peiris, F. Perrotta, V. Pettorino, F. Piacentini, L. Polastri, G. Polenta, J. L. Puget, J. P. Rachen, M. Reinecke, M. Remazeilles, A. Renzi, G. Rocha, C. Rosset, G. Roudier, J. A. Rubiño-Martín, B. Ruiz-Granados, L. Salvati, M. Sandri, M. Savainen, D. Scott, E. P. S. Shellard, C. Sirignano, G. Sirri, L. D. Spencer, R. Sunyaev, A. S. Suur-Uski, J. A. Tauber, D. Tavagnacco, M. Tenti, L. Toffolatti, M. Tomasi, T. Trombetti, L. Valenziano, J. Valiviita, B. Van Tent, L. Vibert, P. Vielva, F. Villa, N. Vittorio, B. D. Wandelt, I. K. Wehus, M. White, S. D. M. White, A. Zaccrei, and A. Zonca. Planck 2018 results. VI. Cosmological parameters. *arXiv e-prints*, art. arXiv:1807.06209, Jul 2018.

S. Raghunathan, S. Patil, E. J. Baxter, F. Bianchini, L. E. Bleem, T. M. Crawford,

- G. P. Holder, A. Manzotti, and C. L. Reichardt. Measuring galaxy cluster masses with CMB lensing using a Maximum Likelihood estimator: statistical and systematic error budgets for future experiments. *JCAP*, 8:030, August 2017. doi: 10.1088/1475-7516/2017/08/030.
- S. Raghunathan, S. Patil, E. Baxter, B. A. Benson, L. E. Bleem, T. L. Chou, T. M. Crawford, G. P. Holder, T. McClintock, C. L. Reichardt, E. Rozo, T. N. Varga, T. M. C. Abbott, P. A. R. Ade, S. Allam, A. J. Anderson, J. Annis, J. E. Austermann, S. Avila, J. A. Beall, K. Bechtol, A. N. Bender, G. Bernstein, E. Bertin, F. Bianchini, D. Brooks, D. L. Burke, J. E. Carlstrom, J. Carretero, C. L. Chang, H. C. Chiang, H.-M. Cho, R. Citron, A. T. Crites, C. E. Cunha, L. N. da Costa, C. Davis, S. Desai, H. T. Diehl, J. P. Dietrich, M. A. Dobbs, P. Doel, T. F. Eifler, W. Everett, A. E. Evrard, B. Flaugher, P. Fosalba, J. Frieman, J. Gallicchio, J. García-Bellido, E. Gaztanaga, E. M. George, A. Gilbert, D. Gruen, R. A. Gruendl, J. Gschwend, N. Gupta, G. Gutierrez, T. de Haan, N. W. Halverson, N. Harrington, W. G. Hartley, J. W. Henning, G. C. Hilton, D. L. Hollowood, W. L. Holzapfel, K. Honscheid, Z. Hou, B. Hoyle, J. D. Hrubes, N. Huang, J. Hubmayr, K. D. Irwin, D. J. James, T. Jeltema, A. G. Kim, M. Carrasco Kind, L. Knox, A. Kovacs, K. Kuehn, N. Kuropatkin, A. T. Lee, T. S. Li, M. Lima, M. A. G. Maia, J. L. Marshall, J. J. McMahon, P. Melchior, F. Menanteau, S. S. Meyer, C. J. Miller, R. Miquel, L. Mocanu, J. Montgomery, A. Nadolski, T. Natoli, J. P. Nibarger, V. Novosad, S. Padin, A. A. Plazas, C. Pryke, D. Rapetti, A. K. Romer, A. Carnero Rosell, J. E. Ruhl, B. R. Saliwanchik, E. Sanchez, J. T. Sayre, V. Scarpine, K. K. Schaffer, M. Schubnell, S. Serrano, I. Sevilla-Noarbe, G. Smecher, R. C. Smith, M. Soares-Santos, F. Sobreira, A. A. Stark, K. T. Story, E. Suchyta, M. E. C. Swanson, G. Tarle, D. Thomas, C. Tucker, K. Vanderlinde, J. De Vicente, J. D. Vieira, G. Wang, N. Whitehorn, W. L. K. Wu, and Y. Zhang. Mass Calibration of Optically Selected DES Clusters Using a Measurement of CMB-cluster Lensing with SPTpol Data. *ApJ*, 872:170, February 2019a. doi: 10.3847/1538-4357/ab01ca.
- S. Raghunathan, S. Patil, E. Baxter, B. A. Benson, L. E. Bleem, T. M. Crawford, G. P. Holder, T. McClintock, C. L. Reichardt, T. N. Varga, N. Whitehorn, P. A. R. Ade, S. Allam, A. J. Anderson, J. E. Austermann, S. Avila, J. S. Avva, D. Bacon, J. A. Beall, A. N. Bender, F. Bianchini, S. Bocquet, D. Brooks, D. L. Burke, J. E. Carlstrom, J. Carretero, F. J. Castander, C. L. Chang, H. C. Chiang, R. Citron, M. Costanzi, A. T. Crites, L. N. da Costa, S. Desai, H. T. Diehl, J. P. Dietrich, M. A. Dobbs, P. Doel, S. Everett, A. E. Evrard, C. Feng, B. Flaugher, P. Fosalba, J. Frieman, J. Gallicchio, J. García-Bellido, E. Gaztanaga, E. M. George, T. Giannantonio, A. Gilbert, R. A. Gruendl, J. Gschwend, N. Gupta, G. Gutierrez, T. de

- Haan, N. W. Halverson, N. Harrington, J. W. Henning, G. C. Hilton, D. L. Hollowood, W. L. Holzapfel, K. Honscheid, J. D. Hrubes, N. Huang, J. Hubmayr, K. D. Irwin, T. Jeltema, M. Carrasco Kind, L. Knox, N. Kuropatkin, O. Lahav, A. T. Lee, D. Li, M. Lima, A. Lowitz, M. A. G. Maia, J. L. Marshall, J. J. McMahon, P. Melchior, F. Menanteau, S. S. Meyer, R. Miquel, L. M. Mocanu, J. J. Mohr, J. Montgomery, C. Corbett Moran, A. Nadolski, T. Natoli, J. P. Nibarger, G. Noble, V. Novosad, R. L. C. Ogando, S. Padin, A. A. Plazas, C. Pryke, D. Rapetti, A. K. Romer, A. Roodman, A. Carnero Rosell, E. Rozo, J. E. Ruhl, E. S. Rykoff, B. R. Saliwanchik, E. Sanchez, J. T. Sayre, V. Scarpine, K. K. Schaffer, M. Schubnell, S. Serrano, I. Sevilla-Noarbe, C. Sievers, G. Smecher, M. Smith, M. Soares-Santos, A. A. Stark, K. T. Story, E. Suchyta, M. E. C. Swanson, G. Tarle, C. Tucker, K. Vanderlinde, T. Veach, J. De Vicente, J. D. Vieira, V. Vikram, G. Wang, W. L. K. Wu, V. Yefremenko, and Y. Zhang. A Detection of CMB-Cluster Lensing using Polarization Data from SPTpol. *arXiv e-prints*, art. arXiv:1907.08605, Jul 2019b.
- A. Refregier, A. Amara, T. D. Kitching, A. Rassat, R. Scaramella, J. Weller, and for the Euclid Imaging Consortium. Euclid Imaging Consortium Science Book. *arXiv e-prints*, art. arXiv:1001.0061, Jan 2010.
- E. Rozo, E. S. Rykoff, A. Abate, C. Bennett, M. Crocce, C. Davis, B. Hoyle, B. Leistedt, H. V. Peiris, R. H. Wechsler, T. Abbott, F. B. Abdalla, M. Banerji, A. H. Bauer, A. Benoit-Lévy, G. M. Bernstein, E. Bertin, D. Brooks, E. Buckley-Geer, D. L. Burke, D. Capozzi, A. C. Rosell, D. Carollo, M. C. Kind, J. Carretero, F. J. Castander, M. J. Childress, C. E. Cunha, C. B. D’Andrea, T. Davis, D. L. DePoy, S. Desai, H. T. Diehl, J. P. Dietrich, P. Doel, T. F. Eifler, A. E. Evrard, A. F. Neto, B. Flaugher, P. Fosalba, J. Frieman, E. Gaztanaga, D. W. Gerdes, K. Glazebrook, D. Gruen, R. A. Gruendl, K. Honscheid, D. J. James, M. Jarvis, A. G. Kim, K. Kuehn, N. Kuropatkin, O. Lahav, C. Lidman, M. Lima, M. A. G. Maia, M. March, P. Martini, P. Melchior, C. J. Miller, R. Miquel, J. J. Mohr, R. C. Nichol, B. Nord, C. R. O’Neill, R. Ogando, A. A. Plazas, A. K. Romer, A. Roodman, M. Sako, E. Sanchez, B. Santiago, M. Schubnell, I. Sevilla-Noarbe, R. C. Smith, M. Soares-Santos, F. Sobreira, E. Suchyta, M. E. C. Swanson, J. Thaler, D. Thomas, S. Uddin, V. Vikram, A. R. Walker, W. Wester, Y. Zhang, and L. N. da Costa. redMaGiC: selecting luminous red galaxies from the DES Science Verification data. *MNRAS*, 461:1431–1450, September 2016. doi: 10.1093/mnras/stw1281.
- E. S. Rykoff, E. Rozo, M. T. Busha, C. E. Cunha, A. Finoguenov, A. Evrard, J. Hao, B. P. Koester, A. Leauthaud, B. Nord, M. Pierre, R. Reddick, T. Sadibekova, E. S. Sheldon, and R. H. Wechsler. redMaPPer. I. Algorithm and SDSS DR8 Catalog. *ApJ*, 785:104, April 2014. doi: 10.1088/0004-637X/785/2/104.

- E. S. Rykoff, E. Rozo, D. Hollowood, A. Bermeo-Hernandez, T. Jeltema, J. Mayers, A. K. Romer, P. Rooney, A. Saro, C. Vergara Cervantes, R. H. Wechsler, H. Wilcox, T. M. C. Abbott, F. B. Abdalla, S. Allam, J. Annis, A. Benoit-Lévy, G. M. Bernstein, E. Bertin, D. Brooks, D. L. Burke, D. Capozzi, A. Carnero Rosell, M. Carrasco Kind, F. J. Castander, M. Childress, C. A. Collins, C. E. Cunha, C. B. D’Andrea, L. N. da Costa, T. M. Davis, S. Desai, H. T. Diehl, J. P. Dietrich, P. Doel, A. E. Evrard, D. A. Finley, B. Flaugher, P. Fosalba, J. Frieman, K. Glazebrook, D. A. Goldstein, D. Gruen, R. A. Gruendl, G. Gutierrez, M. Hilton, K. Honscheid, B. Hoyle, D. J. James, S. T. Kay, K. Kuehn, N. Kuropatkin, O. Lahav, G. F. Lewis, C. Lidman, M. Lima, M. A. G. Maia, R. G. Mann, J. L. Marshall, P. Martini, P. Melchior, C. J. Miller, R. Miquel, J. J. Mohr, R. C. Nichol, B. Nord, R. Ogando, A. A. Plazas, K. Reil, M. Sahlén, E. Sanchez, B. Santiago, V. Scarpine, M. Schubnell, I. Sevilla-Noarbe, R. C. Smith, M. Soares-Santos, F. Sobreira, J. P. Stott, E. Suchyta, M. E. C. Swanson, G. Tarle, D. Thomas, D. Tucker, S. Uddin, P. T. P. Viana, V. Vikram, A. R. Walker, Y. Zhang, and DES Collaboration. The RedMaPPer Galaxy Cluster Catalog From DES Science Verification Data. *ApJS*, 224:1, May 2016. doi: 10.3847/0067-0049/224/1/1.
- S. Y. Sazonov and R. A. Sunyaev. Microwave polarization in the direction of galaxy clusters induced by the cmb quadrupole anisotropy. *MNRAS*, 310:765, December 1999. URL http://adsabs.harvard.edu/cgi-bin/nph-bib_query?bibcode=1999MNRAS.310..765S&db_key=AST.
- K. K. Schaffer, T. M. Crawford, K. A. Aird, B. A. Benson, L. E. Bleem, J. E. Carlstrom, C. L. Chang, H. M. Cho, A. T. Crites, T. de Haan, M. A. Dobbs, E. M. George, N. W. Halverson, G. P. Holder, W. L. Holzapfel, S. Hoover, J. D. Hrubes, M. Joy, R. Keisler, L. Knox, A. T. Lee, E. M. Leitch, M. Lueker, D. Luong-Van, J. J. McMahon, J. Mehl, S. S. Meyer, J. J. Mohr, T. E. Montroy, S. Padin, T. Plagge, C. Pryke, C. L. Reichardt, J. E. Ruhl, E. Shirokoff, H. G. Spieler, B. Stalder, Z. Staniszewski, A. A. Stark, K. Story, K. Vanderlinde, J. D. Vieira, and R. Williamson. The First Public Release of South Pole Telescope Data: Maps of a 95 deg² Field from 2008 Observations. *ApJ*, 743:90, December 2011. doi: 10.1088/0004-637X/743/1/90.
- N. Sehgal, P. Bode, S. Das, C. Hernandez-Monteagudo, K. Huffenberger, Y.-T. Lin, J. P. Ostriker, and H. Trac. Simulations of the Microwave Sky. *ApJ*, 709:920–936, February 2010. doi: 10.1088/0004-637X/709/2/920.
- M. Seiffert, C. Borys, D. Scott, and M. Halpern. An upper limit to polarized submillimetre emission in Arp 220. *MNRAS*, 374:409–414, January 2007. doi: 10.1111/j.1365-2966.2006.11186.x.

- Mauro Sereno, Cosimo Fedeli, and Lauro Moscardini. Comparison of weak lensing by NFW and Einasto halos and systematic errors. *JCAP*, 2016(1):042, Jan 2016. doi: 10.1088/1475-7516/2016/01/042.
- J. Silk. Cosmic black-body radiation and galaxy formation. *ApJ*, 151:459, 1968.
- M. Simet, T. McClintock, R. Mandelbaum, E. Rozo, E. Rykoff, E. Sheldon, and R. H. Wechsler. Erratum: Weak Lensing Measurement of the Mass-Richness Relation of SDSS redMaPPer Clusters. *MNRAS*, 480:5385–5385, November 2018. doi: 10.1093/mnras/sty2318.
- J. Song, A. Zenteno, B. Stalder, S. Desai, L. E. Bleem, K. A. Aird, R. Armstrong, M. L. N. Ashby, M. Bayliss, G. Bazin, B. A. Benson, E. Bertin, M. Brodwin, J. E. Carlstrom, C. L. Chang, H. M. Cho, A. Clocchiatti, T. M. Crawford, A. T. Crites, T. de Haan, M. A. Dobbs, J. P. Dudley, R. J. Foley, E. M. George, D. Gettings, M. D. Gladders, A. H. Gonzalez, N. W. Halverson, N. L. Harrington, F. W. High, G. P. Holder, W. L. Holzapfel, S. Hoover, J. D. Hrubes, M. Joy, R. Keisler, L. Knox, A. T. Lee, E. M. Leitch, J. Liu, M. Lueker, D. Luong-Van, D. P. Marrone, M. McDonald, J. J. McMahon, J. Mehl, S. S. Meyer, L. Mocanu, J. J. Mohr, T. E. Montroy, T. Natoli, D. Nurgaliev, S. Padin, T. Plagge, C. Pryke, C. L. Reichardt, A. Rest, J. Ruel, J. E. Ruhl, B. R. Saliwanchik, A. Saro, J. T. Sayre, K. K. Schaffer, L. Shaw, E. Shirokoff, R. Šuhada, H. G. Spieler, S. A. Stanford, Z. Staniszewski, A. A. Stark, K. Story, C. W. Stubbs, A. van Engelen, K. Vanderlinde, J. D. Vieira, R. Williamson, and O. Zahn. Redshifts, Sample Purity, and BCG Positions for the Galaxy Cluster Catalog from the First 720 Square Degrees of the South Pole Telescope Survey. *ApJ*, 761:22, December 2012. doi: 10.1088/0004-637X/761/1/22.
- R. Sunyaev and Y. Zel'dovich. Small-scale fluctuations of relic radiation. *Astrophysics and Space Science*, 7:3, 1970. URL http://adsabs.harvard.edu/cgi-bin/nph-bib_query?bibcode=1970Ap%26SS...7....3S&db_key=AST.
- R. A. Sunyaev and Y. B. Zel'dovich. The Observations of Relic Radiation as a Test of the Nature of X-Ray Radiation from the Clusters of Galaxies. *Comments on Astrophysics and Space Physics*, 4:173–+, November 1972.
- A. Suzuki, P. Ade, Y. Akiba, C. Aleman, K. Arnold, C. Baccigalupi, B. Barch, D. Barron, A. Bender, D. Boettger, J. Borrill, S. Chapman, Y. Chinone, A. Cukierman, M. Dobbs, A. Ducout, R. Dunner, T. Elleflot, J. Errard, G. Fabbian, S. Feeney, C. Feng, T. Fujino, G. Fuller, A. Gilbert, N. Goeckner-Wald, J. Groh, T. De Haan, G. Hall, N. Halverson, T. Hamada, M. Hasegawa, K. Hattori, M. Hazumi, C. Hill, W. Holzapfel, Y. Hori, L. Howe, Y. Inoue, F. Irie, G. Jaehnig, A. Jaffe, O. Jeong, N. Katayama, J. Kaufman, K. Kazemzadeh, B. Keating, Z. Kermish, R. Keski-

- talo, T. Kisner, A. Kusaka, M. Le Jeune, A. Lee, D. Leon, E. Linder, L. Lowry, F. Matsuda, T. Matsumura, N. Miller, K. Mizukami, J. Montgomery, M. Navaroli, H. Nishino, J. Peloton, D. Poletti, G. Puglisi, G. Rebeiz, C. Raum, C. Reichardt, P. Richards, C. Ross, K. Rotermund, Y. Segawa, B. Sherwin, I. Shirley, P. Siritanasak, N. Stebor, R. Stompor, J. Suzuki, O. Tajima, S. Takada, S. Takakura, S. Takatori, A. Tikhomirov, T. Tomaru, B. Westbrook, N. Whitehorn, T. Yamashita, A. Zahn, and O. Zahn. The Polarbear-2 and the Simons Array Experiments. *Journal of Low Temperature Physics*, 184(3-4):805–810, Aug 2016. doi: 10.1007/s10909-015-1425-4.
- R. Takahashi, T. Hamana, M. Shirasaki, T. Namikawa, T. Nishimichi, K. Osato, and K. Shiroyama. Full-sky Gravitational Lensing Simulation for Large-area Galaxy Surveys and Cosmic Microwave Background Experiments. *ApJ*, 850:24, November 2017. doi: 10.3847/1538-4357/aa943d.
- The Simons Observatory Collaboration, P. Ade, J. Aguirre, Z. Ahmed, S. Aiola, A. Ali, D. Alonso, M. A. Alvarez, K. Arnold, P. Ashton, and et al. The Simons Observatory: Science goals and forecasts. *Journal of Cosmology and Astro-Particle Physics*, 2019(2):056, Feb 2019. doi: 10.1088/1475-7516/2019/02/056.
- J. Tinker, A. V. Kravtsov, A. Klypin, K. Abazajian, M. Warren, G. Yepes, S. Gottlöber, and D. E. Holz. Toward a Halo Mass Function for Precision Cosmology: The Limits of Universality. *ApJ*, 688:709–728, December 2008. doi: 10.1086/591439.
- A. von der Linden, M. T. Allen, D. E. Applegate, P. L. Kelly, S. W. Allen, H. Ebeling, P. R. Burchat, D. L. Burke, D. Donovan, R. G. Morris, R. Blandford, T. Erben, and A. Mantz. Weighing the Giants - I. Weak-lensing masses for 51 massive galaxy clusters: project overview, data analysis methods and cluster images. *MNRAS*, 439: 2–27, March 2014. doi: 10.1093/mnras/stt1945.
- S.D.M. White, J.F. Navarro, A.E. Evrard, and C.S. Frenk. The baryon content of galaxy clusters: A challenge to cosmological orthodoxy. *Nature*, 366:429, 1993.
- J. Yoo and M. Zaldarriaga. Improved estimation of cluster mass profiles from the cosmic microwave background. *PRD*, 78(8):083002, October 2008. doi: 10.1103/PhysRevD.78.083002.

Appendix A

Appendix A

A.1 Section in an appendix

A.2 Simulated skies

The MLE presented in this work depends being able to produce large numbers of realistic simulated skies, incorporating a diverse range of astrophysical signals: the CMB (lensed by the galaxy cluster), radio galaxies, dusty galaxies, the kSZ effect, and the tSZ effect. One unique challenge for cluster studies is that the galaxy cluster itself can source most of these signals in addition to contributions from other unrelated haloes. These simulated skies are used for the calculation of the pixel-pixel covariance matrix, and for the creation of mock data sets (§??). In this appendix, we detail the creation of these sky simulations.

The sequence of operations is as follows. First, simulations of each signal are created on $50' \times 50'$ boxes with a $0.25'$ pixel resolution. Most of this appendix will focus on how this is done. The CMB maps are then lensed by the galaxy cluster, convolved by a Gaussian beam of the appropriate size, and rebinned to $0.5'$ pixels. This final rebinning reduces the number of map pixels four-fold and substantially speeds up the MLE without significantly reducing the SNR. White, Gaussian instrumental noise is added, with a pixel RMS level based on an experiment's sensitivity, observing time and survey area. For computational reasons, the $50' \times 50'$ box is cut down to the central $10' \times 10'$ area used in the analysis. Finally we point out a subtle effect because of shrinking the simulations to a $50' \times 50'$ box. Choosing a smaller box will reduce the background CMB gradient and subsequently the lensing signal generated by the cluster – which will tend to worsen $\Delta M/M$. To quantify this, we repeated our simulations with a larger $2^\circ \times 2^\circ$ such that it encompasses the first peak of the CMB. At $\Delta T = 1\mu K - arcmin$ for a sample of 100,000 clusters, the mass uncertainty $\Delta M/M$ is now 0.237% as opposed to 0.252% in the left panel of Fig ??, a very small effect.

Since we are dealing with very small areas of sky, we adopt the flat-sky approximation and substitute Fourier transforms for spherical harmonic transforms. The Fourier wavenumber k is related to the multipole ℓ by $k = \sqrt{k_x^2 + k_y^2} = \frac{\ell}{2\pi}$. We define the azimuthal angle ϕ_ℓ as $\tan^{-1}(k_y/k_x)$.

A.2.1 Cosmic Microwave Background

To simulate CMB maps that have been lensed by a massive galaxy cluster, we begin by creating T, Q, and U maps that are Gaussian realizations (?) of the CMB power spectra ($C_\ell^{TT}, C_\ell^{TE}, C_\ell^{EE}$, and C_ℓ^{BB}). For these fiducial power spectra, we use the lensed CMB power spectra predicted by CAMB (?) for the *Planck* 2015 Λ CDM cosmology¹. Note that the tensor-to-scalar ratio r is zero in this chain, and there is no contribution from inflationary B-modes (?). By using Gaussian realizations of the lensed CMB power spectra, we are effectively assuming (1) that the lensing due to large-scale structures (LSS) occurs at higher redshift than the galaxy cluster, and (2) that the small non-Gaussianities due to this LSS lensing are negligible. We then lens the T, Q, and U maps using with the cluster convergence profile described in §???. We deal with sub-pixel deflection angles by interpolating over the maps using a fifth-degree B-spline interpolation.

A.2.2 Sunyaev-Zel'dovich (SZ) effect

There are two SZ effects of interest: the kinematic SZ (kSZ) effect and the thermal SZ (tSZ) effect. Both SZ effects have contributions from the cluster itself as well as from unrelated haloes. For the latter signal, we assume the best-fit tSZ and kSZ power spectra from ?. We use the ? model for the tSZ power spectrum with an overall normalization of $D_{\ell=3000}^{\text{tSZ,150GHz}} = 3.7 \mu K^2$. For the kSZ spectrum, we take the ? model with an overall normalization of $D_{\ell=3000}^{\text{kSZ}} = 2.9 \mu K^2$. For the uncorrelated tSZ and kSZ signals, we simply create Gaussian realizations of these two spectra.

In some cases, we wish to study the effect of the kSZ and tSZ signals from the galaxy cluster in question. At these times, we add the cutouts around comparable mass haloes in simulated SZ maps to the simple Gaussian CMB realizations. We use the kSZ maps provided for the ? N-body simulations, while for tSZ maps, we use the smoothed-particle hydrodynamics (SPH) simulations of ?.

¹More specifically, we use the best-fit parameters from the *Planck* 2015 chain that combines the *Planck* 2015 temperature, polarization, lensing power spectra with BAO, H_0 , and SNe data (TT, TE, EE+lowP+lensing+ext in Table 4 of ?).

We ignore the extremely small polarized SZ signals in all cases. To generate polarization the free electrons of the intracluster medium must be exposed to a quadrupole radiation field, due to the CMB quadrupole mode for tSZ polarization, p_{tSZ} , and to an apparent CMB quadrupole created by the Doppler effect of bulk velocities in the electrons for kSZ polarization, p_{kSZ} . The level of the tSZ polarization is $p_{tSZ} \sim 0.1(\tau_e/0.02) \mu K$ while the kSZ polarization level is $p_{kSZ} \sim 0.1\beta_t^2\tau_e K$ (??) where τ_e is the optical depth of the cluster and $\beta_t = v/c$ transverse component of the electron's velocity. The clusters used in this work have $M_{200} = 2 \times 10^{14} M_\odot$ and an expected optical depth of $\tau_e \sim 0.004$ (?). We assume a velocity, $v = 1000 km s^{-1}$, leading to $p_{tSZ} = 20 nK$ and $p_{kSZ} = 2 nK$. This level of polarization is negligible.

A.2.3 Radio and Dusty Galaxies

We also create simulated maps of radio and dusty galaxies. These maps include four terms:

1. radio galaxies following a spatial Poisson distribution ($C_\ell^{radio} \propto \text{constant}$),
2. dusty star forming galaxies (DGs) also following a spatial Poisson distribution ($C_\ell^{DG-Po} \propto \text{constant}$),
3. clustering of DGs ($C_\ell^{DG-clus} \propto \ell^{0.8}$), and
4. the overdensity of DGs in galaxy clusters

The first three items are uncorrelated with the galaxy cluster and are expected to reduce the SNR of the estimators without biasing the reconstructed lensing mass. However, the relative overdensity of DGs in galaxy clusters can potentially bias the derived masses, and is discussed in §???. We assume the galaxies are randomly polarized at the 4% level, based on ?. This 4% level is expected to be an over-estimate for the DGs (?).

For radio galaxies, we draw a Poisson realization of the number counts as a function of flux (?). We ignore the clustering of radio galaxies as it is irrelevant at frequencies observed by the CMB telescopes (??). We take a more sophisticated approach for the dusty galaxies to handle the clustering and tSZ-CIB correlation. We begin by taking a Poisson distribution for the unusually bright dusty galaxies ($> 1 mJy$) (?). For fainter DGs, we create a set of number density contrast maps $\delta(\hat{\mathbf{n}})^{DG-Po}$ covering narrow flux bins. We adjust these number density

contrast maps to account for the desired clustering and correlation properties as outlined below, and then assign random fluxes to each pixel in Jy/sr (drawn uniformly across the flux bin). The resulting flux maps are then converted to CMB temperature units (μK_{CMB}).

For the tSZ-CIB correlation, we use the tSZ simulations produced by ? and the $C_\ell^{\text{tSZ} \times \text{CIB}}$ cross spectrum measured by ?. Using these we produce a tSZ \times CIB correlated map $T(\hat{\mathbf{n}})^{\text{tSZ} \times \text{CIB}}$ and a weight map $W(\hat{\mathbf{n}})^{\text{DG} \times \text{tSZ}}$ to modify $\delta(\hat{\mathbf{n}})^{\text{DG-Po}}$ as

$$T_\ell \equiv T_\ell^{\text{tSZ} \times \text{CIB}} = T_\ell^{\text{tSZ}} \frac{C_\ell^{\text{tSZ} \times \text{CIB}}}{C_\ell^{\text{tSZ}}} \quad (\text{A.1})$$

$$W(\hat{\mathbf{n}}) \equiv W(\hat{\mathbf{n}})^{\text{DG} \times \text{tSZ}} = \frac{|T(\hat{\mathbf{n}})|}{\sum |T(\hat{\mathbf{n}})|} \quad (\text{A.2})$$

$$\tilde{\delta}(\hat{\mathbf{n}})^{\text{DG} \times \text{tSZ}} = W(\hat{\mathbf{n}}) \delta(\hat{\mathbf{n}})^{\text{DG-Po}} \quad (\text{A.3})$$

where subscripts ℓ refer to the harmonic space transforms of the CMB map $T(\hat{\mathbf{n}})$. Eq.(A.2) and Eq.(A.3) ensure that the number of point sources are conserved and are predominantly clustered near massive dark matter haloes. For the clustering component of DG we modify Eq.(A.3) following ?

$$\tilde{\delta}_\ell^{\text{DG}} \equiv \tilde{\delta}_\ell^{\text{DG-Po,clus,tSZ}} = \tilde{\delta}_\ell^{\text{DG} \times \text{tSZ}} \frac{\sqrt{C_\ell^{\text{Po}} + C_\ell^{\text{clus}}}}{\sqrt{C_\ell^{\text{Po}}}} \quad (\text{A.4})$$